Title

Retrospective Search for Strongly Lensed Supernovae in the DESI Legacy Imaging Surveys

Journal

The Astrophysical Journal, 952(1)

ISSN

0004-637X

Authors

Sheu, William

Huang, Xiaosheng

Cikota, Aleksandar

et al.

Publication Date

2023-07-01

DOI

10.3847/1538-4357/acd1e4

The Astrophysical Journal, 952:10 (40pp), 2023 July 20 https://doi.org/10.3847/1538-4357/acd1e4

Retrospective Search for Strongly Lensed Supernovae in the DESI Legacy Imaging Surveys

William Sheu[1,2], Xiaosheng Huang[2,3], Aleksandar Cikota[4], Nao Suzuki[2,5], David J. Schlegel[2], and Christopher Storfer[2,6]
[1] Department of Physics & Astronomy, University of California, Los Angeles 430 Portola Plaza, Los Angeles, CA 90095, USA; wsheu@astro.ucla.edu
[2] Physics Division, Lawrence Berkeley National Laboratory, 1 Cyclotron Road, Berkeley, CA 94720, USA; xhuang22@usfca.edu
[3] Department of Physics & Astronomy, University of San Francisco, 2130 Fulton Street, San Francisco, CA 94117-1080, USA
[4] Gemini Observatory/NSF's NOIRLab Casilla 603, La Serena, Chile
[5] Kavli Institute for the Physics and Mathematics of the Universe, University of Tokyo Kashiwa 277-8583, Japan
[6] Institute for Astronomy, University of Hawaii, 2680 Woodlawn Drive, Honolulu, HI 96822-1897, USA
Received 2023 January 8; revised 2023 March 30; accepted 2023 May 1; published 2023 July 13

Abstract

The introduction of deep wide-field surveys in recent years and the adoption of machine-learning techniques have led to the discoveries of $\mathcal{O}(10^4)$ strong gravitational lensing systems and candidates. However, the discovery of multiply-lensed transients remains a rarity. Lensed transients and especially lensed supernovae are invaluable tools to cosmology because they allow us to constrain cosmological parameters via lens modeling and the measurements of their time delays. In this paper, we develop a pipeline to perform a targeted lensed transient search. We apply this pipeline to 5807 strong lenses and candidates, which were identified in the literature, in the DESI Legacy Imaging Surveys Data Release 9 (DR9) footprint. For each system, we analyze every exposure in all of the observed bands (DECam *g*, *r*, and *z*). Our pipeline finds, groups, and ranks detections that are in sufficient proximity temporally and spatially. After the first round of inspection, for promising candidate systems, we further examine the newly available DR10 data (with additional *i* and *Y* bands). Here we present our targeted lensed supernova search pipeline and seven new lensed supernova candidates, including a very likely lensed supernova—probably a Type Ia—in a system with an Einstein radius of $\sim 1\farcs5$.

Unified Astronomy Thesaurus concepts: Strong gravitational lensing (1643); Gravitational lensing (670); Supernovae (1668); Type Ia supernovae (1728); Core-collapse supernovae (304); Hubble constant (758); Cosmology (343); Observational cosmology (1146)

1. Introduction

The flat ΛCDM cosmological model is highly successful in describing our universe from the time of photon decoupling (at a redshift $z \approx 1100$) to the present time. According to this model, our universe has a flat geometry and is expanding at an accelerating rate (Riess et al. 1998; Perlmutter et al. 1999). The present day expansion rate of the universe is known as the Hubble constant (H_0). The inferred value for H_0 from the Planck CMB measurements is $67.4 \pm 0.5\,\mathrm{km\,s^{-1}\,Mpc^{-1}}$ (Planck Collaboration et al. 2020). Meanwhile, direct measurements of H_0 using local distance ladders is higher by $\gtrsim 4\sigma$ (e.g., Riess et al. 2021). Thus, if this inconsistency is not due to systematic effects (e.g., Freedman 2021), then at, a minimum, ΛCDM needs revision.

If a transient event were to occur in a strongly-lensed background galaxy, then it can be potentially observed multiple times, in each of the lensed images. The time delay Δt between the different images consists of a geometric component and a gravitational component (e.g., Narayan & Bartelmann 1996). A competitive H_0 constraint can be achieved if the time delays can be measured precisely and the lensing potential can be modeled accurately, providing an independent method to measure the Hubble constant (e.g., Suyu et al. 2020). If the observed transient is a lensed Type Ia supernova (L-SN Ia), then their standardizability can also significantly reduce the main systematic effect for lensing-based H_0 measurements, i.e., the mass sheet degeneracy (e.g., Birrer et al. 2022).

There are currently seven confirmed lensed SNe: Quimby et al. (2014; PS1-10afx), Kelly et al. (2015; SN Refsdal), Goobar et al. (2017; SN 2016geu), Rodney et al. (2021; SN Requiem), Kelly et al. (2022; AT 2022riv), Goobar et al. (2022; SN Zwicky), and Chen et al. (2022; C22). Out of the seven, four are lensed by a galaxy cluster (SN Refsdal, SN Requiem, AT 2022riv, and C22). Of the remaining three that were lensed by single galaxies, two were found live (SN 2016geu and SN Zwicky). Both happen to be Type Ia. However, both have subarcsecond Einstein radii, and thus short time delays of $\lesssim 1$ day, which makes them unuseful for H_0 measurements (Dhawan et al. 2020; Goobar et al. 2022; Pierel et al. 2023). Some cluster lenses have very long time delays (e.g., two decades for SN Requiem) and they generally have larger modeling uncertainties, but with different systematics compared with galaxy-scale lenses. Lensed SNe that are found behind cluster with time delays at a reasonable timescale may still yield competitive H_0 measurements (e.g., Grillo et al. 2020). In recent years, thousands of new strong lenses have been discovered in imaging surveys (e.g., Jacobs et al. 2019; Cañameras et al. 2020; Huang et al. 2020; Cañameras et al. 2021; Huang et al. 2021; Shu et al. 2022; Stein et al. 2022; Storfer et al. 2022). Most of them are galaxy-scale lenses, with a small number of group/cluster lenses. They are resolved in ground-based observations, and thus are expected to have time delays (on the order of days to weeks) that are useful for

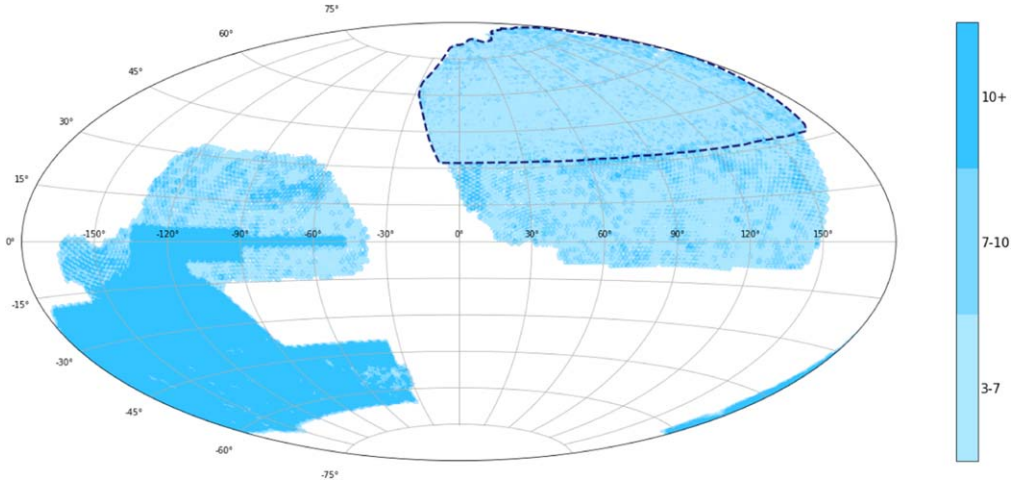

Figure 1. The Legacy Imaging Surveys DR9 footprint, color coded by the z band observation depth. We perform a targeted search for lensed transients within the DECaLS region (decl. $<32°$). Exposures from the MzLS and BASS surveys (blue-dashed outline) are excluded.

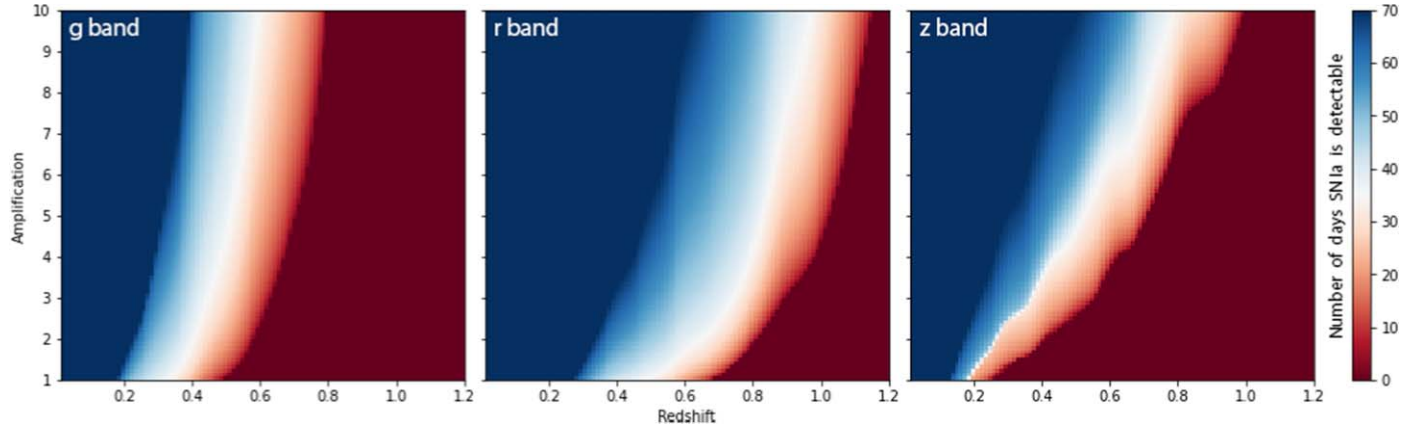

Figure 2. Number of days when a L-SN Ia is detectable as a function of redshift and lensing amplification in DECam g, r, and z bands. Every pixel in each plot represents a simulated SALT3 light-curve model, color coded by the number of days that it exceeds the corresponding filter's 5σ PSF detection limit.

H_0 measurements. In this paper, we develop a targeted lensed transient pipeline to search among these systems in the DESI Legacy Imaging Surveys (Dey et al. 2019) footprint.

By applying our pipeline to the Legacy Surveys in a retrospective search, we have discovered seven new lensed supernova candidates. Along with the discoveries of many lensed quasars (which will be presented in a separate publication), we are confident that our pipeline is capable of finding live lensed transients for present (e.g., Pan-STARRS; Chambers et al. 2016) and future surveys (e.g., LSST and the Roman Space Telescope; Ivezić et al. 2019 and Spergel et al. 2015 respectively).

2. Observation

The DESI Legacy Imaging Surveys is composed of three surveys: the Dark Energy Camera Legacy Survey (DECaLS), the Beijing Arizona Sky Survey (BASS), and the Mayall z band Legacy Survey (MzLS). DECaLS is observed by the Dark Energy Camera (DECam; Flaugher et al. 2015) on the 4 m Blanco telescope, which covers $\sim$9000 deg^2 of the sky in the range of $-18° \lesssim \delta \lesssim +32°$. BASS/MzLS are observed in the g and r bands by the 90Prime camera (Williams et al. 2004) on the Bok 2.3 m telescope and in the z band by the Mosaic3 camera (Dey et al. 2016) on the 4 m Mayall telescope. Together BASS/MzLS cover the same $\sim$5000 deg^2 of the northern subregion of the Legacy Surveys. For this search, we exclude BASS and MzLS data because there are fewer exposures from each of the component surveys, with inferior seeing in gr bands for reliable detection of transients. Data Release 9 (DR9) contains additional DECam data reprocessed from the Dark Energy Survey (DES; Dark Energy Survey Collaboration et al. 2016) for $\delta \lesssim -18°$. This provides an additional $\sim$5000 deg^2, resulting in a total footprint of $\sim$19,000 deg^2 (see Figure 1). Data release 10 (DR10) supplements DR9 with additional DECam exposures (including additional optical bands) from NOIRLab. Both data releases are publicly available.[7] The DECam surveys will hereafter be referred to in its entirety as DECaLS, within which we distinguish DES and non-DES regions. The pipeline deployment will mostly focus on the exposures in DECaLS, in g, r, and z filters, with a nominal DES exposure time of 90 s, and non-DES exposure time ranging from 60 to 200 s. In addition, the Legacy Surveys contain deep field DECam observations (from surveys such as COSMOS, XMM-LSS, and SN-X3), with 800+ exposures for any given

[7] https://www.legacysurvey.org

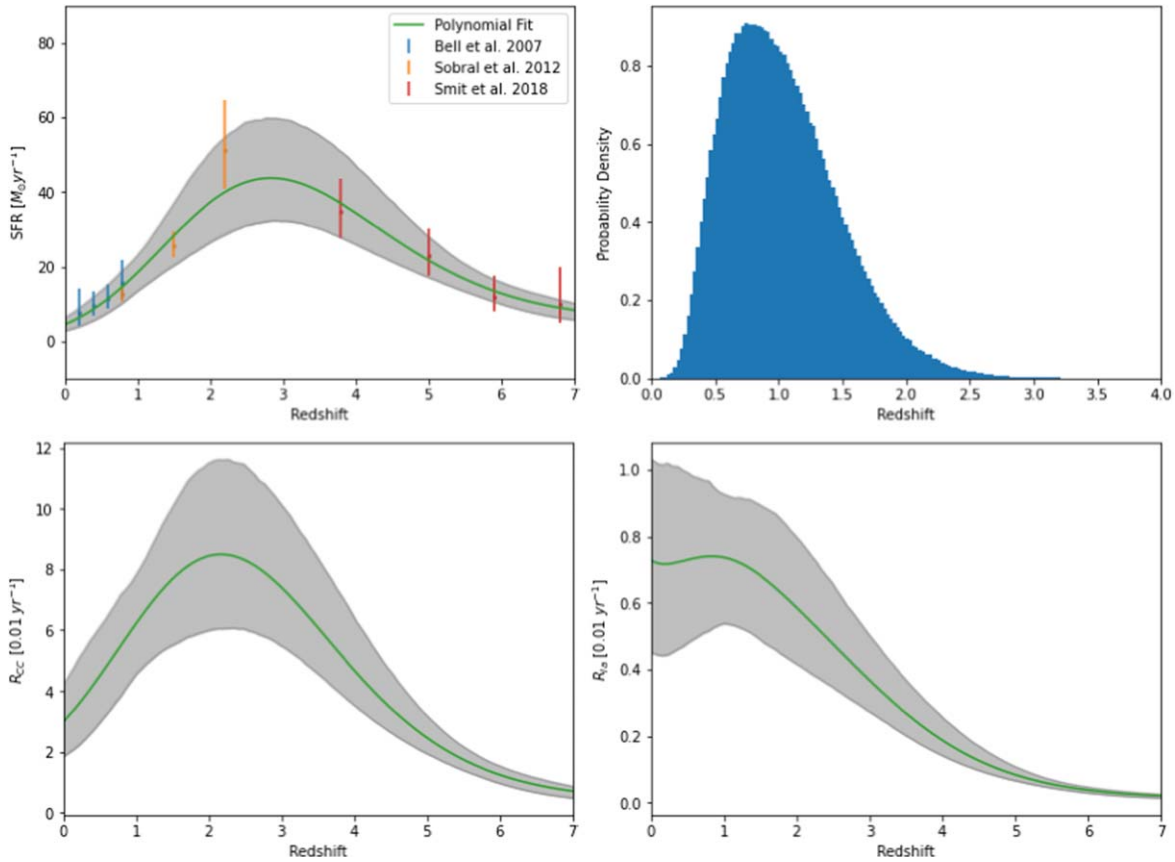

Figure 3. Distributions used to simulate the necessary parameters to calculate the expected results of our pipeline's deployment. Top left-hand panel: Star formation rate vs. redshift, with the polynomial fit (degree of 3) to the data (Bell et al. 2007, Smit et al. 2012; Sobral et al. 2012). The uncertainty bounds (shown in gray) are generated using the the covariance matrix of the resulting fit. Top right-hand panel: The assumed source redshift distribution (see text). Bottom left-hand panel: CC SNe rates verses redshift. The same polynomial fit and uncertainty bounds are used to calculate these rates, according to Equations (1) and (2). Bottom right-hand panel: SNe Ia rates vs. redshift. The same polynomial fit and uncertainty bounds are used to calculate these rates, according to Equations (2), (3), and (4).

target in these fields. Our pipeline has been applied to DECaLS and these deep observations.

Since we take the approach of a targeted search, we compile a database of 5807 strong lenses and candidates found within DECaLS, with the majority from Huang et al. (2020), Huang et al. (2021), and Storfer et al. (2022), and the rest from Moustakas (2012), Carrasco et al. (2017), Diehl et al. (2017), Jacobs et al. (2017), Pourrahmani et al. (2018), Sonnenfeld & Leauthaud (2018), Wong et al. (2018), and Jacobs et al. (2019). Note that Storfer et al. (2022) only included C-grade or above candidates. However on the project's website,[8] they also included D-grade candidates. These receive numerical scores of 1 or 1.5.[9] Here we include those with the higher numerical score of 1.5, which in this paper we will call D+.

3. Pipeline

The general framework of the pipeline consists of image reprojection and reference image generation (Section 3.1), image subtraction (Section 3.2), and source detection and grouping (Section 3.3) for each of 5807 lensing systems and candidates.

3.1. Image Reprojection and Reference Image Generation

The pipeline first collects all of the relevant exposures from DR9 for all targets. The images are then reprojected onto the same World Coordinate System (WCS) orientation, with the system centered in each 801×801 pixel ($216\farcs27 \times 216\farcs27$) cutout. For each filter, we use the median coadd as the reference image to reduce the influence of a potential transient (and other time-dependent systematics, such as cosmic rays). These steps are done using the Montage software package (Jacob et al. 2010). For exposures of the same band within 1.5 days of each other, we combine them as a mean coadd because we do not expect a significant change in the flux for an astrophysical transient in such a short time frame, while increasing detection efficiency.

3.2. Image Subtraction

To find transients, we perform image subtraction between each exposure and reference image for the same filter. This pipeline uses two different image subtraction algorithms: that of Bramich (2008; henceforth B08), and Saccadic Fast Fourier Transform (SFFT; Hu et al. 2022).

The B08 algorithm fits for a spatially varying kernel that attempts to convolve the reference image to appear comparable to the image of each exposure (science image). B08 uses delta functions as its basis functions, and thus fits for every pixel in the kernel to minimize the χ^2 of the difference image between

[8] https://sites.google.com/usfca.edu/neuralens
[9] C. Storfer, private communication.

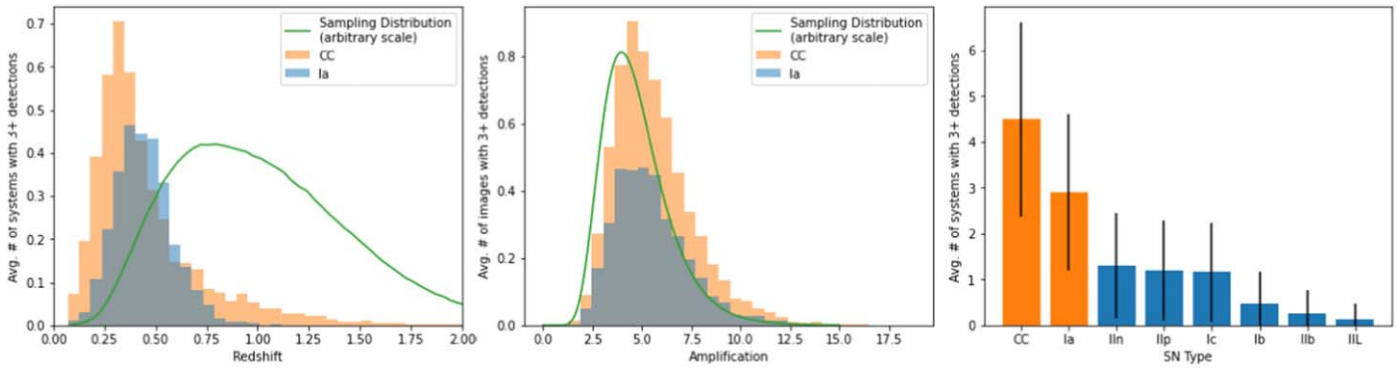

Figure 4. Results of the 1000 simulated runs for finding lensed SNe in the 5807 targeted systems. Left-hand panel: A histogram illustrating the average number of systems (out of 5807) with three or more detections verses redshift, as well as the scaled sampled source redshift distribution outlined in green. The redshift distribution of the detectable systems is clearly lower than the distribution that we sample from due to detection limits. The integrals of the distributions are shown in Table 2. Center panel: A histogram illustrating the number of systems with three or more detections verses magnification, the magnification distribution that we sample from is outlined in green. There is a slight bias toward higher magnifications, as would be expected. Right-hand panel: A bar diagram illustrating the representation of each type of simulated SNe in the systems with three or more detections.

Table 1
Supernova Simulation Percentages and Brightness Parameters

SNe Type (1)	$\overline{M_B}$ (2)	σ (3)	% Rate of CC Occurrence (4)	SNCosmo Template (5)	Template (6)
IIp	-16.75 ± 0.37	0.98	55.83	nugent-sn2p	Gilliland et al. (1999)
Ic	-17.66 ± 0.40	1.18	17.00	nugent-sn1bc	Levan et al. (2005)
IIb	-16.99 ± 0.45	0.92	12.43	v19-2006t-corr	Vincenzi et al. (2019)
Ib	-17.45 ± 0.33	1.12	9.00	nugent-sn1bc	Levan et al. (2005)
IIL	-17.98 ± 0.34	0.86	3.34	nugent-sn2l	Gilliland et al. (1999)
IIn	-18.53 ± 0.32	1.36	2.40	nugent-sn2n	Gilliland et al. (1999)
Ia	-19.25 ± 0.20	0.50	⋯	salt3	Kenworthy et al. (2021)

Note. This table shows the supernova-related parameters used in the pipeline simulated results. As with Craig et al. (2021), the rate for 87A-like SNe (1%) is uniformly distributed across IIp, IIb, and IIL SNe. All $\overline{M_B}$ and σ values are reported in Richardson et al. (2014). CC SNe percentages are reported in Eldridge et al. (2013).

the science image and the convolved reference image. Because it fits for every pixel in the kernel, it makes no assumption on the functional form of the fitted kernel.

SFFT is a fully-Fourier implementation of image subtraction. SFFT performs Fourier transforms on both reference and science images, and fits for a convolutional, while also spatially varying the kernel for the reference image (thus similar to B08, but in the Fourier space).

Although we have experimented with other well-known image subtraction algorithms (Alard 2000; Zackay et al. 2016), we found that B08 and SFFT best suit this pipeline's application. Alard (2000; henceforth A00), implemented in the HOTPANTS package (Becker 2015), is widely used for large surveys and is very similar to B08. The main difference is that A00 uses a set of Gaussian priors, and thus assumes a functional form of the convolutional kernel. Rather than fitting for each pixel of the kernel (as with B08), A00 only has to fit for the Gaussian parameters, which leads to a significant speed-up for large scale surveys. However, since we are conducting a targeted search, our pipeline can afford to use the slower and more flexible B08 algorithm. Zackay et al. (2016; also known as ZOGY) takes a different approach to the image subtraction problem by utilizing the concept of cross-filtering (i.e., two separate convolutional kernels) for the difference image generation and to solve both kernels in Fourier space. We opt to use the SFFT algorithm because the results indicate an improvement to addressing photometric mismatch within image subtraction over ZOGY. Despite appearing as a publication only recently, SFFT has been extensively applied to time-domain observations.[10] For almost all cases, we find that the SFFT algorithm produces cleaner and more accurate image subtraction when compared to B08. Thus, although both algorithms are used for transient detection, we use the SFFT difference images for all subsequent photometry and detection presentation in this paper.

3.3. Source Detection and Grouping

After generating difference images with both image subtraction algorithms, we use a Python implementation (SEP; Barbary 2018) of the source extraction algorithm from Bertin & Arnouts (1996) to detect any potential sources in the difference images, with thresholds ranging from 1.0 to 2.5σ in 0.25 increments as determined by SEP (with detections $>2.5\sigma$ treated as the same detection level as 2.5σ). Henceforth, we denote a detection in a single difference algorithm as a "sub-detection" (a given transient event in a single exposure can generate two sub-detections, by being detected in difference images produced by both the B08 and SFFT algorithms). The sub-detections (from both subtraction algorithms, across all bands, and across all exposures) are then grouped together spatially and temporally. These groupings contain the sub-detections that are within three pixels (0.″8) of

[10] L. Wang, private communication.

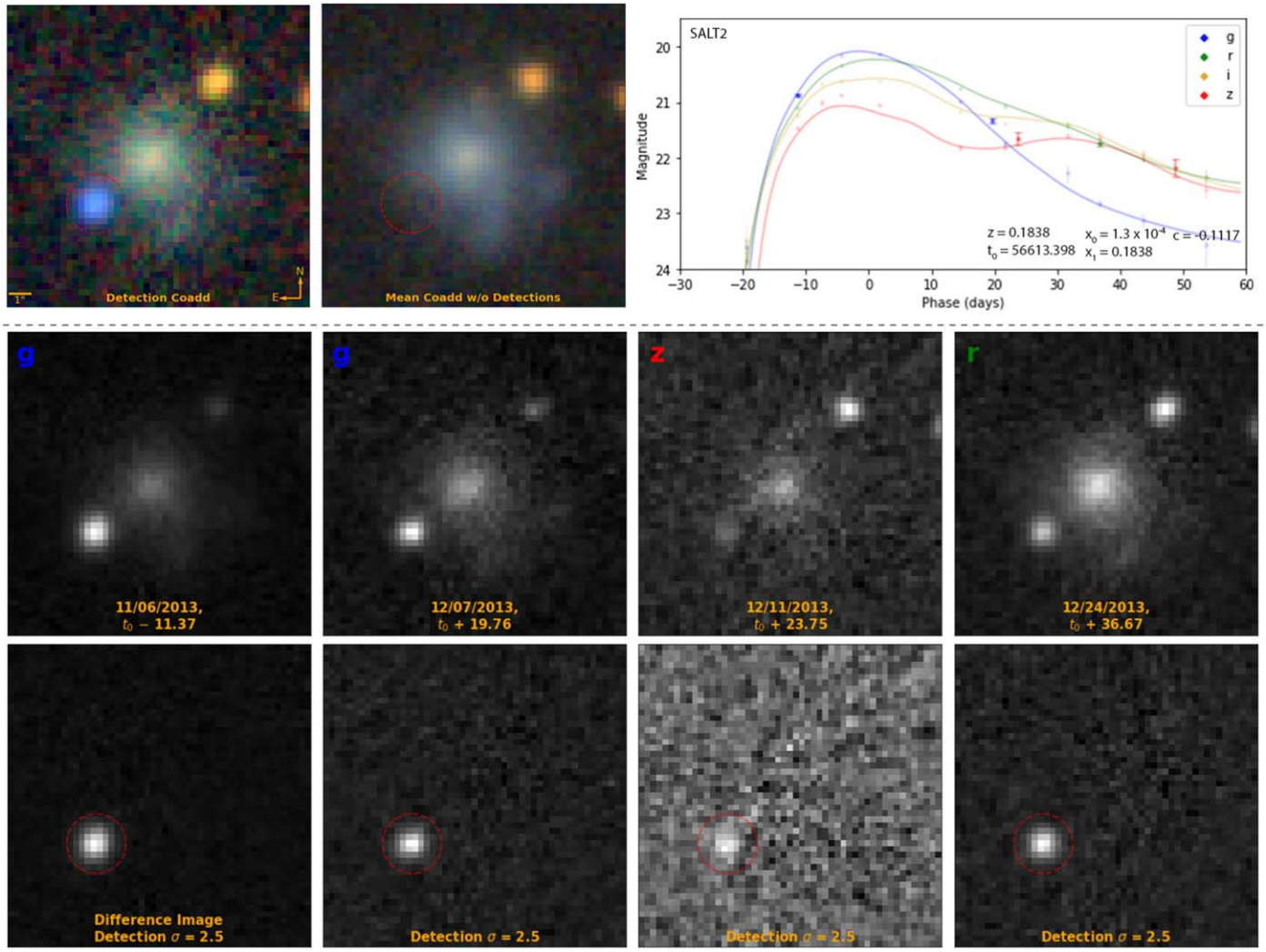

Figure 5. Detection and photometry results of our pipeline, for a known SN Ia at (R.A., decl.) = (7.6006, −42.2977), $z = 0.1838$. Top left-hand panel: The mean coadded RGB (generated from *g*, *r*, *i*, and *z* bands; see text) image, which is generated using exposures that include the SN event. Top middle panel: The mean coadded RGB image, generated using exposures that exclude the supernova event. The dotted-red circle indicates the location of the SN Ia event. Top right-hand panel: Photometry for the detected SN from the SFFT difference images (solid points), plotted with DES photometry (fainter points) for this SN and the best-fit DES light curve. We note the good agreement between our results and DES. Below the dotted line: examples of single band images in chronological order, alongside its corresponding SFFT difference image (bottom) and SN detection, labeled with band, date of exposure, the phase, and the σ-level of detection.

one another and are within 50 days of other sub-detections in the group. If a given group has less than three sub-detections, then the pipeline disregards them. If a group has three or more difference image sub-detections, then it is labeled as a possible transient detection. That is, an event must be observed by DECaLS at least twice, in at least two separate exposures, to be labeled as a possible transient detection.[11] This reduces the number of false detections (from noise, cosmic rays, CCD artifacts, etc.) and inconclusive events, and improves the overall quality of detections that will be visually examined. Had we conducted this search live, then $\mathcal{O}(100)$ 2+ sub-detection groups would have been identified, most of which would warrant follow-up observations.

The entire process typically takes about two hours to run per system, with approximately one hour for data collection and reprojection and one hour for image subtraction. To run this pipeline on 5807 systems (approximately 120,000 individual exposure cutouts), parallelization is necessary. The full deployment is performed on the National Energy Research Scientific Computing Center (NERSC) Cori supercomputer. Using 20 nodes, 32 CPUs per node, and one thread per CPU, this requires that each thread run 9 to 10 systems, taking a total of 18 to 20 hr. SFFT is capable of being run on GPUs with a significant speed gain. We will take advantage of this capability in our pipeline in the near future.

Twenty-five of the 5807 candidate systems lie within a deep field survey footprint, and thus each has 800+ individual exposures. For these systems, the amount of memory and time required makes naively running the pipeline infeasible. Instead, we opt to split the exposures from these systems into smaller groups of temporally-similar exposures and run the pipeline on each possible pair of groups for all permutations. The groups were created such that every exposure appears in at least three groups, which ensures that the pipeline does not miss a possible lensed transient in any exposure. We do not find any lensed transients within the 25 deep field systems.

[11] For example, at the threshold (inclusive), a group with three sub-detections can correspond to two or three detections (i.e., in two or three exposures). In the case of two detections, one of them is detected by both subtraction algorithms. In the case of three detections, each is detected by a single subtraction algorithm.

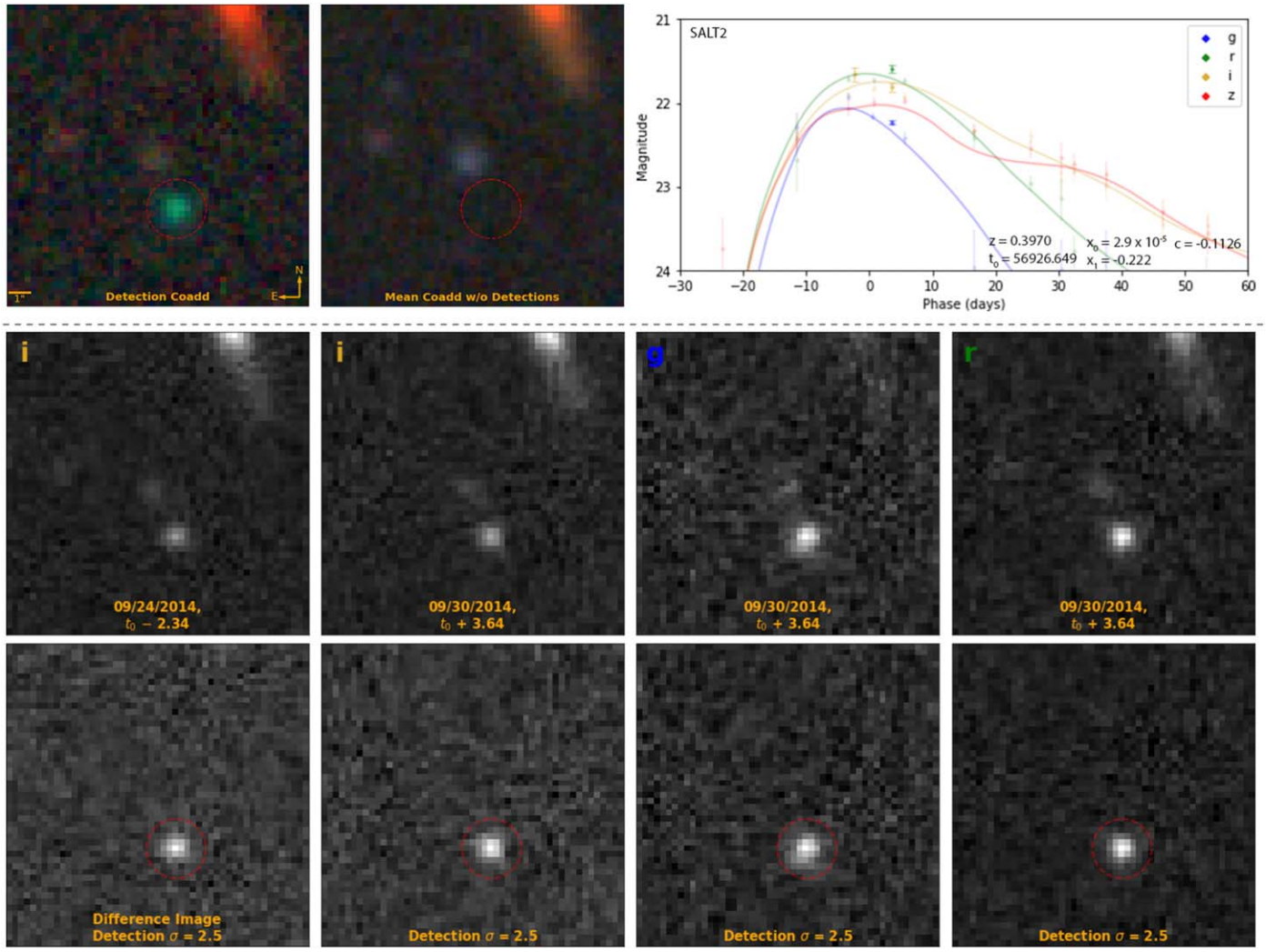

Figure 6. Detection and photometry results of our pipeline for a known SN Ia at (R.A., decl.) = (41.0802, −0.4498), $z = 0.397$. For the arrangement of panels, see the caption of Figure 5.

Table 2
Expected Numbers of Lensed SN Detections

Number of Detections (1)	L-SNe Ia (2)	L-CC SNe (3)
1 or more	16.49 ± 4.14	22.74 ± 4.85
2 or more	**6.58 ± 2.57**	**9.35 ± 3.08**
3 or more	**2.90 ± 1.68**	**4.53 ± 2.12**
4 or more	1.31 ± 1.16	2.43 ± 1.55
5 or more	0.63 ± 0.80	1.42 ± 1.16
6 or more	0.30 ± 0.53	0.82 ± 0.87
7 or more	0.14 ± 0.36	0.48 ± 0.68

Note. This table shows the final results of the 1000 simulations for finding lensed supernovae in the 5807 lenses and candidates. To compare this forecast with our targeted search, we boldface the rows for two and three detections or more (see text).

3.4. Selection Criteria

Human inspection of the pipeline results is necessary to validate the pipeline detections. For first round visual inspection, for each system two initial grades are assigned regarding its most convincing group of detections. First, we assign a location grade to assess how close the detection location lies relative to any putative lensed features. We use this grade to filter out transient candidates that are clearly not lensed. Second, a transient grade is given by the likelihood that the detection is a transient.

Most systems were not given any grades, i.e., there were no convincing detections for these systems. Since our pipeline's focus is to detect transients that are lensed, very obvious transients far from any lensing features are given high transient grades but low location grades. By using these metrics, we identified the most promising lensed transient candidates.

We apply our pipeline to these select candidates a second time, while removing all exposures that contain the suspected transient detection from the median coadd, to generate a reference that is free of possible transient light. Preliminary Legacy Surveys DR10 data are included in this second run. The new data also includes observations from the DECam *i* and *Y* bands. Using Point Spread Functions (PSFs) that are modeled from isolated stars within the entire CCD exposure brick,[12] PSF photometry is then applied to all SFFT difference images. For exposures that we are not able to fit with a PSF at the detection location (i.e., non-detections that take place well before or after the peak of the suspected transient event), aperture photometry is applied to the location

[12] https://www.legacysurvey.org/dr10/description/

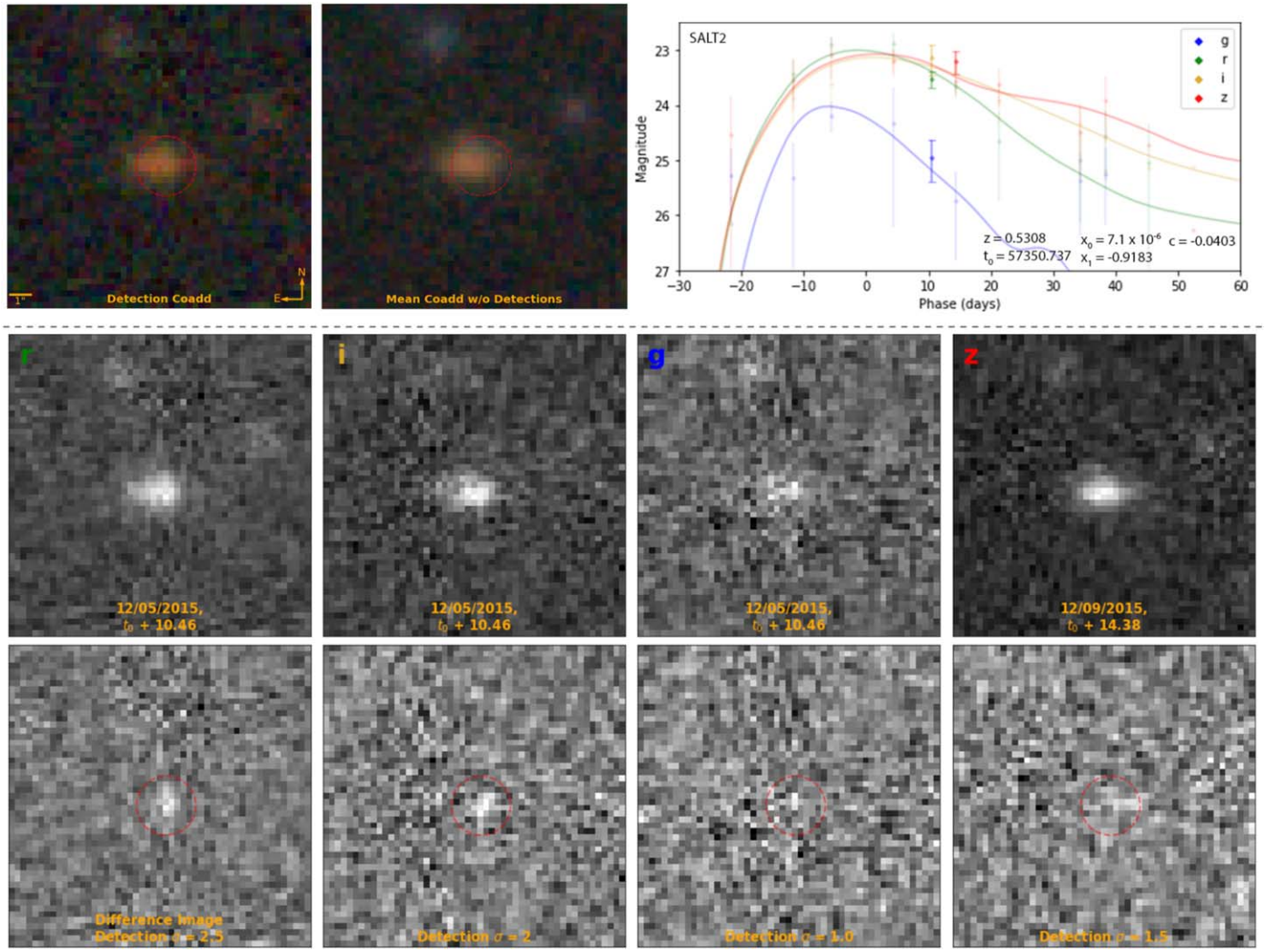

Figure 7. Detection and photometry results of our pipeline for a known SN Ia at (R.A., decl.) = (41.2919, −1.5649), $z = 0.5308$. For the arrangement of the panels, see the caption of Figure 5.

of the possible transient to establish a baseline flux for light-curve fitting. For promising candidates, we apply our own final set of criteria to select the candidates with the highest potential of being a L-SN:

1. *Strong Lensing Plausibility* - Because the lens candidates that are included in the search are from multiple publications and different search efforts, we determine the likelihood that a candidate is a strong lensing system. The criteria that we use are similar to those in Huang et al. (2021).
2. *Asteroid Filtering* - If there are only a few detections minutes apart in a given night, and no detections after that night, then this is an indication that transient is possibly an asteroid. To confirm this, we can approximate the speed of the asteroid between detections (using PSF fitting to precisely locate the punitive asteroid) and compare it to the speed of a typical main-belt asteroid.
3. *Location Consideration* - In combination with the location grade, we also take into consideration surrounding objects (in some cases, modeling their light profiles) and assess the overall probability of the transient candidate being lensed based on the detection location.
4. *Light Curve Fit Quality* - To narrow the possible identities of the detection, we fit a SALT3 (Kenworthy et al. 2021) SN Ia light-curve model and 161 different core-collapse (CC) SN models to the observed photometry. Because the survey data is sparse and the search is retrospective, we use a photometric redshift prior or a spectroscopic redshift in the fitting process. A fit with low χ^2/DOF is an indication of a possible identity. When a light-curve model fits the photometry well, we also assess whether the best-fit light-curve model parameters are reasonable (e.g., the SALT2 x_1 parameter is generally between -3 and 3).
5. *Amplification/Hubble Diagram Residual* - From the best-fit light-curve models, we can further deduce whether the transient is amplified, and if the amplification is reasonable given the system configuration. For the case of a SN Ia, we can find its Hubble residual and determine the amplification (if any).

Although unlikely, there is a possibility that one or some of our lensed transient candidates are rare instances of micro-lensed high-redshift stars (e.g., Kelly et al. 2018 and Welch et al. 2022). However, this would be extremely coincidental because most of our targets and candidates are single-galaxy-

Table 3
Lensed and Unlensed Supernova Candidates

System Name (1)	Overall Grade (2)	Total Number of Exposures (g, r, i, z, Y) (3)	Number of PSF Photometry Exposures (g, r, i, z, Y) (4)	Distance Grade (5)	Postulation (6)	Shown (7)	Redshift Used in LC Prior (8)	Best-fit z_{SN} (9)	χ^2/DOF (10)	Hubble Residual (11)	Required Amplification (12)	Model Fitting Grade (13)	Reason (14)
DESI-344.6252-48.8977	A	(10, 8, 7, 7, 7)	(1, 2, 1, 0, 1)	A	uL-SN Ia	Y	0.374 ± 0.053	0.299 ± 0.021	5.47	1.10 ± 0.24	⋯	D	[1] [2]
					L-SN Ia	Y	1.188 ± 0.255	0.833 ± 0.042	2.81	-2.29 ± 0.30	$8.23^{+2.61}_{-1.98}$	A	
					uL-CC SN		0.374 ± 0.053	0.393 ± 0.026	4.93	⋯	⋯	D	[1]
					L-CC SN	Y	1.188 ± 0.255	0.731 ± 0.049	2.75	⋯	$40.28^{+52.80}_{-22.89}$	B	
DESI-058.6486-30.5959	B	(10, 11, 9, 9, 6)	(2, 2, 0, 0, 0)	B	uL-SN Ia	Y	0.1702	0.1702	1.73	0.66 ± 0.20	⋯	B−	
					L-SN Ia		0.6735	0.6735	4.61	-3.00 ± 0.04	$15.82^{+0.54}_{-0.52}$	C	[1]
					uL-CC SN		0.1702	0.1702	3.40	⋯	⋯	C	[1]
					L-CC SN	Y	0.6735	0.6735	2.43	⋯	$27.91^{+82.66}_{-20.92}$	B+	
DESI-308.7726-48.2381	B	(12, 12, 10, 15, 8)	(0, 1, 1, 1, 0)	A	uL-SN Ia		0.473 ± 0.032	0.448 ± 0.034	4.59	-1.54 ± 0.61	⋯	D	[1] [2]
					L-SN Ia	Y	⋯	0.869 ± 0.021	2.05	-2.91 ± 0.32	$14.62^{+5.02}_{-3.74}$	B+	
					uL-CC SN	Y	0.473 ± 0.032	0.465 ± 0.026	4.88	⋯	⋯	C	[1]
					L-CC SN	Y	⋯	0.828 ± 0.057	2.98	⋯	$15.61^{+45.94}_{-11.66}$	B−	
DESI-034.3625-35.3563	C	(11, 11, 10, 8, 9)	(2, 2, 1, 0, 0)	A	uL-SN Ia	Y	0.240 ± 0.008	0.238 ± 0.011	1.31	0.20 ± 0.25	⋯	A	
					L-SN Ia		⋯	0.294 ± 0.026	1.64	-0.09 ± 0.24	$1.09^{+0.27}_{-0.22}$	D	[3]
					uL-CC SN		0.240 ± 0.008	0.242 ± 0.011	1.71	⋯	⋯	B	
					L-CC SN	Y	⋯	0.530 ± 0.218	1.97	⋯	$35.16^{+50.83}_{-20.79}$	C	[1]
DESI-035.1374+00.4676	C	(21, 16, 7, 14, 9)	(1, 0, 1, 1, 0)	C	uL-SN Ia	Y	0.269 ± 0.007	0.269 ± 0.008	1.20	0.27 ± 0.33	⋯	A	
					L-SN Ia		0.776 ± 0.118	0.727 ± 0.056	1.25	-1.90 ± 0.41	$5.74^{+2.63}_{-1.81}$	B	
					uL-CC SN		0.269 ± 0.007	0.269 ± 0.005	1.84	⋯	⋯	B	
					L-CC SN	Y	0.776 ± 0.118	0.795 ± 0.050	0.44	⋯	$18.97^{+55.29}_{-14.13}$	A	
DESI-052.0083-37.2049	C	(43, 11, 64, 9, 4)	(3, 2, 1, 2, 0)	A	uL-SN Ia	Y	0.292 ± 0.029	0.333 ± 0.023	1.48	0.47 ± 0.16	⋯	B	
					L-SN Ia		⋯	0.357 ± 0.013	1.46	0.37 ± 0.10	$0.71^{+0.07}_{-0.07}$	D	[3]
					uL-CC SN		0.292 ± 0.029	0.316 ± 0.018	2.07	⋯	⋯	D	[1]
					L-CC SN	Y	⋯	0.450 ± 0.018	1.54	⋯	$12.60^{+18.20}_{-7.45}$	B	
DESI-084.8493-59.3586	D	(9, 10, 6, 9, 3)	(3, 3, 0, 2, 0)	D	uL-SN Ia	Y	0.361 ± 0.015	0.365 ± 0.008	1.61	-0.15 ± 0.09	⋯	B	
					L-SN Ia		0.593 ± 0.146	0.391 ± 0.011	1.41	-0.20 ± 0.12	$1.20^{+0.12}_{-0.11}$	D	[3]
					uL-CC SN		0.361 ± 0.015	0.406 ± 0.006	3.64	⋯	⋯	D	[1]
					L-CC SN	Y	0.593 ± 0.146	0.819 ± 0.064	2.02	⋯	$86.05^{+153.15}_{-55.10}$	C	[1]

Table 3
(Continued)

System Name (1)	Overall Grade (2)	Total Number of Exposures (g, r, i, z, Y) (3)	Number of PSF Photometry Exposures (g, r, i, z, Y) (4)	Distance Grade (5)	Postulation (6)	Shown (7)	Redshift Used in LC Prior (8)	Best-fit z_{SN} (9)	χ^2/ DOF (10)	Hubble Residual (11)	Required Amplification (12)	Model Fitting Grade (13)	Reason (14)
DESI-015.8465-50.5450	N/A	(9, 7, 4, 9, 5)	(1, 1, 0, 0, 0)	N/A	uL-SN Ia	Y	0.301 ± 0.026	0.373 ± 0.131	0.58	-0.91 ± 1.52	⋯	B	
					L-SN Ia		⋯	⋯	⋯	⋯	⋯	⋯	
					uL-CC SN	Y	0.301 ± 0.026	0.289 ± 0.036	1.30	⋯	⋯	B	
					L-CC SN		⋯	⋯	⋯	⋯	⋯	⋯	

Note. Summary table for our eight lensed and unlensed supernova candidates. Column 2: A wholistic grade on how likely a detection a L-SN is, based on the criteria in Section 3.4. Column 5: The distance grade, based on the location of the transient (for first round visual inspection, Section 3.4). Column 6: The four postulations for each candidate, uL-SN Ia, L-SN Ia, uL-CC SN, and L-CC SN. Column 7: Only light-curve models for postulations marked with "Y" are shown in this column (in Section 6.1 and Appendix B, above and below the horizontal line, respectively). Column 8: For redshift prior in the fitting process, we use photometric redshifts from Zhou et al. (2020), shown with three decimal places and uncertainties, or fix them to be the spectroscopic redshifts from A. Cikota et al. (2023, in preparation), shown with four decimal places and no uncertainties. Columns 14 and 15: Each postulation is given a grade based on the light-curve fitting and/or the Hubble residuals, as well as reasons for a C or D grade. The reasons correspond to the following: [1] poor fit in comparison to the other postulations, [2] large Hubble residual in the case of uL-SN Ia, and [3] best-fit z_{SN} too close to the lens photo$z$, and hence inconsistent with a lensing postulation (note that, to be complete, we nevertheless include the best-fit z_{SN} and magnification information).

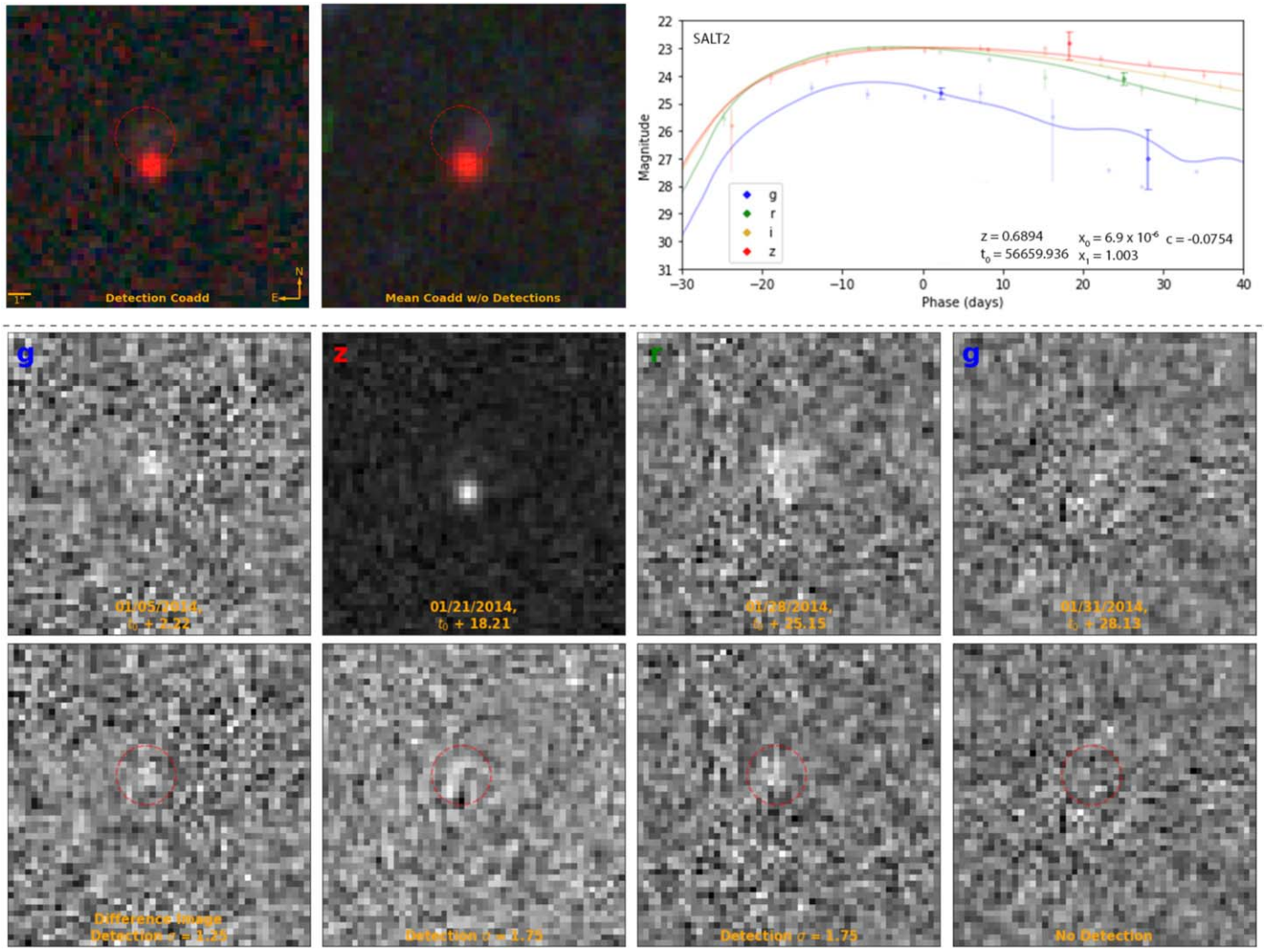

Figure 8. Detection and photometry results of our pipeline for a known SN Ia at (R.A., decl.) = (53.3699, −28.4430), $z = 0.6894$. For the arrangement of the panels, see the caption of Figure 5. Note that there is no detection for the last exposure. We therefore performed aperture photometry at the detected location of the transient.

scale lenses. In contrast, all discovered microlensed high-redshift stars are lensed by galaxy clusters, which boasts much higher magnification, allowing a significantly larger strong lensing cross-section of near-infinite magnification. However, with only the ground-based Legacy Imaging Surveys data present for our candidates, we are unable to accurately model these lensing systems and thus cannot tell if a posited transient lies near the critical curve. Lastly, the photometric data from DR9 and DR10 is too sparse to support this claim. Therefore, while we do not disqualify the possibility of a microlensed high-redshift star, we will not further entertain the postulation.

4. Expectations

To assess the feasibility of finding L-SNe Ia in the DESI Legacy Imaging Surveys, we can simulate SNe Ia light curves at various redshifts and lensing amplifications of a lensed SN, and calculate the amount of time a given simulated SNe will be detectable in the DECam g, r, and z bands. We will be using the following values: 23.47, 23.43, and 21.63 for g, r, and z bands respectively, based on the 5σ PSF detection thresholds from Dey et al. (2019), adjusted to the nominal time of 90 s per exposure in DR9. We use SNCosmo (Barbary 2014) to simulate SNe Ia light curves, based on the SALT3 model (Guy et al. 2007; Kenworthy et al. 2021). We assume $x_1 = 0$ and $c = 0$ for the SALT3 parameters. Figure 2 illustrates the length of time that a L-SN Ia is detectable in the DECam g, r, and z filters across a range of reasonable redshifts and amplifications. This initial investigation indicated that L-SN Ia are discoverable in the Legacy Surveys and motivated this search.

Since a careful forecast of lensed SN rates is beyond the scope of this paper, we use the formulation of Shu et al. (2018, henceforth S18) to provide a first-order estimation. Following S18, we simulate the star formation rate for a source galaxy at a given redshift to sample the SN rates.

We can now estimate the number of lensed Type Ia and CC SNe that we expect to find in our retrospective search. We start by simulating the source redshift of a given lensing system. Given that most of our lens candidates are from Huang et al. (2020, 2021), and Storfer et al. (2022), we generalize the lens galaxy spectroscopic or photometric redshifts from those candidates as the lens galaxy redshift distribution in our simulations. We then multiply this with a truncated normal distribution $\mathcal{N}(2, 0.5)$, with a lower bound at 1, to represent the source galaxy redshift distribution. Figure 3 shows the source galaxy redshift distribution from which we sample for our simulations.

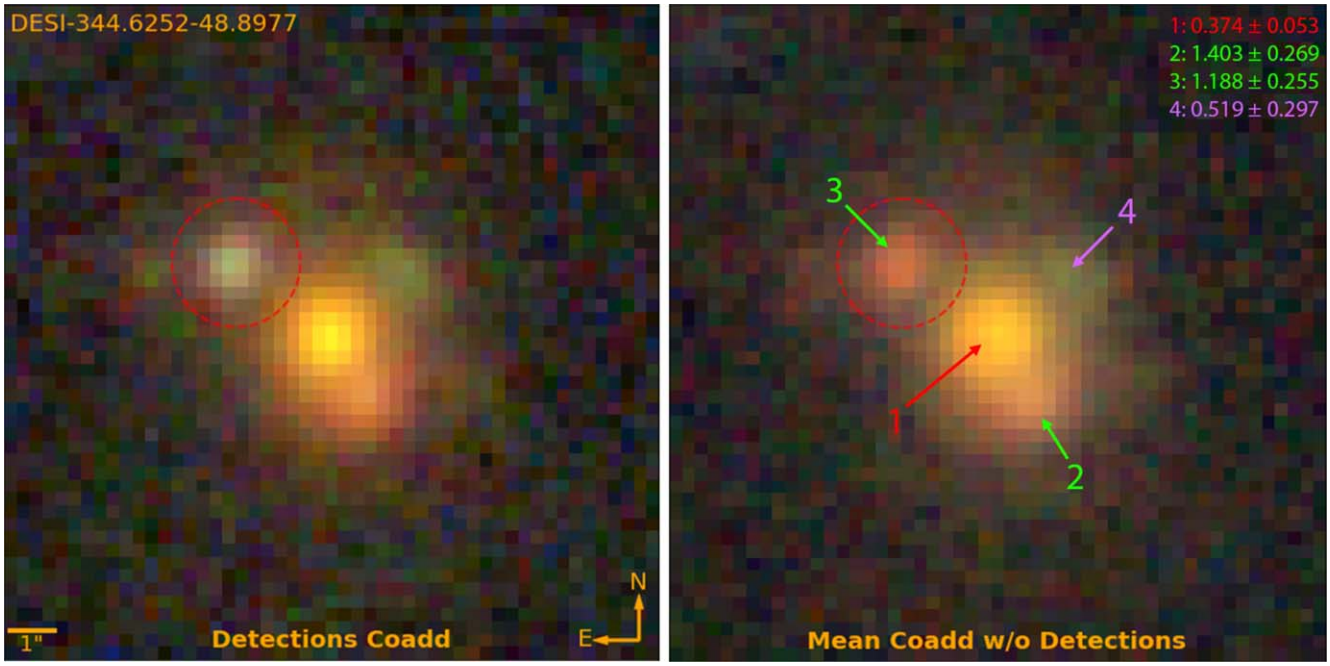

Figure 9. Coadded RGB images (using *g*, *r*, *i*, and *z* bands) of L-SN Ia candidate DESI-344.6252-48.8977 with and without the transient detection (red-dotted circle) exposures. The arrows are color coded as in the following postulated scenario: the lens galaxy is red, the lensed source galaxy is green, and a possible second lensed source or an interloper is purple. Photometric redshifts are displayed on the top right-hand corner. The posited lens galaxy has a photo*z* of 0.374 ± 0.053 and the posited lensed images have photo*z*es of 1.188 ± 0.255 and 1.403 ± 0.269.

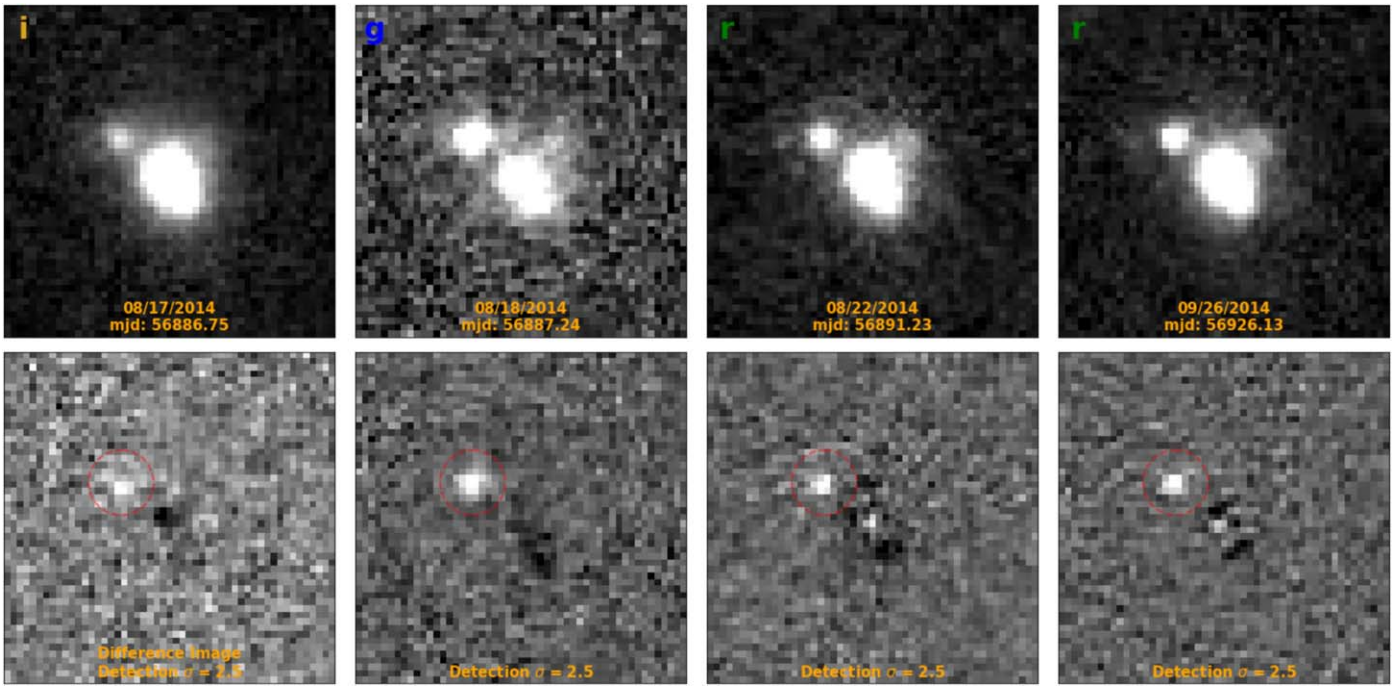

Figure 10. Detection exposures for the transient in DESI-344.6252-48.8977 in chronological order. Top row: Single pass images. Bottom row: Corresponding differencing images from SFFT, where the red circle indicates the location of the detected transient.

Using SFR estimations of varying redshifts (from $z = 0.2$ to $z = 6.8$) from Bell et al. (2007), Smit et al. (2012), and Sobral et al. (2012), we fit a polynomial function (degree of three, using Numpy's polyfit algorithm) to $\log_{10}(\text{SFR})$, with the uncertainties given by the polynomial fit covariance matrix. We sample SFRs at a given source redshift from this polynomial model.

From S18, we can convert SFRs to CC SNe rates:

$$R_{\rm CC} = 0.0068 M_{\odot}^{-1} \frac{\rm SFR}{1 + z_S} [\rm yr^{-1}] \quad (1)$$

The CC SNe rates are the broken down into sub-rates for the different types, based on the percentages in Table 1.

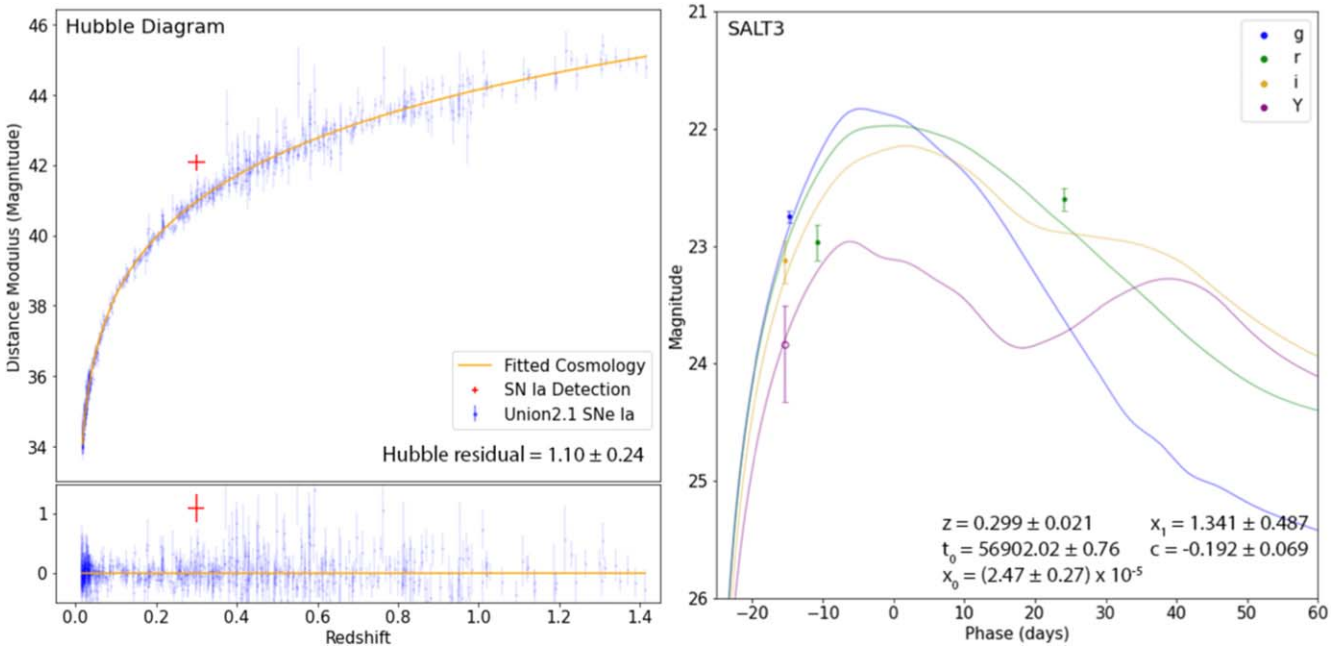

Figure 11. Best-fit SALT3 model for DESI-344.6252-48.8977 with a lens photo$z$ redshift prior of 0.374 ± 0.053. For this and Figures 12 and 13, solid photometry points correspond to the detection passes shown in Figure 10.

We can estimate the SFH from the functional form (Madau & Dickinson 2014), normalized by the recent SFR (S18):

$$\mathrm{SFR}(t(z)) = \mathrm{SFR} \times \left(\frac{1+z(t)}{1+z_S}\right)^{2.7} \left(\frac{1+\left(\frac{1+z_S}{2.9}\right)^{5.6}}{1+\left(\frac{1+z(t)}{2.9}\right)^{5.6}}\right) \quad (2)$$

From S18, by assuming a delay time (t_D) distribution, f_D:

$$f_D(t_D) \propto t_D^{-1.07}, \quad (3)$$

we can estimate SN Ia rates:

$$R_{Ia} = 0.00084 M_\odot^{-1} \frac{\int_{0.1}^{t(z_S)} \mathrm{SFR}(t(z_S) - t_D) f_D(t_D)\, dt_D}{(1+z_S)\int_{0.1}^{t(z=0)} f_D(t_D) dt_D} [\mathrm{yr}^{-1}], \quad (4)$$

Each system is assumed to have two or four lensed images (with probabilities of 0.7 and 0.3 respectively; Oguri & Marshall 2010), and each image has a magnification sampled from a lognormal distribution (mean = 1.5 and standard deviation = 0.35), with an expected magnification of 4.765. As a context, Shu et al. (2021) used a constant magnification of 5 for their targeted rates estimations, whereas Craig et al. (2021) performs a targeted estimate on a set of 40 strong lenses (from Shu et al. 2017) with magnifications ranging [2, 105], with a median of 6.5. We sample time delays between each lensed image from $\mathcal{N}(36, 4)$ days (Craig et al. 2021).

We do not simulate the times of exposures but rather use the true exposure times of our 5807 targets, observed in the DECam g, r, and z bands. Conservatively, we assume 90 s for each exposure (because while an exposure can occasionally be as low as 60 s, the vast majority of the exposures are 90 s or longer).

Assuming that all 5807 systems in our catalog are real lensing systems, we simulate the expected results for each system, using their time of exposures in the DECam g, r, and z bands for our search. We sample their source redshifts, number of lensed images, lensing amplifications, lensing time delays, and star formation rates. Using these sampled values, we calculate the Ia and CC SN rates. Based on these rates, we simulate SNe across the duration of the DR9 observation range (from the date of the first exposure −100 days to the date of the last exposure +100 days; the time frame being significantly larger than the typical width of Ia and CC light-curve widths). In Table 1 gives the SNCosmo light-curve models used during simulations, as well as the absolute B band magnitude distributions. For simulated SNe Ia, we sample the following parameters as: $c \sim \mathcal{N}(0, 0.1)$ and $x_1 \sim \mathcal{N}(0, 1)$ (Guy et al. 2010; Scolnic et al. 2022). For CC SNe, we subdivide and simulate them as Ib, Ic, IIn, IIp, IIb, or IIL, with their M_B sampled from Table 1. For all simulated SNe, we assume a small amount of host-galaxy dust ($E(B-V) \lesssim 0.02$). Finally, we check if a lensed SN image for a given system in a given band is above the detection limit.

The full simulation of our pipeline (on the 5807 target systems) was parallelized and run 1000 times on NERSC to estimate the expected SNe rates. The final results are shown in Figure 4 and Table 2. To reliably find transients, we require a threshold of three sub-detections or more. As mentioned earlier (Section 3.3), depending on the system, this means at least two or three detections, corresponding to the highlighted rows in Table 2.

5. Testing Detection and Photometry Pipelines on Known SNe Ia

To test the performance of our pipeline, we apply it to photometric data from known SNe Ia discovered in DES (Smith et al. 2020; Abbott et al. 2021). From the DES SNe Ia, we select well-observed and modeled SNe that had at least two DR10 exposures within −15 to +30 days of the time of peak brightness in B band (or t_0). This results in a set of 32 SNe Ia. The SNe were previously modeled using SALT2 (extended by Hounsell et al. 2018) parameterization,[13] with a host-galaxy dust extinction

[13] https://github.com/sam-dixon/sncosmo_lc_fits

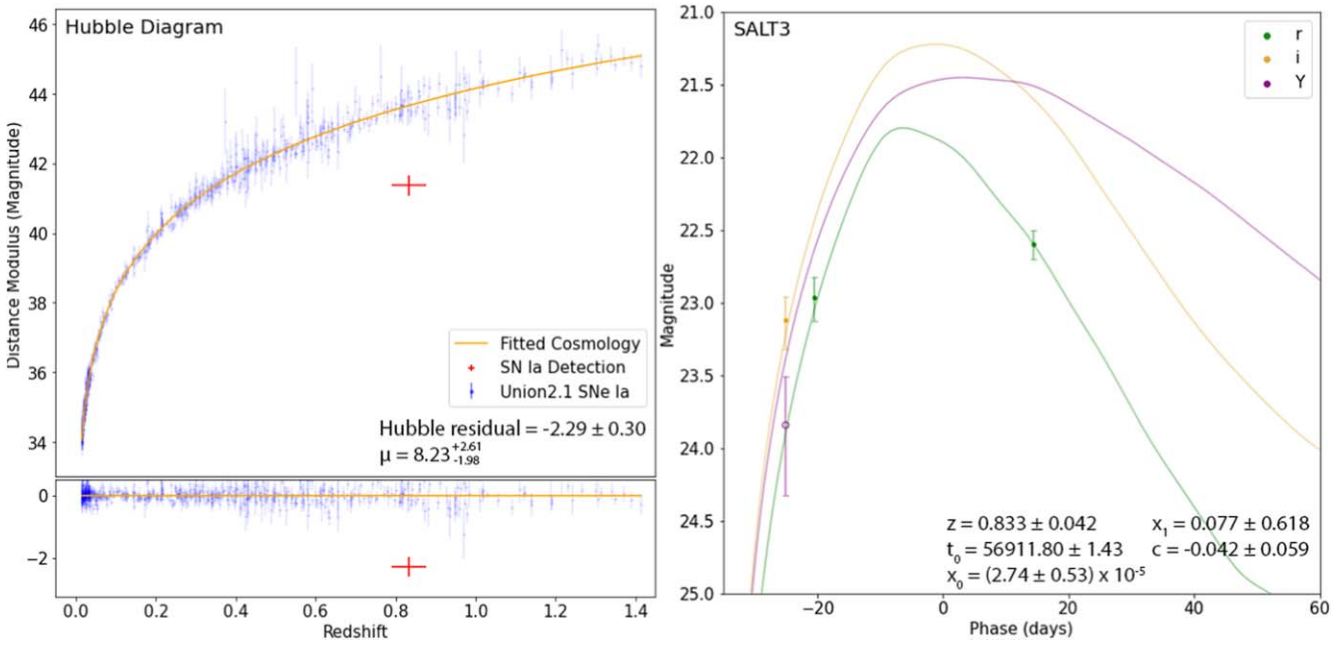

Figure 12. Best-fit SALT3 model for DESI-344.6252-48.8977 with a source photoz redshift prior of 1.188 ± 0.255.

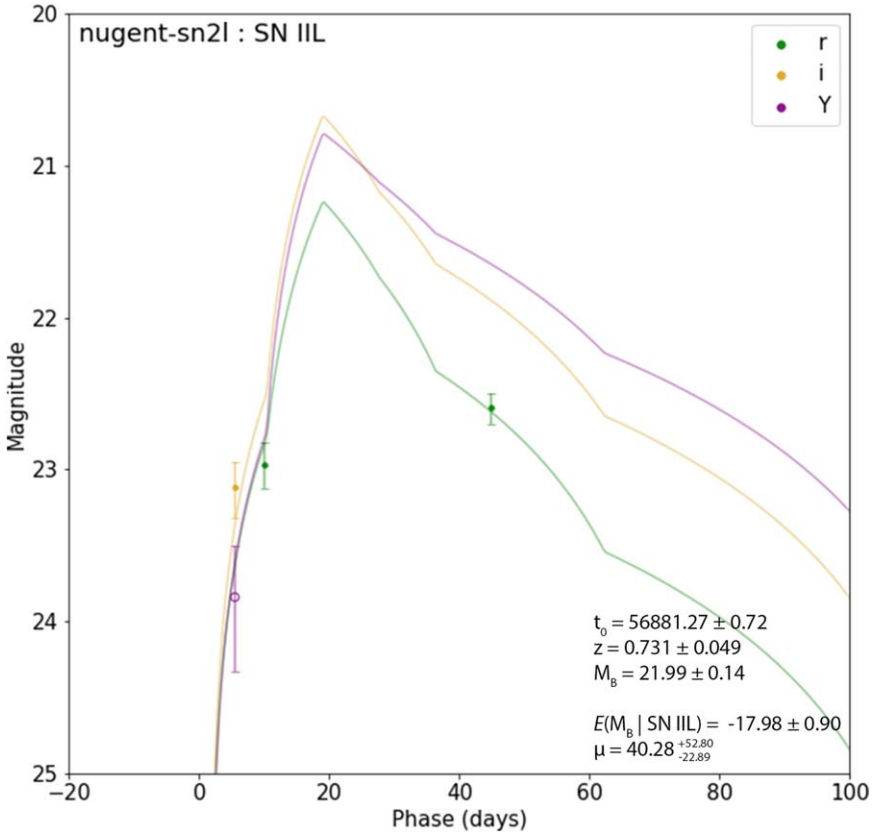

Figure 13. Best-fit core-collapse template model for DESI-344.6252-48.8977 with a lensed source photoz redshift prior 1.188 ± 0.255.

model (Fitzpatrick 1999). The modeled SALT2 parameters include redshift z, t_0, the normalization factor x_0 (normalized so that the peak B band apparent magnitude is 10.5 when $x_0 = 1$, per SNCosmo), the stretch factor x_1, and the color parameter c. We plot our photometry together with previously observed photometry and the SALT2 models. All coadded RGB images are made with the Legacy Surveys' RGB image generation scheme.[14] We present the results for four SNe Ia systems at different redshifts ($z = [0.18, 0.40, 0.53, 0.69]$) in Figures 5, 6, 7, and 8. The results for the full 32 DES SNe Ia test systems are

[14] https://github.com/legacysurvey/imagine/blob/main/map/views.py

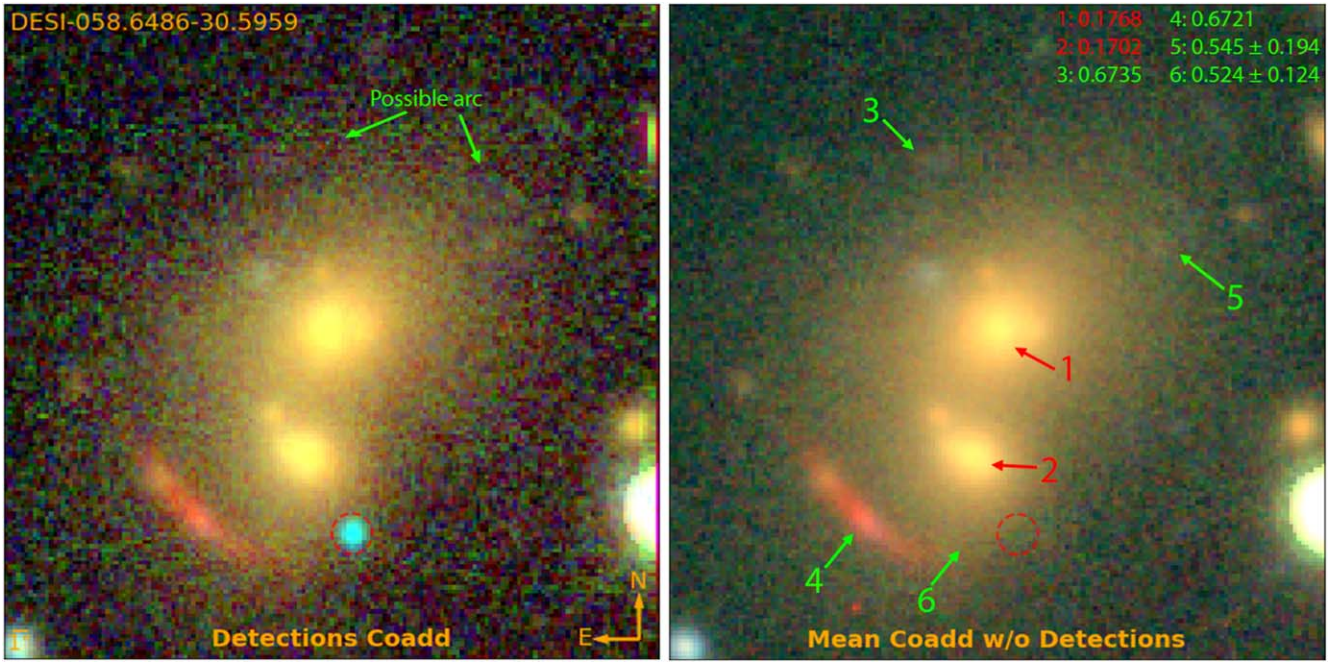

Figure 14. Coadded RGB images (using *g*, *r*, *i*, and *z* bands) of DESI-058.6486-30.5959 with and without the transient detection (red-dotted circle) exposures. The labeled objects are color coded as in the following postulated scenario: the lenses are red and the source galaxy is green. Photometric (shown with uncertainties) and spectroscopic (shown without uncertainties; A. Cikota et al. 2023, in preparation) redshifts for the labeled objects are displayed on the top right-hand corner. The posited lens galaxy has a spectroscopic redshift of 0.1702, and the posited lensed images have spectroscopic redshifts of 0.6735 and 0.6721.

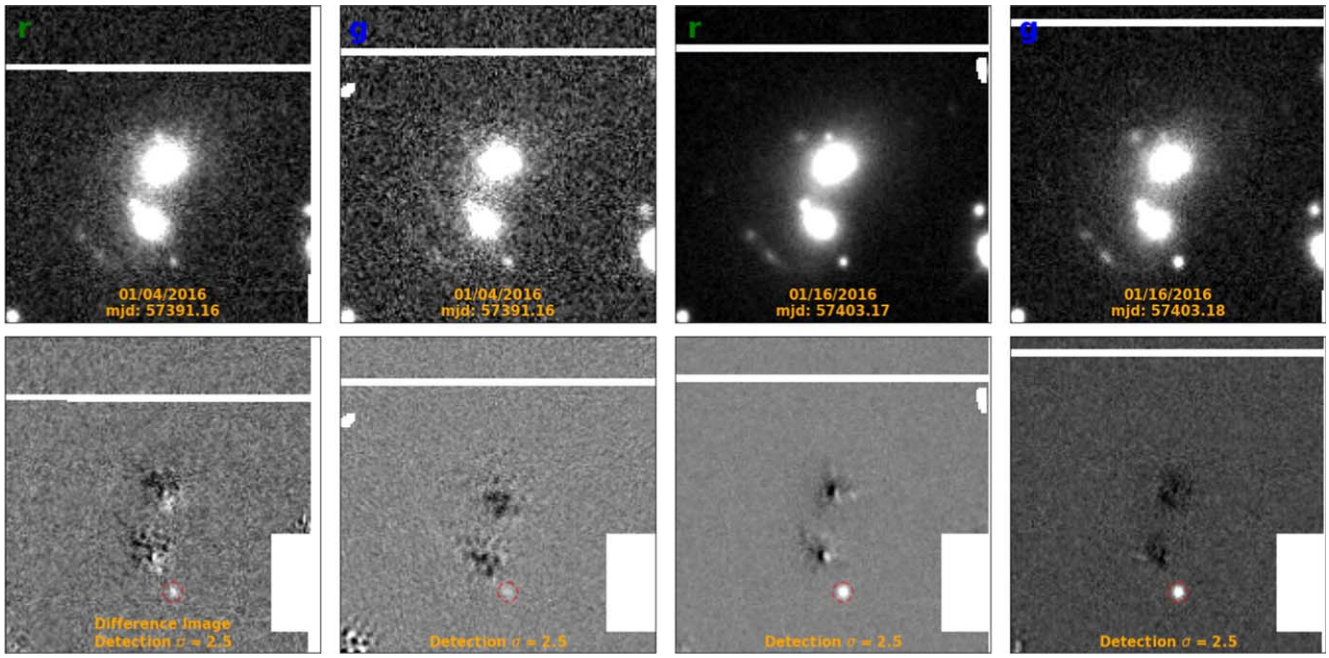

Figure 15. Detection exposures for the transient in DESI-058.6486-30.5959 in chronological order. See the caption of Figure 10 for the full description.

shown in Appendix A. All of the light curves that are presented are in the observer frame.

From these results, we found that our detection pipeline can detect known SN events within the DR9/DR10 data, with a 100% detection rate for the 32 test SNe Ia from DES. Furthermore, the new photometry points from our pipeline are consistent with the DES photometry for these SNe Ia.

6. Results and Discussion

We have identified seven lensed SN candidates, one unlensed SN, and two asteroids detections with our pipeline. This section will focus on one Grade A and two Grade B lensed SN candidates. The lower grade lensed SN candidates and the unlensed SN are given in Appendix B, and the

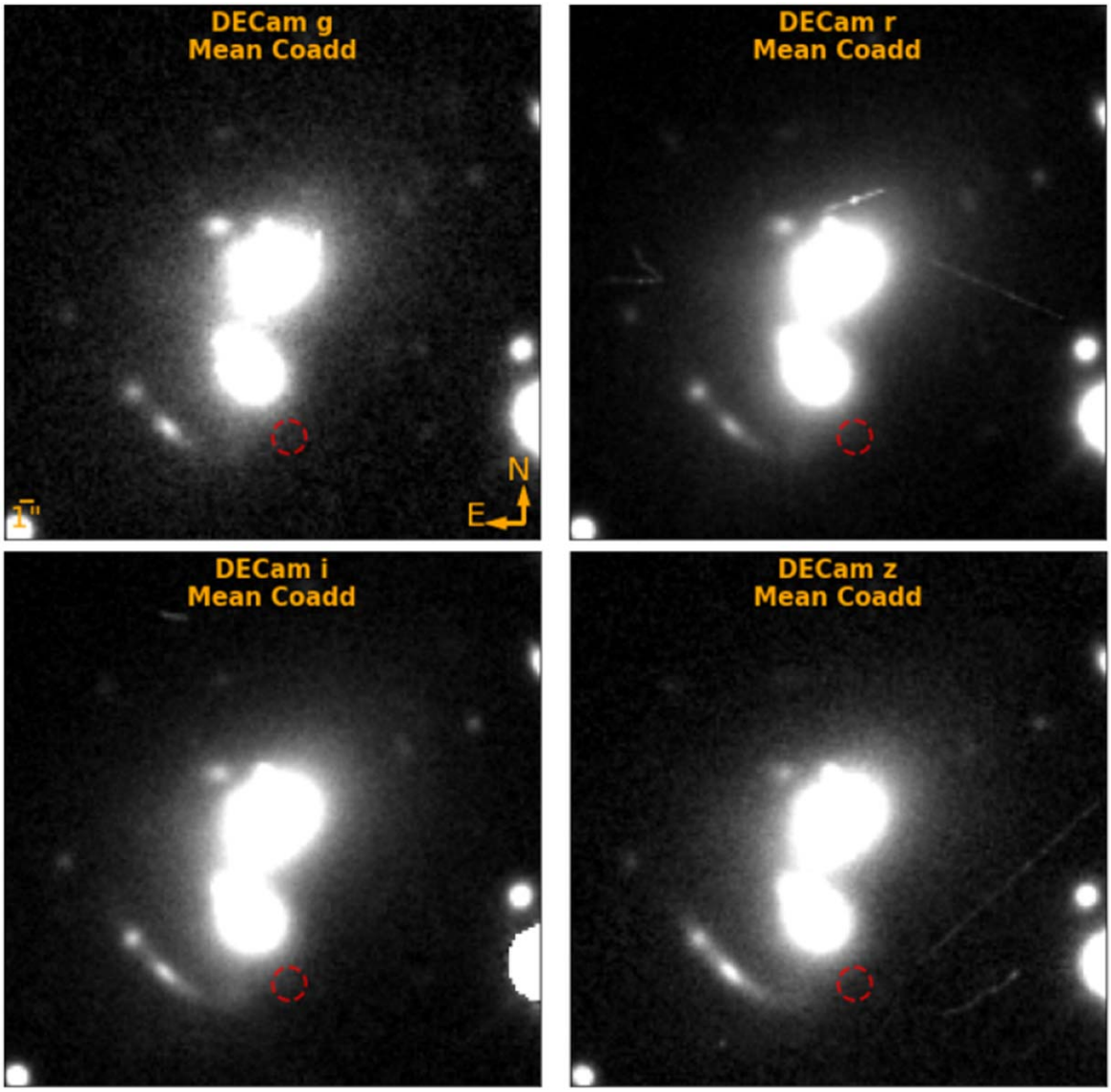

Figure 16. Mean coadded images of DESI-058.6486-30.5959 across different observed bands. These deeper images (especially the *r* and *i* bands) seem to support the possibility of a faint lensed image between the detection (red-dotted circle) and the arc.

asteroid detections are given in Appendix C. We would also note that all eight SN detections (summarized in Table 3) would have warranted additional follow-up observations if found live.

6.1. Grade A and B Lensed Supernova Candidates

The first seven systems (of eight) in Table 3 are identified by the pipeline and determined by visual inspection to be lensed SN candidates. For the eighth system, we believe that it is almost certainly not a strongly-lensed system, and have given it an overall grade of N/A. In this section, we will present the best three lensed SN candidates. The remaining four (and one unlensed SN) candidates are presented in Appendix B.

For each system, we attempt to narrow the identity of the transients by fitting different light-curve models to the photometry. We test for four different postulations for each system: unlensed SN Ia (uL-SN Ia), lensed SN Ia (L-SN Ia), unlensed CC SN (uL-CC SN), and unlensed CC SN (uL-CC SN). In this paper, we only present figures for the most probable scenarios (systems with "Y" in the "Shown" column 7 of Table 3).

We account for Milky Way extinction according to Schlafly & Finkbeiner (2011). When fitting a SN Ia light-curve model (for uL-SN Ia and L-SN Ia), we use the SALT3 model (Kenworthy et al. 2021) and fit for the parameters: redshift z, time of B band peak t_0, the normalization factor x_0, the stretch factor x_1, and the color parameter c. We do not fit for host-galaxy dust because the c parameter would be largely degenerate with small amounts of reddening. We use the following priors in the fitting process: $c \sim \mathcal{N}(0, 0.1)$ and $x_1 \sim \mathcal{N}(0, 1)$. We then use the best-fit SALT parameters for stretch and color corrections, and find the Hubble residual for the given model. This is plotted together with SNe Ia from Suzuki et al. (2012). Though this data is modeled with

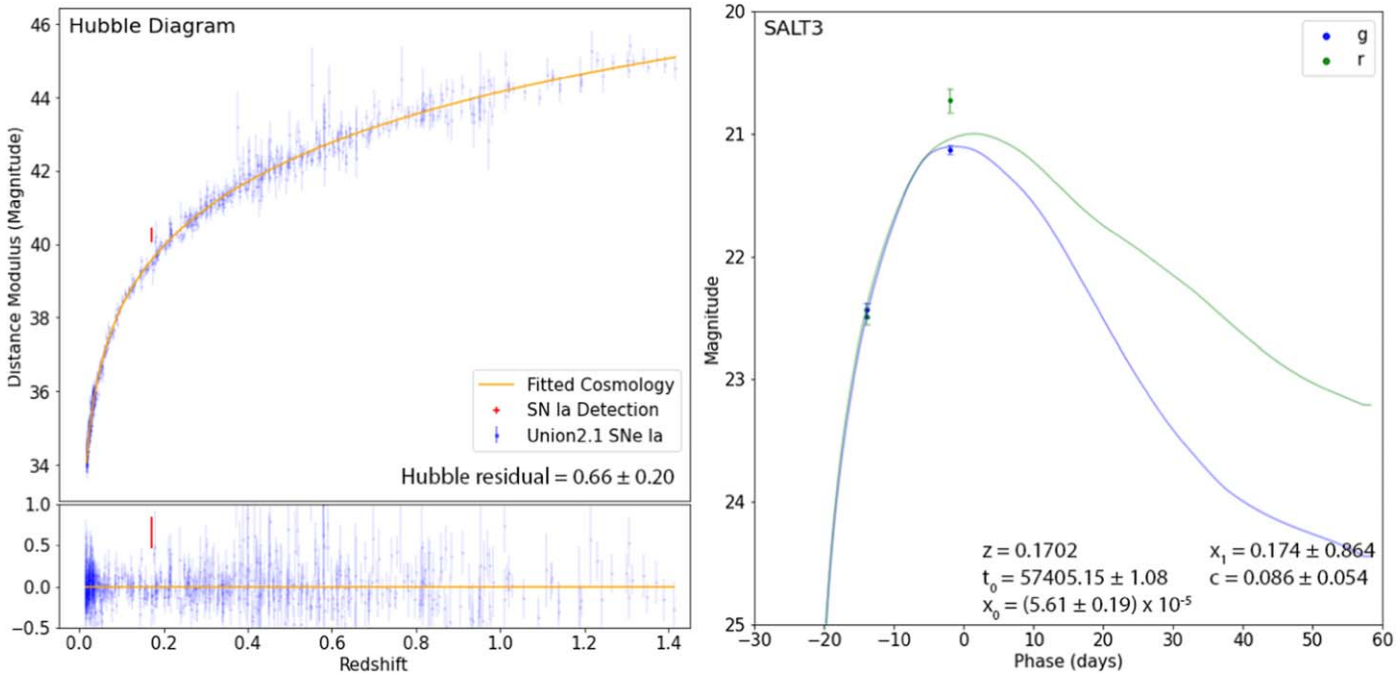

Figure 17. Best-fit SALT3 model for DESI-058.6486-30.5959 with a lens redshift of 0.1702. For this and Figure 18, solid photometry points correspond to the detection passes shown in Figure 14.

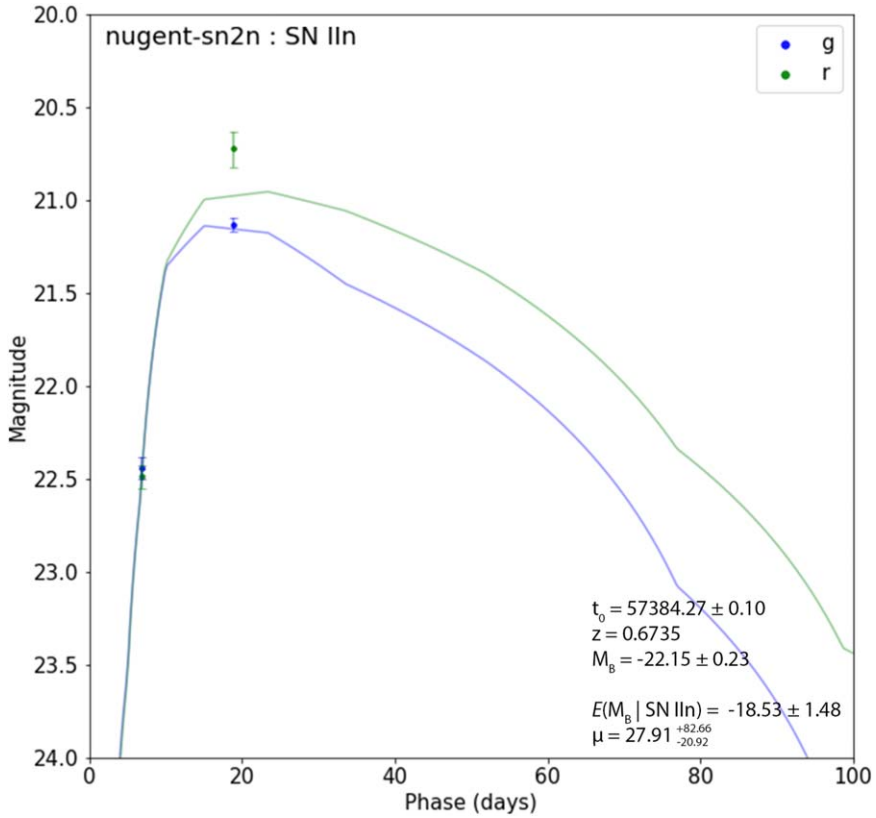

Figure 18. Best-fit core-collapse template model for DESI-058.6486-30.5959 with a source photoz redshift of 0.6735.

SALT2, we expect negligible differences in Hubble residuals of 7 ± 11 mmag (Kenworthy et al. 2021). To model CC SNe light curves, we fit for 161 separate CC SNe templates (as provided by SNCosmo). All of the CC templates are parameterized by only t_0, z, and amplitude (a scaling term with arbitrary units), allowing for a small amount of host-galaxy dust. In all of the CC SN light curves shown in this paper, the best-fit $E(B-V)$ values are very small ($\lesssim$0.01),

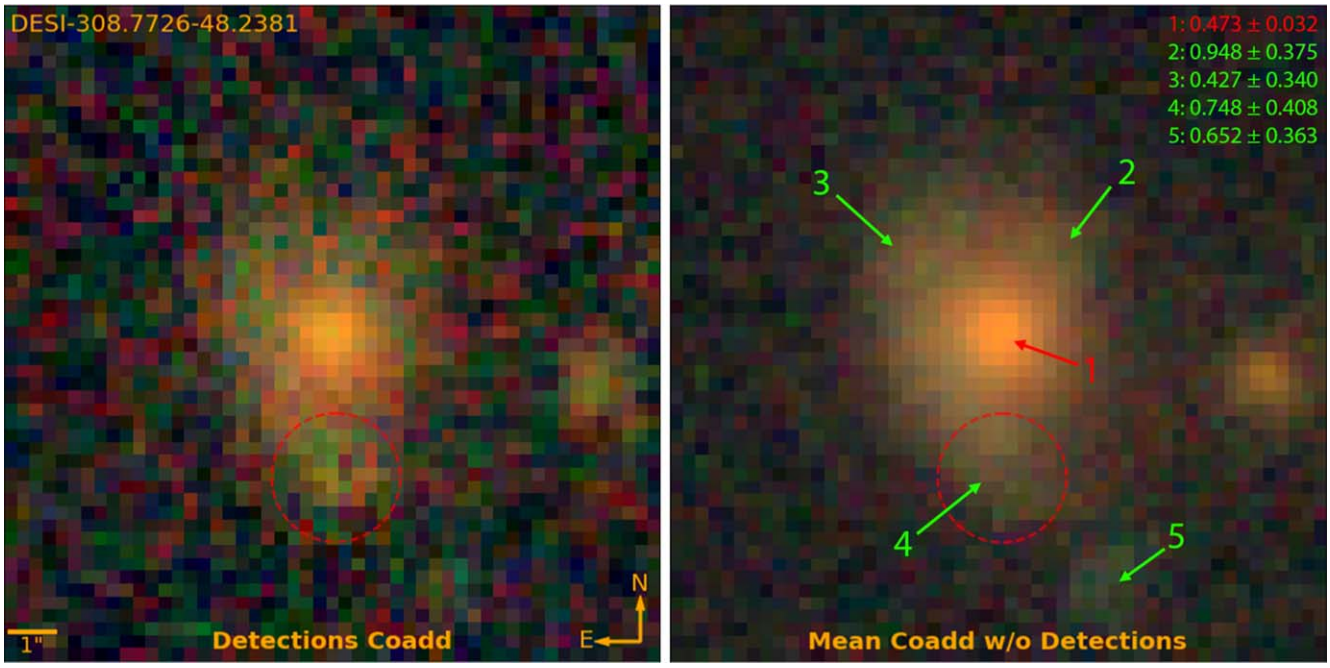

Figure 19. Coadded RGB images (using *g*, *r*, *i*, and *z* bands) of DESI-308.7726-48.2381 with and without the transient detection (red-dotted circle) exposures. The labeled objects are color coded as the following postulated scenario: the lens galaxy is red and the source galaxy is green. Photometric redshifts are displayed on the top right-hand corner. The posited lens galaxy has a photo*z* of 0.473 ± 0.032, and the posited lensed images have photo*z*es of 0.948 ± 0.375, 0.427 ± 0.340, 0.748 ± 0.408, and 0.652 ± 0.363.

and therefore we do not report the reddening parameters. Except for one system, redshift priors used for both CC SNe and SNe Ia postulations (see column 8 of Table 3) are photometric redshifts of objects identified by the forward modeling source extraction algorithm, the Tractor (Lang et al. 2016). All of the photometric redshifts in this paper are from Zhou et al. (2020). For DESI-058.6486-30.5959, we fix the redshifts to be the spectroscopic redshifts (A. Cikota et al. 2023, in preparation).

In the figures that follow, if a lensed scenario is postulated, then we estimate the amplification, μ. If a CC SN scenario is postulated, then the expected peak *B* band magnitude for a given SN type (X) is represented with $E(\mathrm{M_B} \mid \mathrm{X})$, where the values from Table 1 are used.

6.1.1. DESI-344.6252-48.8977

DESI-344.6252-48.8977 is a strong lensing candidate that was discovered in Storfer et al. (2022) and assigned a C-grade. In our analysis, we find that this relatively-low grade was given because in the Legacy Surveys coadded image, the arc and counterarc (objects 2 and 3 respectively, in Figure 9) appear to have somewhat different colors due to the transient. However, with an improved analysis of the color of the arc and counterarc by the criteria laid out in Huang et al. (2021), taking into account of the presence of the transient and photo*z* (see below), we now regrade this system as an A-grade lensing candidate.

The lensed arc in DESI-344.6252-48.8977 is located southwest of the lens, with its counterimage appearing northeast of the lens. The color and photo*z*es of the two lensed images agree with each other (within uncertainties), with both photo*z*es ($z = 1.403 \pm 0.269$ and 1.188 ± 0.255) being significantly higher than the lens photo*z* ($z = 0.374 \pm 0.053$). We note that for object 3, because the majority of the exposures do not contain the transient, its light is unlikely to significantly affect the photo*z* of object 3. Since the lens and source galaxies appear to be red elliptical galaxies, we consider their photo*z*es to be reliable. The image-counterimage arrangement indicates a strong lensing configuration. The detected transient lies directly on the counterimage. As with all of the other light curves presented, the light curves below are constrained by both detection and non-detection exposures. See Figure 10 for single exposure detection images and their corresponding differencing images.

Postulation 1: uL-SN Ia—Figure 11 shows the best-fit light-curve model for the uL-SN Ia scenario. We see that it is not a good fit ($\chi^2/\mathrm{DOF} = 5.47$), especially in the *r* band. Additionally, the resulting SALT3 model has a statistically significant Hubble residual of 1.10 ± 0.24. Thus, we believe that this detection is unlikely to be an uL-SN Ia. The uL-CC SN scenario is not shown, which also (as with the uL-SN Ia scenario) has a large χ^2/DOF (see Table 3).

Postulation 2: L-SN Ia—Figure 12 shows the best-fit light-curve model for the L-SN Ia scenario. Due to the high redshift, SALT3 cannot model the *g* band observation and it is ignored in the fitting process. For the three redder bands, the best-fit SALT3 curve model agrees well with the photometric data. Based on the Hubble residual of -2.29 ± 0.30, the implied amplification is $8.23^{+2.61}_{-1.98}$. This is consistent with the expectation of a multiply-imaged SN by a galaxy-scale lens (e.g., Shu et al. 2018). Finally, the best-fit SN redshift, $z_{SN} = 0.833 \pm 0.042$, is consistent with the photo*z* of the source galaxy. We note that this redshift value is in line with our preliminary investigation of the feasibility of our search (see Figure 2).

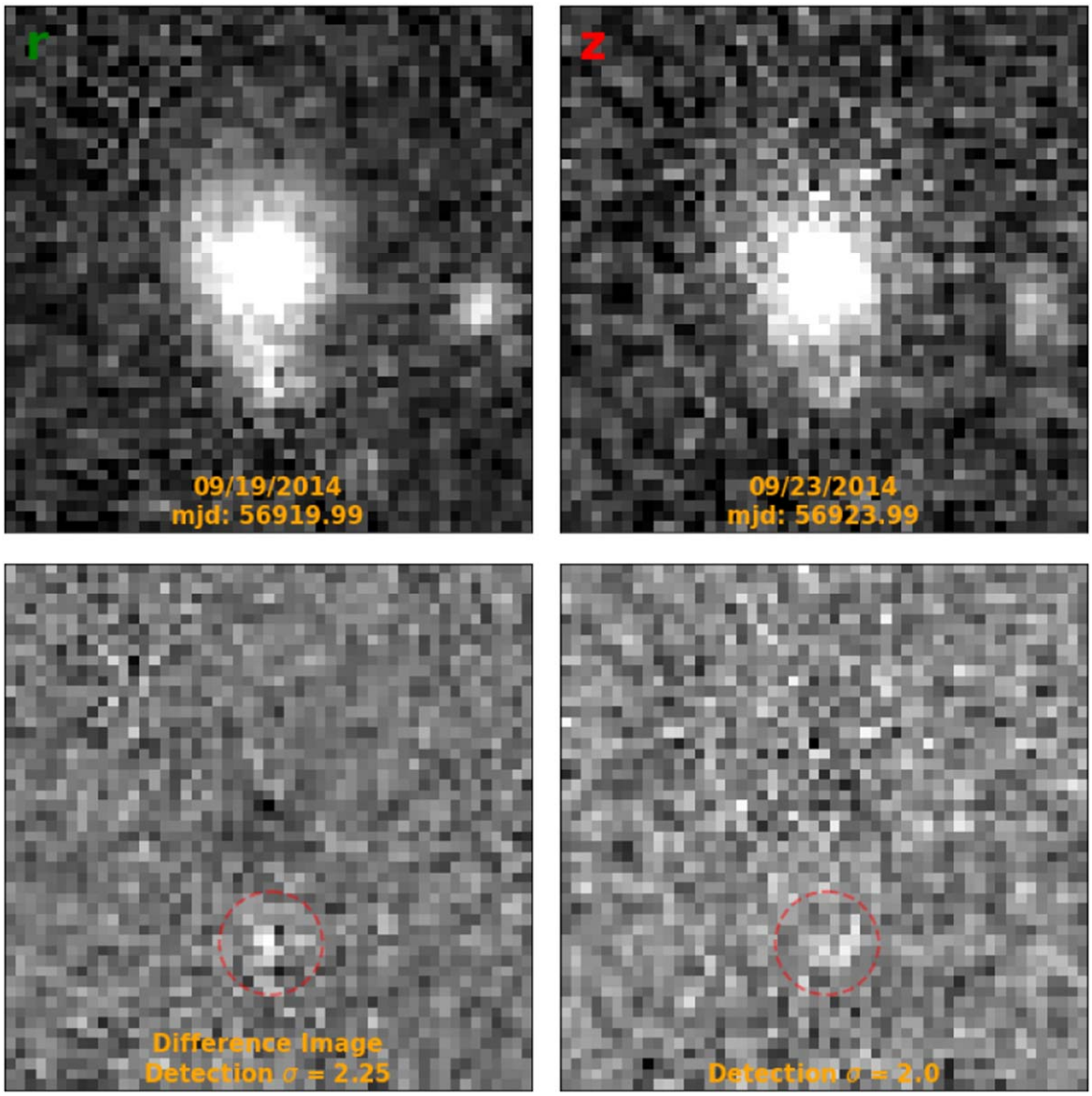

Figure 20. Detection exposures for the transient in DESI-308.7726-48.2381 in chronological order. See caption of Figure 10 for the full description.

Postulation 3: L-CC SN—Figure 13 shows the best-fit light-curve model for the L-CC SN scenario. As with the previous postulation, this model cannot fit the *g* band data point due to the high redshift, and thus is ignored in the fitting process. The best-fit model (the nugent-sn2l SN IIL template) is in good agreement with the photometric data from the redder bands. However, the implied magnification is quite large. Despite this, we note that: 1.) such a magnification is not impossible (e.g., Quimby et al. 2014), and 2.) because CC SNe have a large range of M_B, the uncertainties of the amplification are large. Therefore the L-CC SN scenario is still plausible for this system.

Conclusion—Any unlensed SN postulation seems unlikely, due to the poor agreement between the light-curve model and the data. Additionally, for the uL-SN Ia scenario, the Hubble residual would be too high. With all of the evidence considered, this is very likely a lensed SN. A L-SN CC is possible. However, we believe that it is most likely a L-SN Ia. This conclusion is based on the following:

1. The red color and morphology seem to indicate that the putative lensed source is an elliptical galaxy. The foreground galaxy is clearly an elliptical galaxy. Thus, the photo*z*es for the punitive lens and source are both likely reliable, with the later being significantly higher than the former. Based on this, combined with the classic image-counterimage configuration, we regard this system as a grade-A lens candidate.
2. The putative SN is situated directly on the counterimage.
3. Given that the source galaxy is likely an elliptical galaxy, the SN is more likely to be a Ia than CC.
4. The SN Ia light-curve model is a good fit to the photometry and the Hubble residual is most consistent with it being lensed. For this scenario, the amplification is also consistent with galaxy-scale strong lensing.

If it is indeed a lensed SN, then this would be the first galaxy-scale strongly-lensed SN to be resolved by ground-based observations. Furthermore, either for the case of L-CC SN or

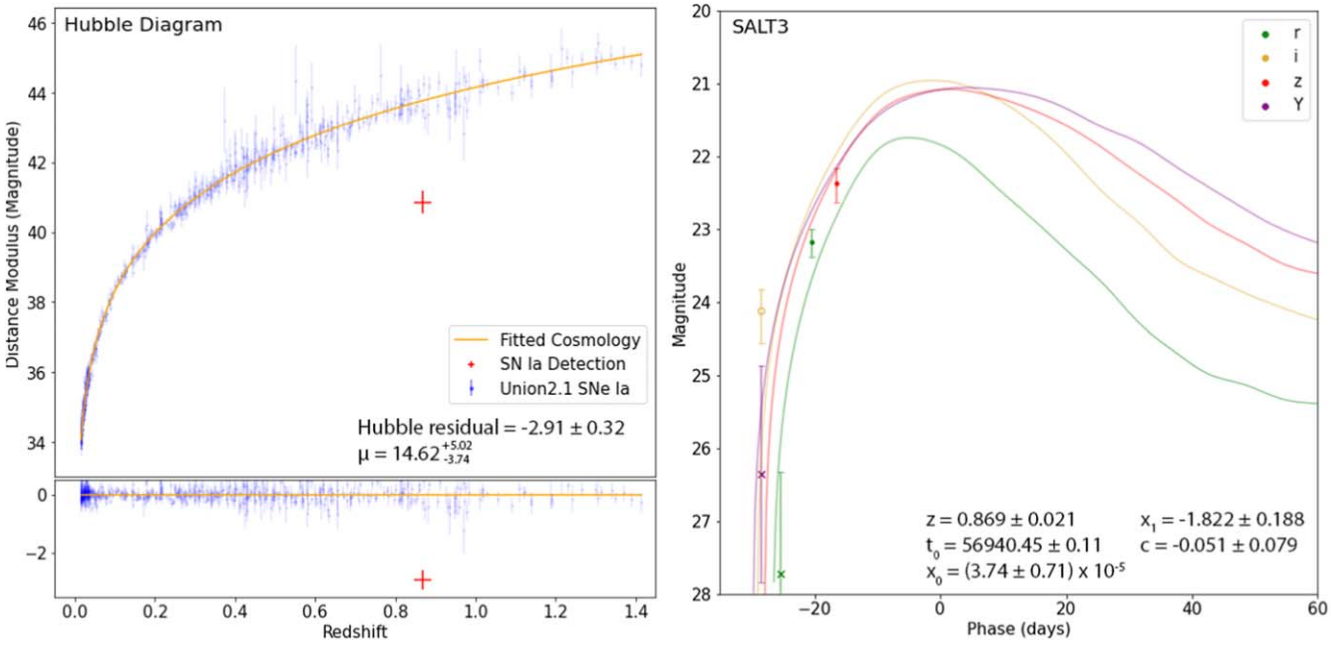

Figure 21. Best-fit SALT3 model for DESI-308.7726-48.2381 with no redshift prior. For this and Figures 22 and 23, solid photometry points correspond to the detection passes shown in Figure 20, hollow points correspond to other exposures with PSF photometry, and crosses correspond to measurements using aperture photometry (Section 3.4).

L-SN Ia, it is at a significantly higher redshift ($z_{SN} \gtrsim 0.8$) than the other two resolved galaxy-scale strongly-lensed SNe (Goobar et al. 2017, 2022). Given that the Einstein radius is $\sim 1\farcs5$, the expected time delay would be on the order of weeks. If caught live, it could have resulted in a H_0 measurement that would have been competitive with those from lensed quasars (e.g., Wong et al. 2019). Additionally, if it were a L-SN Ia, then the systematic effect of the mass sheet degeneracy could be significantly reduced due to the standardizability of its brightness (e.g., Birrer et al. 2022). Therefore, if discovered live, this system would make a strong case for high resolution imaging and spectroscopic follow-up observations.[15]

6.1.2. DESI-058.6486-30.5959

DESI-058.6486-30.5959 was discovered in Huang et al. (2021) as a grade-A strong lensing candidate.

DESI-058.6486-30.5959 is a galaxy-group lensing system, with a prominent red arc southeast of the lens. Including additional observations from DR10, there also appears to be a faint and highly magnified blue arc northwest of the lens, somewhat further from the estimated center of mass for the foreground galaxy group than the red arc. For this system, we have obtained VLT MUSE spectroscopy with preliminary redshifts (A. Cikota et al. 2023, in preparation) for objects 1, 2, 3, and 4 in Figure 14. See Figure 15 for single exposure detection images and their corresponding differencing images. The clearly detected transient lies $\sim 3''$ from the tip of the red arc (object 4, spectroscopically confirmed to be in the background) in the deep i band image (Figure 16, lower left-hand panel). The deep z band image (Figure 16, lower right-hand panel) seems to show that the arc curves toward the direction of the transient. There also seems to be a very faint galaxy (object 6) between the red arc and the transient location. The source extraction code for the Legacy Surveys, the Tractor, also identifies this object. It has similar photo$z$ (Zhou et al. 2020) as the aforementioned blue arc (object 3, also spectroscopically confirmed to be in the background), and therefore could possibly be its counterimage.

Postulation 1: uL-SN Ia—Figure 17 shows the best-fit light-curve model for the uL-SN Ia scenario. We see that the second r band photometry point is not well accounted for in this SALT3 model, but not at an unreasonable level. Additionally, the Hubble residual indicates that this scenario is unusually faint.

Postulation 2: L-CC SN—Figure 18 shows the best-fit light-curve model (with the best-fitting parameters of the best-fitting CC SN templates) for the L-CC SN scenario. The best CC SN template to the data is the nugent-sn2n SN IIn model. This model seems to provide the best overall fit. The implied amplification would be $27.91^{+82.66}_{-20.92}$. Depending on the location of the SN relative to the lensing critical curve, a large amplification for a group-scale lens is not impossible (e.g., SN Refsdal; Kelly et al. 2016 and Rodney et al. 2016). We also note the large uncertainty, which is typical for CC SNe.

Conclusion—The rise time for the transient in DESI-058.6486-30.5959 is consistent with it being a SN. If so, then there are three possibilities for the host galaxy—objects 2, 4, or 6. Object 2 is an elliptical galaxy (A. Cikota et al. 2023, in preparation). Thus, if it hosts a SN, then it is more likely a Ia than CC. Figure 17 shows that the SALT3 fit for a SN Ia at its spectroscopic redshift cannot account well for the r band photometry near maximum light. Furthermore, the Hubble residual of 0.66 ± 0.20, is unusually large at $>3\sigma$. Object 4 appears to be at the greatest angular separation from the transient. However, given the high degree of distortion due to lensing, without lens modeling, it is difficult to meaningfully assess how far away the SN is from object 4, e.g., in terms of half-light radius or directional light radius (Sako et al. 2018) if

[15] At the present, it is still possible to obtain the source galaxy spectra to measure its star formation rate. This in turn would more precisely quantify the SN Ia likelihood.

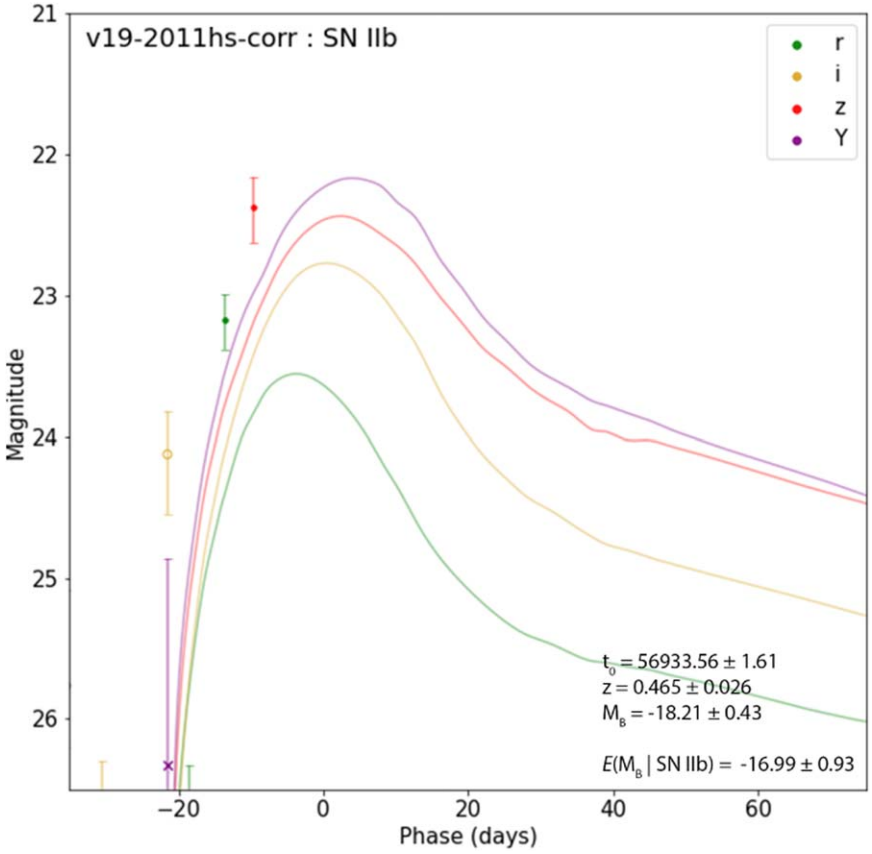

Figure 22. Best-fit core-collapse template model for DESI-308.7726-48.2381 with a lens photo$z$ redshift prior of 0.473 ± 0.032.

the delensed source is highly elliptical. Object 6 has the least angular separation from the transient. By color, location, and photo$z$, it appears to be the possible counterarc of the large arc (spectroscopically confirmed) to the northwest of the lens. The L-CC SN postulation is also consistent with object 6 appearing to be a blue, and therefore likely star-forming, galaxy. Given the sparsity of the photometric data, it is difficult to be certain. All factors considered, we assigned a grade of B to this transient as a lensed SN (more likely a CC than Ia). Additional spectroscopic observation of object 6 can test whether it is a lensed counterimage. We also note that if this transient was detected live, then real time photometric and spectroscopic follow-up observation could have been triggered to determine the nature of this transient.

6.1.3. DESI-308.7726-48.2381

DESI-308.7726-48.2381 was discovered in Storfer et al. (2022), and is given a D+ grade as a strong lensing candidate (see Section 2). If it turns out to be a lensing system, then the location of the detection would lie directly on the arc (Figure 19).

For DESI-308.7726-48.2381, there is a possible arc stretching from object 3 to 4 (in Figure 19), with object 2 as a counterimage. All three objects are identified by the Tractor. The transient candidate is only detected twice: in the r band, and four days later in the z band. This system serves as an example of how our pipeline is able to detect transients with only two detections because the event was captured in at least three sub-detections (see Section 3.3). See Figure 20 for single exposure detection images and their corresponding differencing images. These detections are visually comparable to the difference and detection images of known high-redshift SNe Ia in Section 5 (e.g., Figures 7 and 8). While there are only two detections, we are reasonably confident that this is an astrophysical transient because forced photometry in other bands at the detection location supports this postulation (Figure 21 to 23). Lastly, the photo$z$ measurements of the posited lens and source galaxies (0.473 ± 0.032 and 0.748 ± 0.408, respectively) are consistent with DESI-308.7726-48.2381 being an instance of strong lensing.

Postulation 1: L-SN Ia—Figure 21 shows the best-fit light-curve model for the L-SN Ia scenario with no prior on the redshift (given how broad the photometric redshifts of the punitive lensed images are). The SALT3 parameters are all reasonable with a best-fit redshift of 0.869. The resulting SALT3 model seems to fit the photometric data reasonably well, with an amplification of $14.62^{+5.02}_{-3.74}$.

Postulation 2: uL-CC SN—Figure 22 shows the best-fit light-curve model for the uL-CC SN scenario, which appears to be far worse when compared with Postulation 1. To reiterate, this is the best-fitting CC SN template model of 161 templates supplied by SNcosmo.

The uL-SN Ia fit is not shown, which results in a model that is too bright for what is expected of a SN Ia (see Table 3).

Postulation 3: L-CC SN—Figure 23 shows the best-fit light-curve model for the L-CC SN scenario. The best-fit redshift is at 0.828, and the required amplification is 15.61, albeit with a large uncertainty, which is typical for CC SNe. The data appear to rise more rapidly than the model, but this scenario may still be possible.

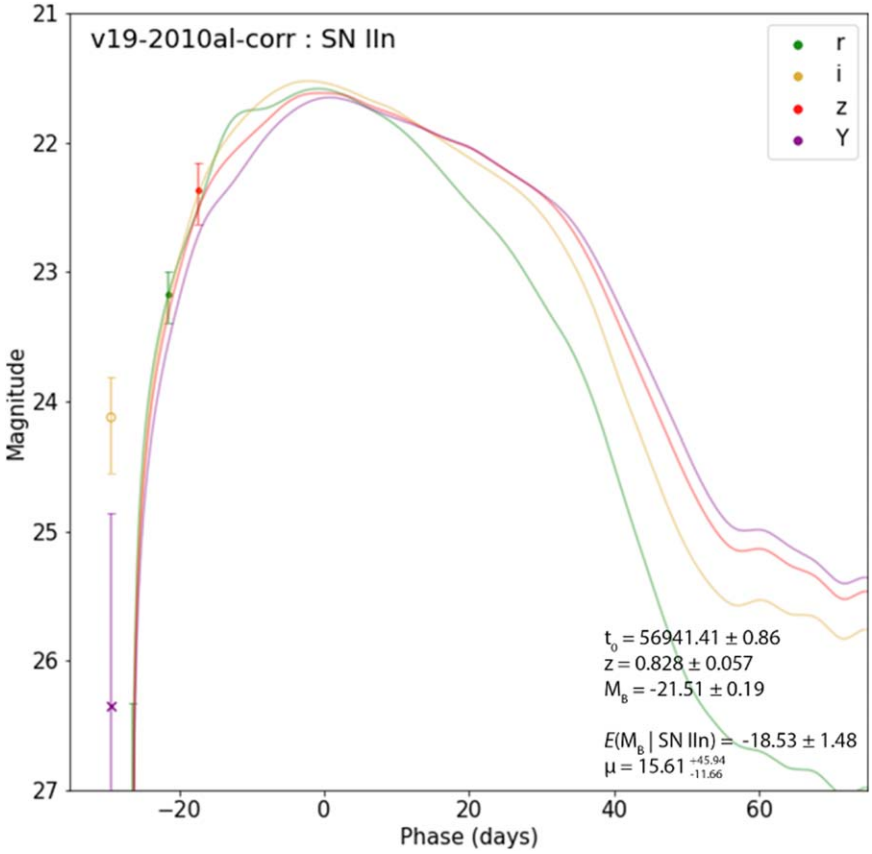

Figure 23. Best-fit core-collapse template model for DESI-308.7726-48.2381 with no redshift prior.

Conclusion—The transient found in DESI-308.7726-48.2381 is likely to be a lensed SN (more likely a Ia than CC). As with the previous two candidates, to be more confident of the lensing nature of this system, higher resolution and/or spectroscopic observations are needed.

7. Conclusion

We have developed a pipeline for a targeted search for lensed transients. For 5807 strong lensing systems and candidates observed by the DESI Legacy Imaging Surveys, this pipeline first generates a median coadd for each observed band as a reference image. It then employs two image subtraction algorithms to identify transient detections that are in close proximity, both spatially and temporally. By applying this pipeline to the DESI Legacy Imaging Surveys DR9/10, we have found seven lensed SN candidates, one unlensed SN, and two asteroids. We have also confirmed the variability of a large number of lensed quasars, which we will present in a subsequent paper (W. Sheu et al. 2023, in preparation). Of the seven lensed SN candidates, the one in DESI-344.6252-48.8977 is very likely to be a galaxy-scale strongly-lensed SN, probably a Type Ia. Follow-up high resolution imaging and spectroscopy, as well as lens modeling, can help us to reach a more definitive conclusion on whether some of these transient candidates are lensed.

Of our grade A and B candidates, the transients in DESI-344.6252-48.8977 and DESI-308.7726-48.2381 are likely to be L-SNe Ia, whereas the transient in DESI-058.6486-30.5959 is likely to be a L-CC SN. Preliminary results indicate that half of the 5807 systems, for which we have conducted the search, are actually strong lenses (S. Tabares-Tarquinio et al. 2023, in preparation). Since the uncertainties of our forecast results in Table 2 are Poisson in nature, we adjust our estimates by $1/2$ and their uncertainties by $\sqrt{1/2}$. And so, the number of L-SNe Ia and L-CC SNe with two or more detections becomes 3.29 ± 1.82 and 4.68 ± 2.18, respectively, and the corresponding numbers for three or more detections become 1.45 ± 1.19 and 2.27 ± 1.50. The results from our grade A and B candidates are broadly consistent with these forecasts.

We believe that these results demonstrate the very promising viability of our pipeline and its applicability to future surveys, such as the Vera C. Rubin Observatory Legacy Survey of Space and Time (LSST) and the Nancy Grace Roman Space Telescope (RST), to find live lensed SNe and other types of transients, as well as lensed quasars. Assuming the trend of three high grade lensed SN candidates for every $5807/2 \approx 3000$ systems found in our search, we have reached an approximate rate of 1 lensed SN per 1000 lensing systems in our targeted search. The Legacy Imaging Surveys DR9 spanned $\sim$5 yr, with an *r* band limiting magnitude of 23.43 and an average cadence of $\sim$90 days (note that it was not intended to look for transients). Given that LSST and RST will have significantly greater depth and higher cadence, we can expect this rate to be a lower bound for lensed SN discoveries in future targeted searches within these surveys. A targeted search strategy requires prior knowledge of the locations of lenses and lens candidates. However, we anticipate that this will impose little limitation for resolvable lensing systems because lens search pipelines are becoming increasingly efficient and fast (on the order of days). Thus, iterative lens searches can be rapidly carried out as the observational

coverage expands and depth increases (e.g., Huang et al. 2020, 2021; Storfer et al. 2022) for LSST and RST. Targeted searches for lensed transients can then quickly follow. Lensed transient discoveries in these future surveys will likely realize the potential to dramatically improve lens modeling and possibly resolve the H_0 tension.

Acknowledgments

This work was supported in part by the Director, Office of Science, Office of High Energy Physics of the US Department of Energy under contract No. DE-AC025CH11231. This research used resources of the National Energy Research Scientific Computing Center (NERSC), a U.S. Department of Energy Office of Science User Facility operated under the same contract as above and the Computational HEP program in The Department of Energy's Science Office of High Energy Physics provided resources through the Cosmology Data Repository project (Grant #KA2401022). X.H. acknowledges the University of San Francisco Faculty Development Fund.

This paper is based on observations at Cerro Tololo Inter-American Observatory, National Optical Astronomy Observatory (NOAO Prop. ID: 2014B-0404; co-PIs: D. J. Schlegel and A. Dey), which is operated by the Association of Universities for Research in Astronomy (AURA) under a cooperative agreement with the National Science Foundation.

This project used data obtained with the Dark Energy Camera, which was constructed by the Dark Energy Survey collaboration. Funding for the DES Projects has been provided by the U.S. Department of Energy, the U.S. National Science Foundation, the Ministry of Science and Education of Spain, the Science and Technology Facilities Council of the United Kingdom, the Higher Education Funding Council for England, the National Center for Supercomputing Applications at the University of Illinois at Urbana-Champaign, the Kavli Institute of Cosmological Physics at the University of Chicago, the Center for Cosmology and Astro-Particle Physics at the Ohio State University, the Mitchell Institute for Fundamental Physics and Astronomy at Texas A&M University, Financiadora de Estudos e Projetos, Fundação Carlos Chagas Filho de Amparo à Pesquisa do Estado do Rio de Janeiro, Conselho Nacional de Desenvolvimento Científico e Tecnológico and the Ministério da Ciência, Tecnologia e Inovacão, the Deutsche Forschungsgemeinschaft, and the Collaborating Institutions in the Dark Energy Survey. The Collaborating Institutions are Argonne National Laboratory, the University of California at Santa Cruz, the University of Cambridge, Centro de Investigaciones Enérgeticas, Medioambientales y Tecnológicas-Madrid, the University of Chicago, University College London, the DES-Brazil Consortium, the University of Edinburgh, the Eidgenössische Technische Hochschule (ETH) Zürich, Fermi National Accelerator Laboratory, the University of Illinois at Urbana-Champaign, the Institut de Ciències de l'Espai (IEEC/CSIC), the Institut de Física d'Altes Energies, Lawrence Berkeley National Laboratory, the Ludwig-Maximilians Universität München and the associated Excellence Cluster Universe, the University of Michigan, the National Optical Astronomy Observatory, the University of Nottingham, the Ohio State University, the OzDES Membership Consortium the University of Pennsylvania, the University of Portsmouth, SLAC National Accelerator Laboratory, Stanford University, the University of Sussex, and Texas A&M University.

The work of Aleksandar Cikota is supported by NOIRLab, which is managed by the Association of Universities for Research in Astronomy (AURA) under a cooperative agreement with the National Science Foundation.

We thank Alex Kim at the Lawrence Berkeley National Laboratory for insightful discussions on difference image photometry, as well as Saul Perlmutter and Greg Aldering for general commentary on our paper's results.

Software: Astropy (Astropy Collaboration et al. 2013, 2018), Montage (Jacob et al. 2010), SEP (Bertin & Arnouts 1996; Barbary 2018), SNCosmo (Barbary 2014), NumPy (Harris et al. 2020), Matplotlib (Hunter 2007).

Appendix A
Photometry of Previously Discovered SNe Ia

See Figures 24, 25, and 26 for our photometry, plotted against DES photometry and their best-fit SALT2 light-curve.

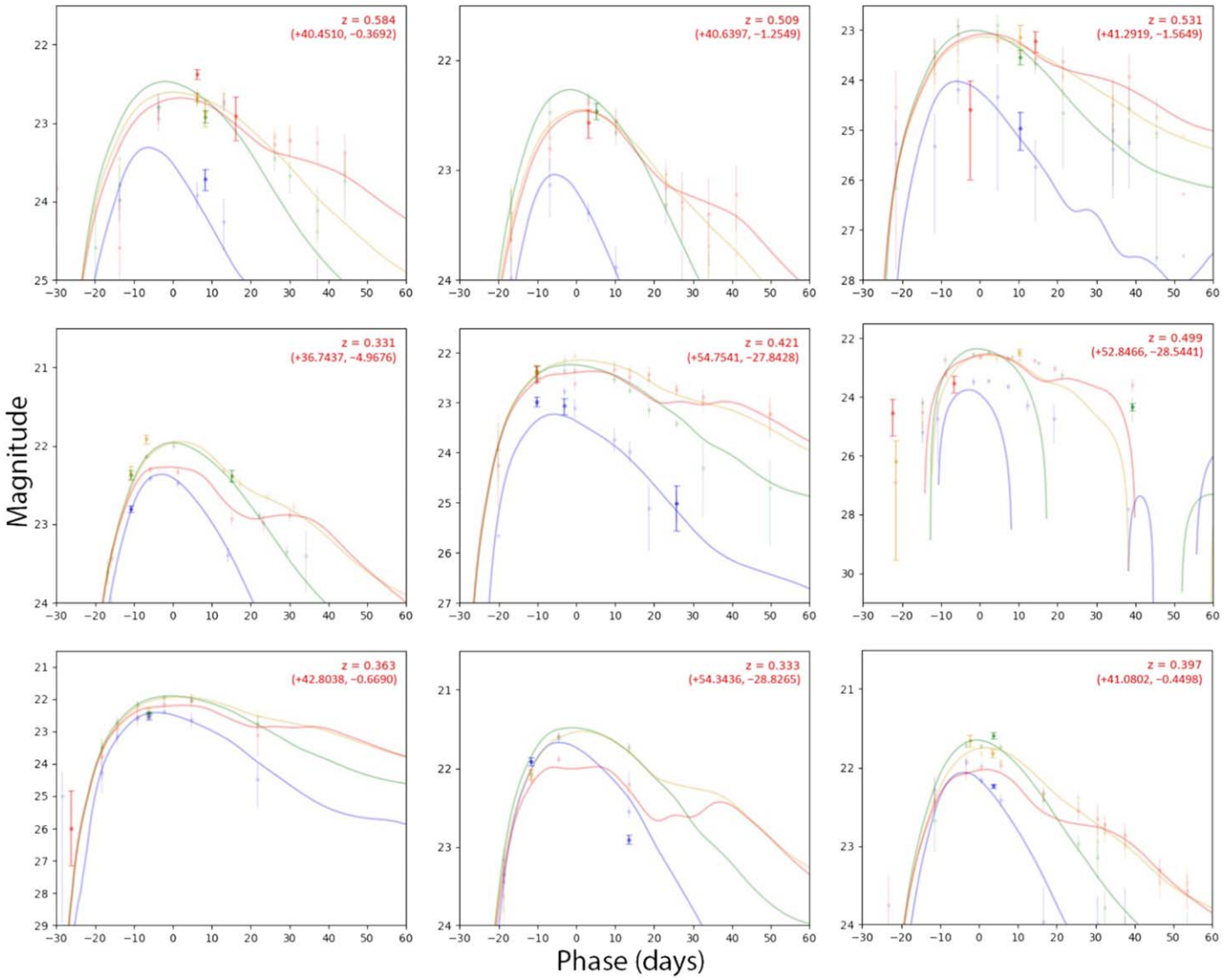

Figure 24. Our photometry (solid data points) for new detections of 9 (of 32; for the rest see Figures 25 and 26) known SNe Ia from DES, shown along with DES photometry (faint points) and their best-fit SALT2 light curve[16]. For all panels, we follow the color scheme of blue = g band, green = r band, yellow = i band, and red = z band. The redshift and the (R.A., decl.) is given on the top right-hand corner of every plot. Note that our measurements match well with DES photometry and provide additional photometry points for these SNe Ia.

[16] https://github.com/legacysurvey/imagine/blob/main/map/views.py

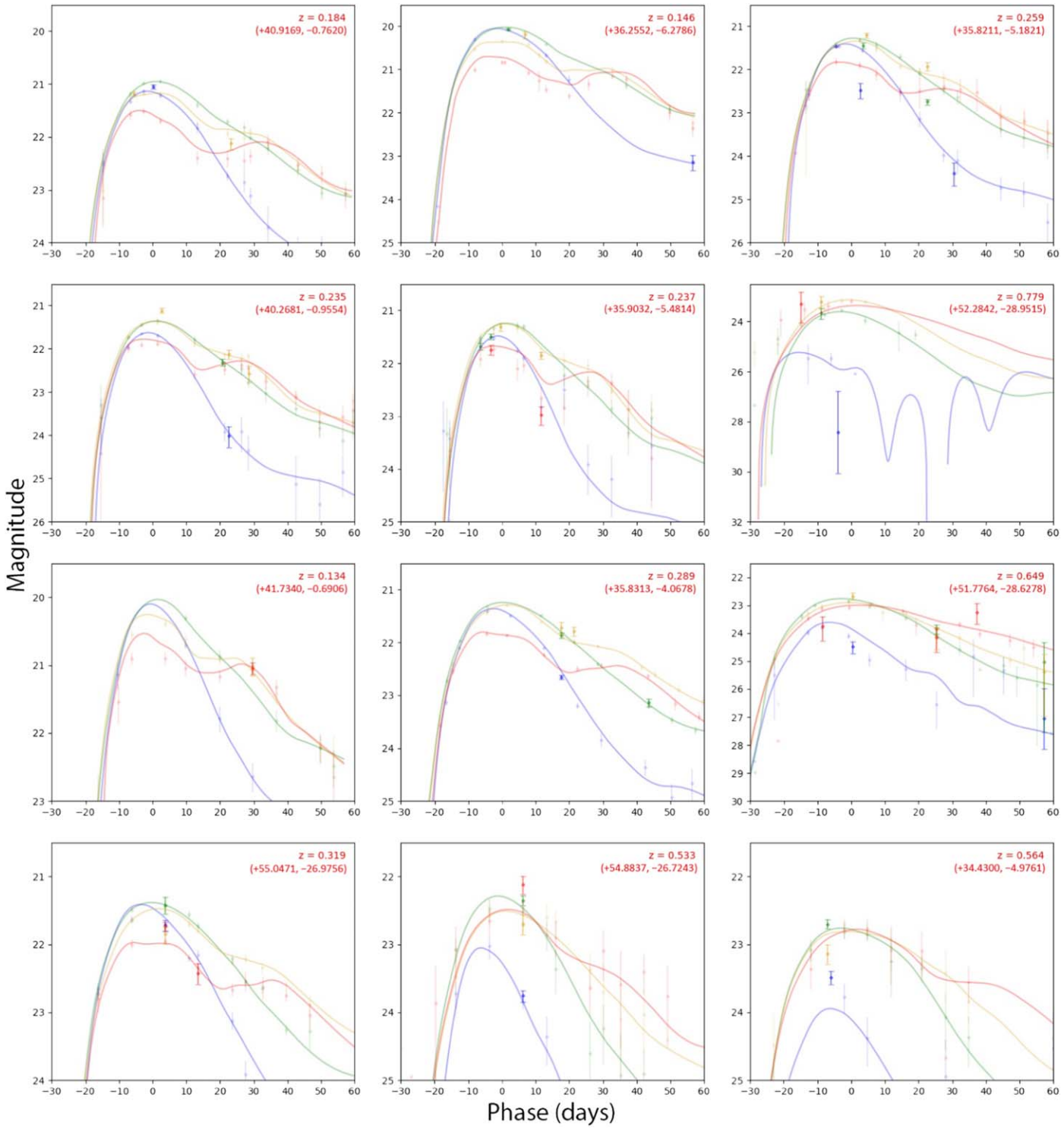

Figure 25. Our photometry (solid data points) for new detections of 12 (of 32) known SNe Ia from DES. For additional details, see the caption of Figure 24.

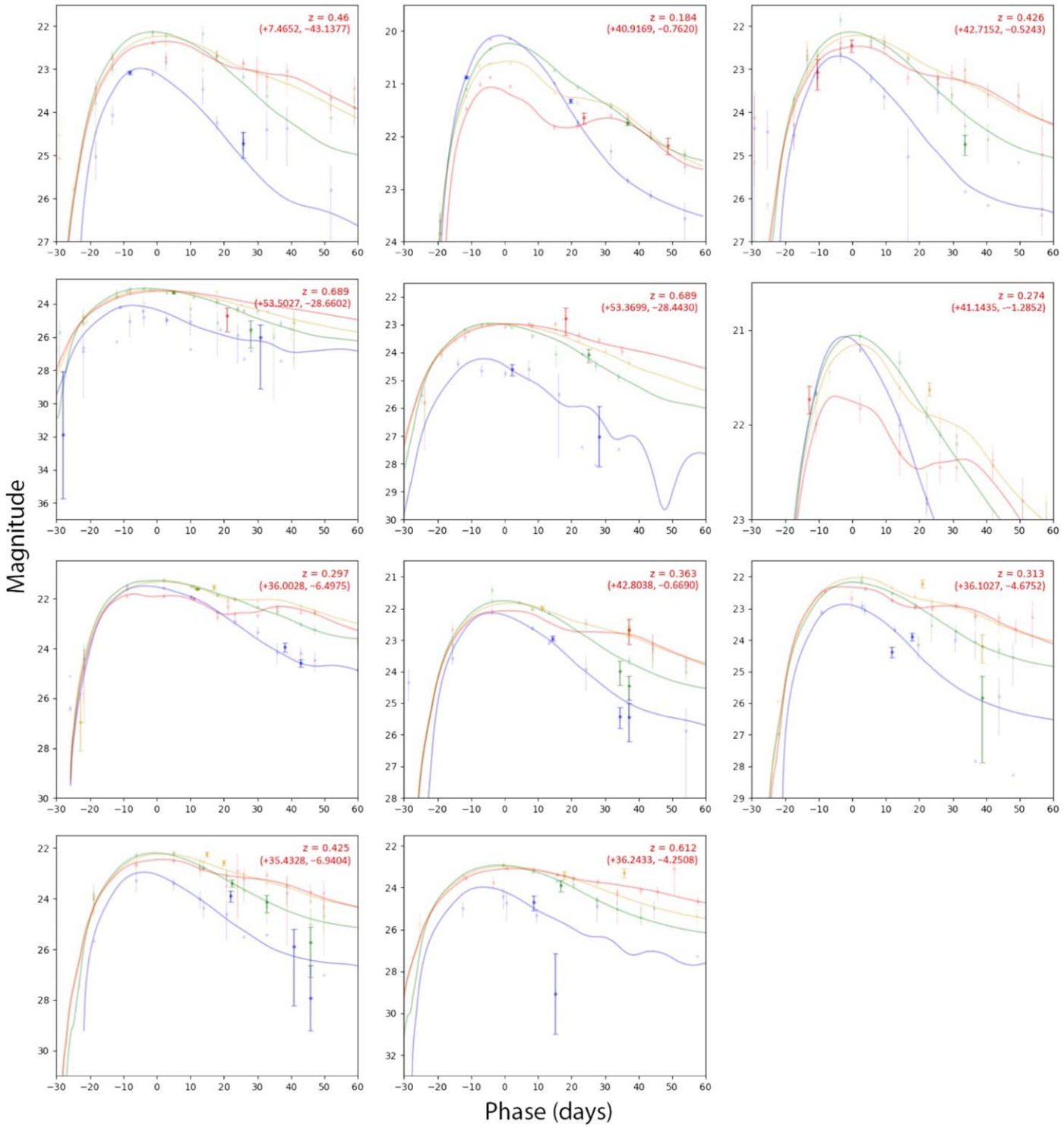

Figure 26. Our photometry (solid data points) for new detections of 11 (of 32) known SNe Ia from DES. For additional details, see the caption of Figure 24.

Appendix B
Grade C and D Lensed Supernova and Unlensed Supernova Candidates

B.1. DESI-034.3625-35.3563

DESI-034.3625-35.3563 is a C-grade strong lensing candidate that was discovered in Storfer et al. (2022).

DESI-034.3625-35.3563 is a strong lensing candidate system with a single massive galaxy as the main lens. There appear to be two faint arcs, located north (identified by Tractor as objects 4 and 5 in Figure 27) and south (objects 2 and 3) of the foreground galaxy, at approximately four arcseconds away. Given the similarities in morphology, color, and photo$z$, they quite possibly correspond to the same background source. The transient lies directly at the east end of the first arc (object 5). This transient is also only about 2.5 effective radii (Figure 29) away from the lens, and so it is possible that the foreground galaxy is the host. See Figure 28 for single exposure detection

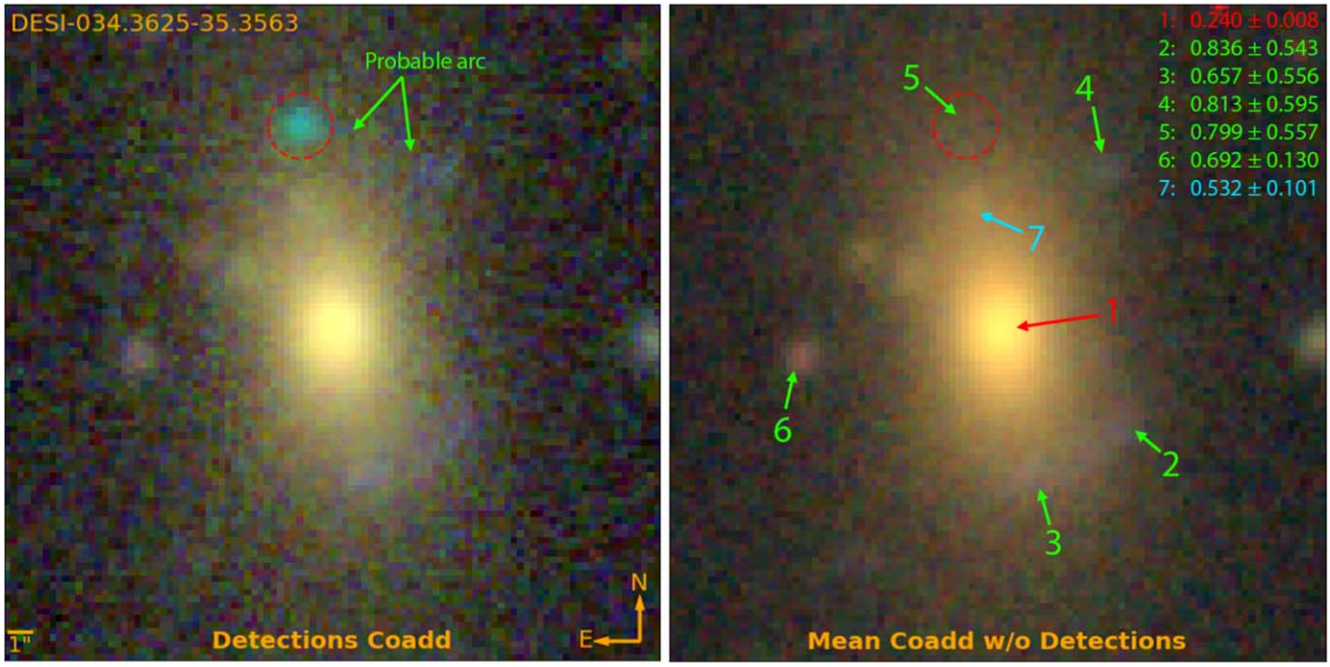

Figure 27. Coadded RGB images (using *g*, *r*, *i*, and *z* bands) of DESI-034.3625-35.3563 with and without the transient detection (red-dotted circle) exposures. The labeled objects are color coded as the following postulated scenario: the lens galaxy is red, the source galaxy is green, and the interloper or a second source is cyan. Photometric redshifts are displayed on the top right-hand corner. The posited lens galaxy has a photo*z* of 0.240 ± 0.008, and the posited lensed images have photo*z*es of 0.836 ± 0.543, 0.657 ± 0.556, 0.813 ± 0.595, 0.799 ± 0.557, and 0.692 ± 0.130.

images and their corresponding differencing images. In Figure 29, we subtract out the lens galaxy light to beter identify the lensed features.

Postulation 1: uL-SN Ia—Figure 30 shows the best-fit SALT3 light-curve model for the uL-SN Ia scenario. This model agrees well with the data, with reasonable light-curve parameters. The inferred absolute magnitude is consistent with the expectation for a SN Ia at the redshift of the foreground galaxy. Therefore, this seems to be a likely identity for the transient.

Postulation 2: L-CC SN—Figure 31 shows the best-fit light-curve model for the L-CC SN scenario. This SN IIP template fit has a slightly worse χ^2/DOF when compared to Postulation 1 (see Table 3), but this scenario is nevertheless possible. The model does require a fairly high amplification of $35.16^{+50.83}_{-20.79}$, albeit with large uncertainties.

Conclusion—The photometry seems to suggest that this detection is an uL-SN Ia. However, if additional high resolution and/or spectroscopic observation can confirm the faint lensed arc north of the lens, then the data would strongly support the postulation of a L-CC SN. This points to the importance of timely follow-up if this were a live detection because both the lensed and unlensed scenarios are possible given the location.

B.2. DESI-035.1374+00.4676

DESI-035.1374+00.4676 was discovered in Storfer et al. (2022) as a C-grade strong lensing candidate. However, after viewing the Hyper Suprime-Cam (HSC; Aihara et al. 2019) image (see Figure 32), we feel confident in moving this into the A-grade lens candidate category.

DESI-035.1374+00.4676 appears to be a galaxy group-scale strongly lensing system, with the arc lying northeast of the main lensing galaxy. This is supported by the photo*z*es of the posited lensed and source galaxies (0.296 ± 0.007 and 0.776 ± 0.118 respectively). The transient's location is somewhat far from both the lens and lensed image. See Figure 33 for single exposure detection images and their corresponding differencing images. From the best-fit foreground galaxy light parameters shown in Figure 34, the detection is approximately four half-light radii away from the lensing galaxy, which does not exclude it from being the host galaxy of the transient. Meanwhile, if it is hosted by the lensed source galaxy, then the distance between the transient and its center would be stretched along the tangential direction. Without lens modeling, which would provide the delensed source, it is difficult to estimate how far the transient is from the source galaxy center in meaningful terms (e.g., half-light radius or directional light radius). Therefore, neither is an impossible scenario based on the location. The possibility of a faint galaxy hosting the transient seems remote because such a galaxy does not even appear in the HSC image with superior seeing ($0\farcs58$ in the *i* band) and greater depth (26.2 *i* band limiting magnitude; see Figure 32).

Postulation 1: uL-SN Ia—Figure 35 shows the best-fit light-curve model for the uL-SN Ia scenario. The SALT3 model fits the four photometric data points well and its Hubble residual is consistent with the Union 2.1 best-fit cosmology. We consider this to be a possible identity of this transient.

Postulation 2: L-CC SN—Figure 36 shows the best-fit light-curve model for the L-CC SN scenario. This model also fits the available data well for a Type IIn SN template (nugent-sn2n), with an estimated amplification of $18.97^{+55.29}_{-14.13}$. Since this model is consistent with the data, we believe L-CC SN to be a possible identity of the transient.

Conclusion—This transient in DESI-035.1374+00.4676 appears to be consistent with an uL-SN Ia or a L-CC SN. With the data, it is difficult to discern which scenario is more likely.

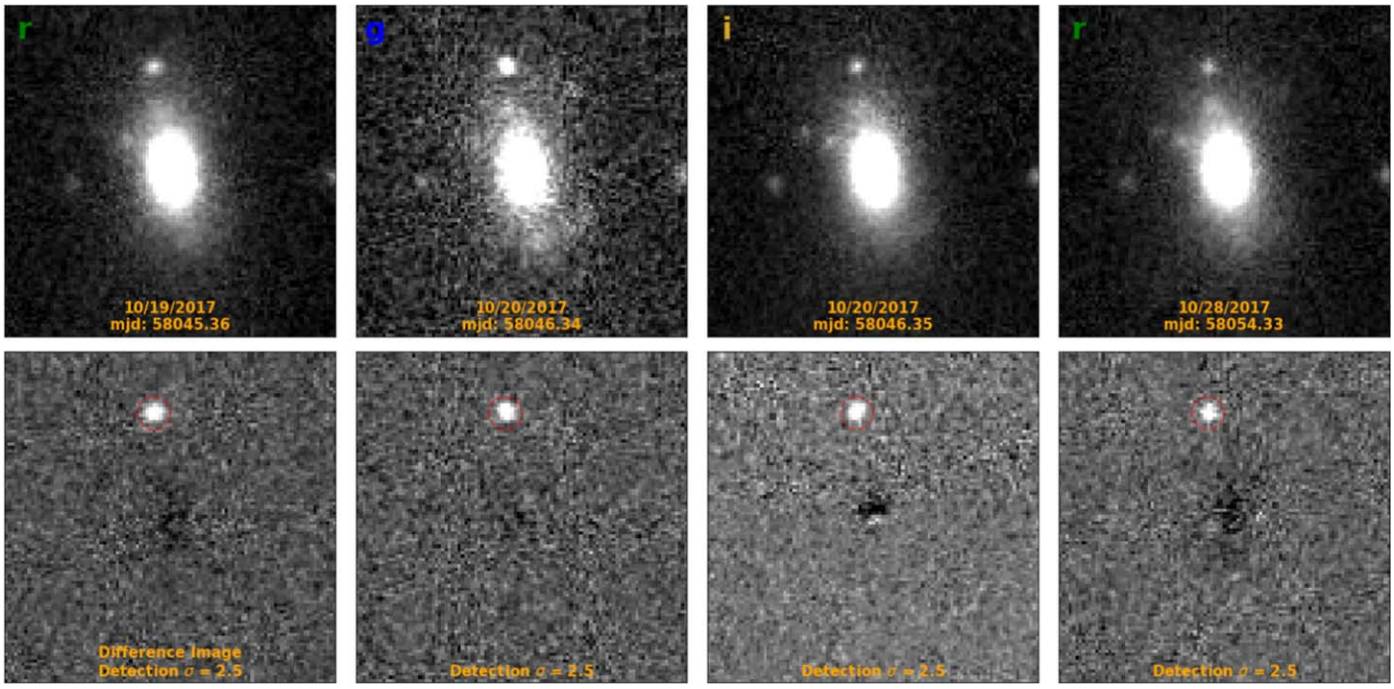

Figure 28. Detection exposures for the transient in DESI-034.3625-35.3563 in chronological order. See the caption of Figure 10 for the full description.

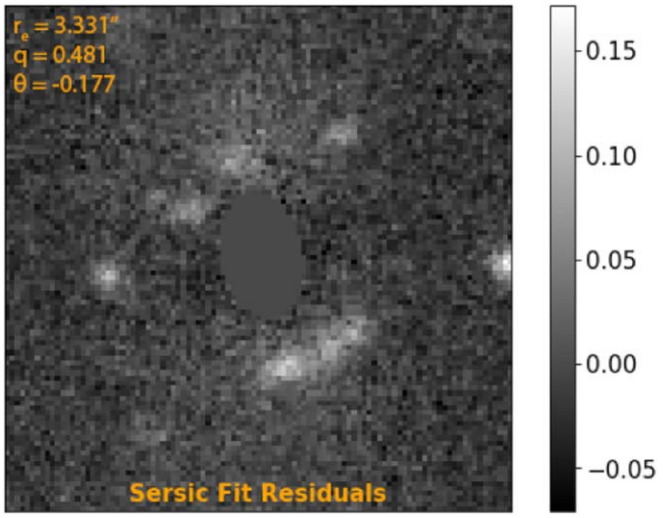

Figure 29. Residual image after lens light subtraction for DESI-034.3625-35.3563, with the Sérsic light parameters (half-light radius, axis ratio, and semimajor axis orientation from the *y*-axis) in the top left-hand corner (modeled in DECam *g* filter), with the core of the lens galaxy masked out.

In the case of a uL-SN Ia, the supernova would have occurred at approximately four effective radii away from the lensing galaxy. However, while the detection is far from the center of the lensed galaxy, this separation may not rule out the background as the host due to the tangential stretching from strong lensing. Lens modeling (using HSC DR2 data or follow-up higher resolution observations) may shed more light on this possibility. If it had been detected live, this detection would have warranted follow-up observations.

B.3. DESI-052.0083-37.2049

DESI-052.0083-37.2049 was discovered in Storfer et al. (2022) as a C-grade strong lensing candidate.

DESI-052.0083-37.2049 is a possible strong lensing candidate, although a ring galaxy or a face-on spiral scenario is not ruled out. The posited lens galaxy has a photo$z$ of 0.292 ± 0.029. The photo$z$es of the posited source images have large uncertainties (0.782 ± 0.610 and 0.272 ± 0.412; see Figure 37). The transient, however, is unmistakably present, with multiple detections lying directly on the arc-like structure. See Figure 38 for single exposure detection images and their corresponding differencing images.

Postulation 1: uL-SN Ia—Figure 39 shows the best-fit light-curve model for the uL-SN Ia scenario. Note that the first *r* band point is near the peak, almost coincidental with a *g* band point. The SALT3 light-curve model agrees reasonably well with the data. The Hubble residual is somewhat large, but does not rule out this scenario. Of note is that the first *z* band point appears to be too bright for this model.

Postulation 2: L-CC SN—Figure 40 shows the best-fit light-curve model for the L-CC SN scenario. The SN IIP template provides a reasonable fit for the photometry, with an amplification of $12.60^{+18.20}_{-7.45}$. Similarly to Postulation 1, the first *z* band point is not well fitted by this model; nor is the second point of the *r* band.

Conclusion—The transient in DESI-052.0083-37.2049 appears to be either an uL-SN Ia or a L-CC SN. If high resolution and/or spectroscopic observations reveal that the arc-like structure is part of a spiral or ring galaxy, then that would obviously rule out the L-CC SN scenario. Conversely, if it is a strongly-lensed arc or Einstein ring formation, then L-CC SN becomes quite possible considering the location of the detection. If found it had been live, then this detection would have warranted follow-up observations.

B.4. DESI-084.8493-59.3586

DESI-084.8493-59.3586 was discovered in Storfer et al. (2022) and was labeled as a C-grade strong lensing candidate.

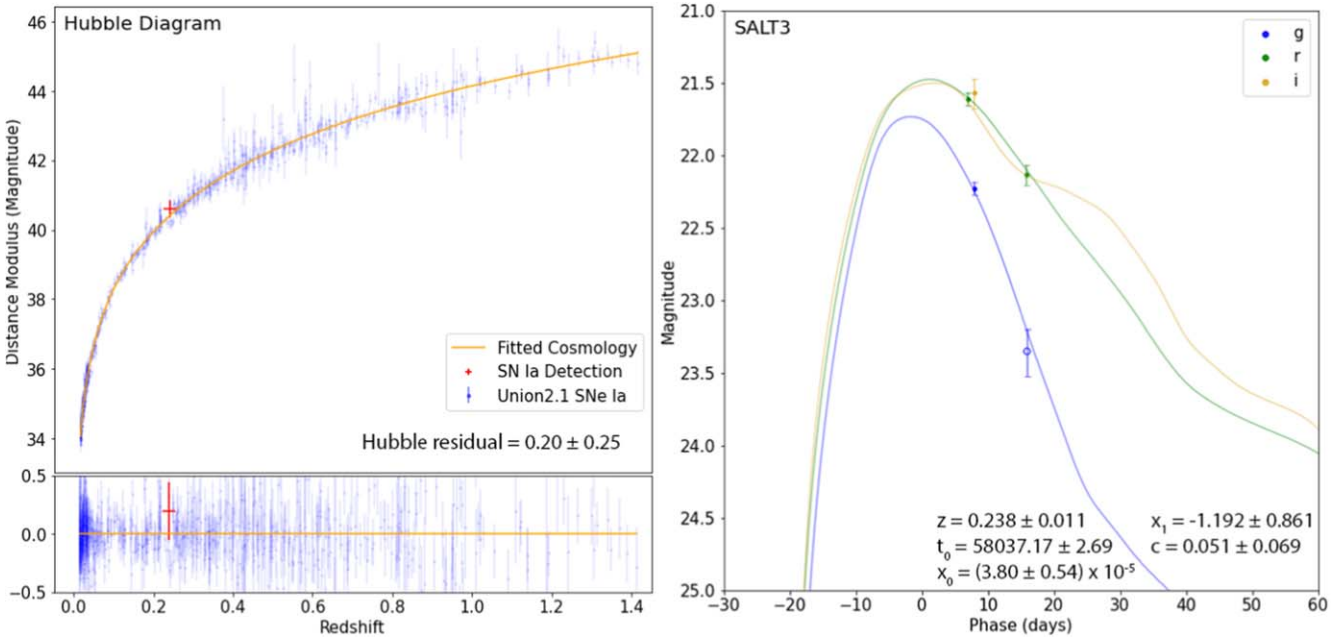

Figure 30. Best-fit SALT3 model for DESI-034.3625-35.3563 with a lens photo$z$ redshift prior of 0.240 ± 0.008. For this and Figure 31, solid photometry points correspond to the detection passes shown in Figure 28.

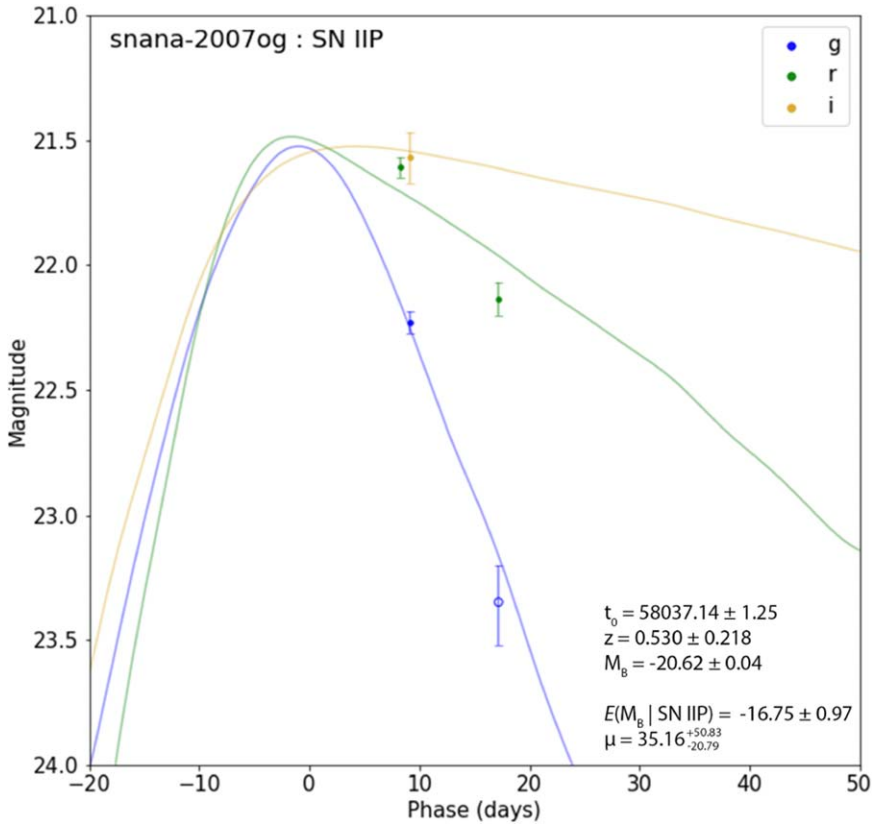

Figure 31. Best-fit core-collapse template model for DESI-034.3625-35.3563 with no redshift prior.

DESI-084.8493-59.3586 is a single galaxy strongly-lensed system. There is a red lensed arc to the East of the lens (with a photo$z$ of 0.593 ± 0.146), and the transient detection lies South of the lens. Additionally, it is possible that objects 3 and 4 (Figure 41) correspond to the same source galaxy, due to similarities in color and photo$z$, with the possibility that object 3 is the host. See Figure 42 for single exposure detection images and their corresponding differencing images.

Postulation 1: uL-SN Ia—Figure 43 shows the best-fit light-curve model for the uL-SN Ia scenario, with the foreground galaxy photo$z$ used as the redshift prior. The SALT3 model

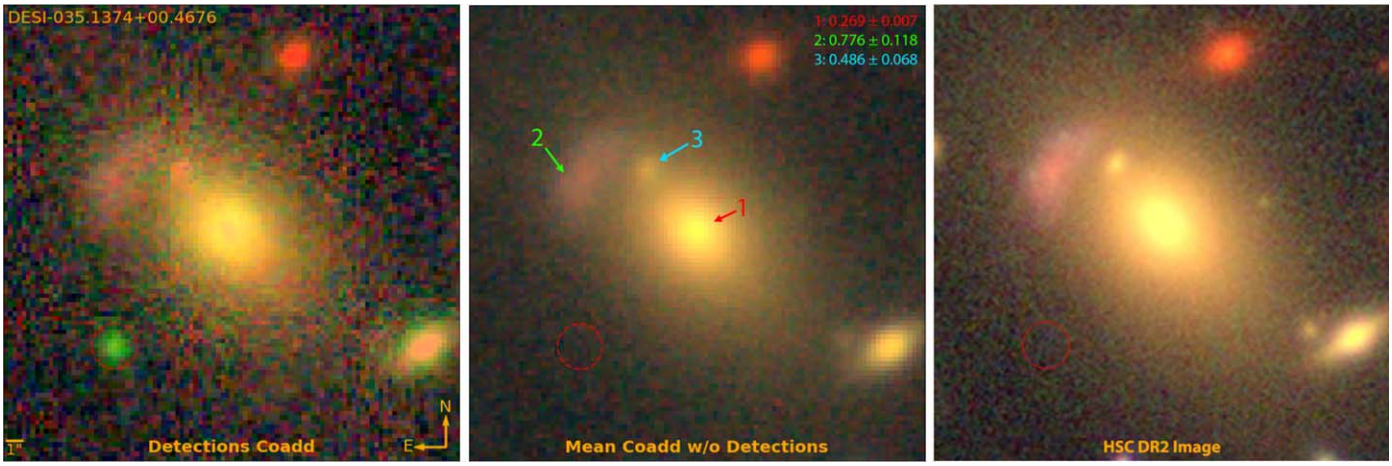

Figure 32. Coadded RGB images (using *g*, *r*, *i*, and *z* bands) of DESI-035.1374+00.4676 with and without the transient detection (red-dotted circle) exposures, as well as the HSC DR2 image. The labeled objects are color coded as in the following postulated scenario: the lens galaxy is red, the source galaxy is green, and the interloper or a member galaxy of the foreground group is cyan. Photometric redshifts are displayed on the top right-hand corner of the second image. The posited lens galaxy has a photo$z$ of 0.269 ± 0.007, and the posited lensed image has a photo$z$ of 0.776 ± 0.118.

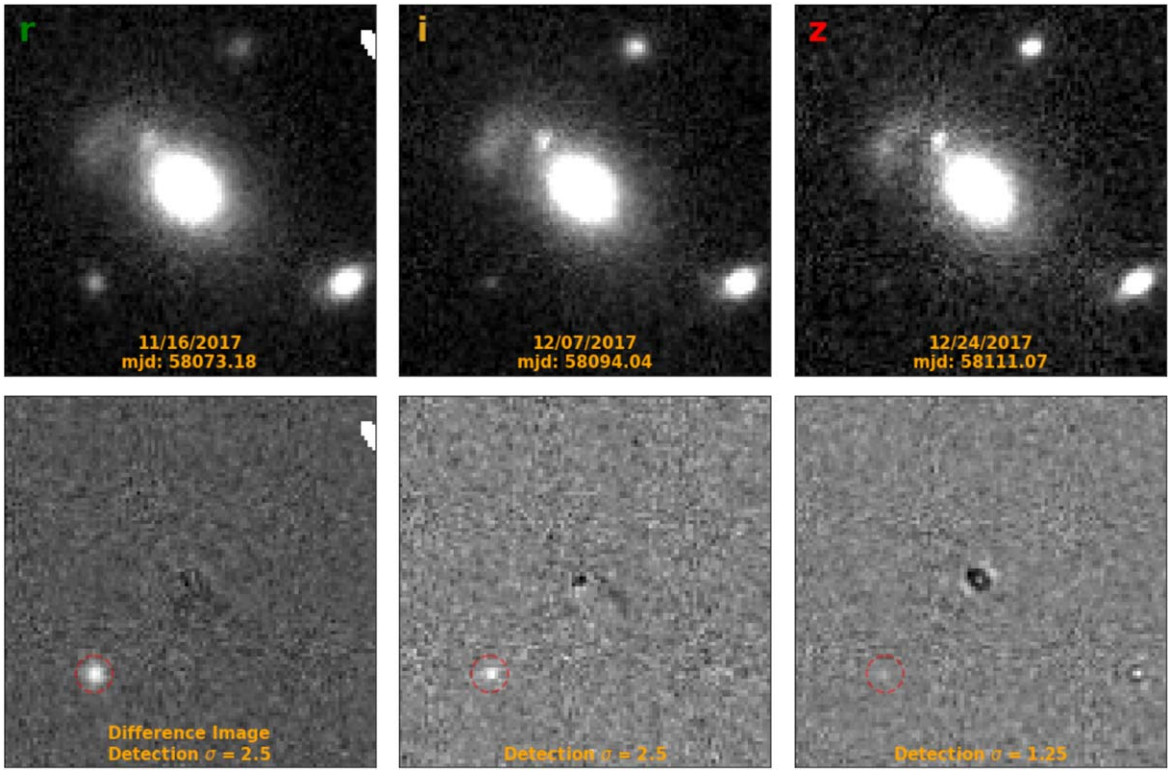

Figure 33. Detection exposures for the transientin DESI-035.1374+00.4676 in chronological order. See caption of Figure 10 for the full description.

agrees well with the data, with reasonable light-curve parameters and small Hubble residual.

Postulation 2: L-CC SN—Figure 44 shows the best-fit light-curve model for the L-CC SN scenario. The fit is significantly inferior to the previous postulation in the z band, requiring a high magnification of $86.05^{+153.15}_{-55.10}$, albeit with large uncertainties.

Conclusion—This transient in DESI-084.8493-59.3586 is likely to be an unlensed SN Ia, although there is a small possibility of it being a lensed CC SN. Thus, we give this system an appropriately low lensed SN grade of D. If found live, follow-up spectroscopic observations at the transient location could easily distinguish these two scenarios.

B.5. DESI-015.8465-50.5450

DESI-015.8465-50.5450 is a grade D+ strong lens candidate that was discovered in Storfer et al. (2022).

Upon closer inspection of DESI-015.8465-50.5450, we believe that it is more likely a face-on spiral galaxy. In the detection coadd image in Figure 45, the evidence for the spiral pattern (rather than lensed arcs) is especially strong in the *g* band. There are only two detections of this transient,

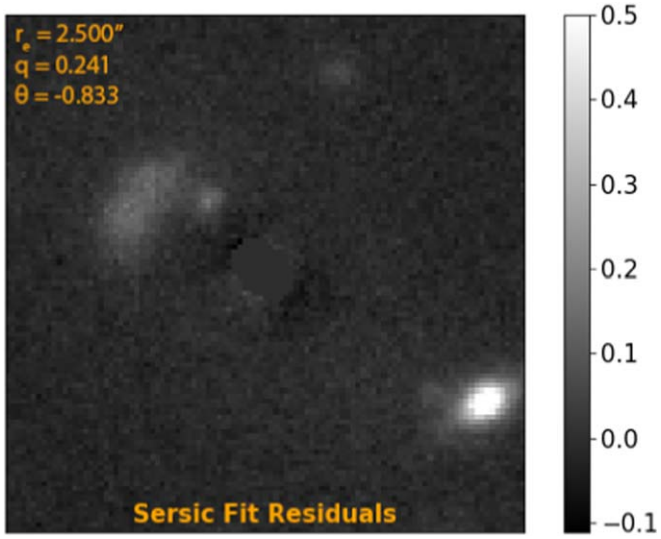

Figure 34. Residual image after lens light subtraction for DESI-035.1374+00.4676, with the Sérsic light parameters (half-light radius, axis ratio, and semimajor axis orientation from the *y*-axis) in the top left-hand corner (modeled in DECam *g* filter), with the core of the lens galaxy masked out.

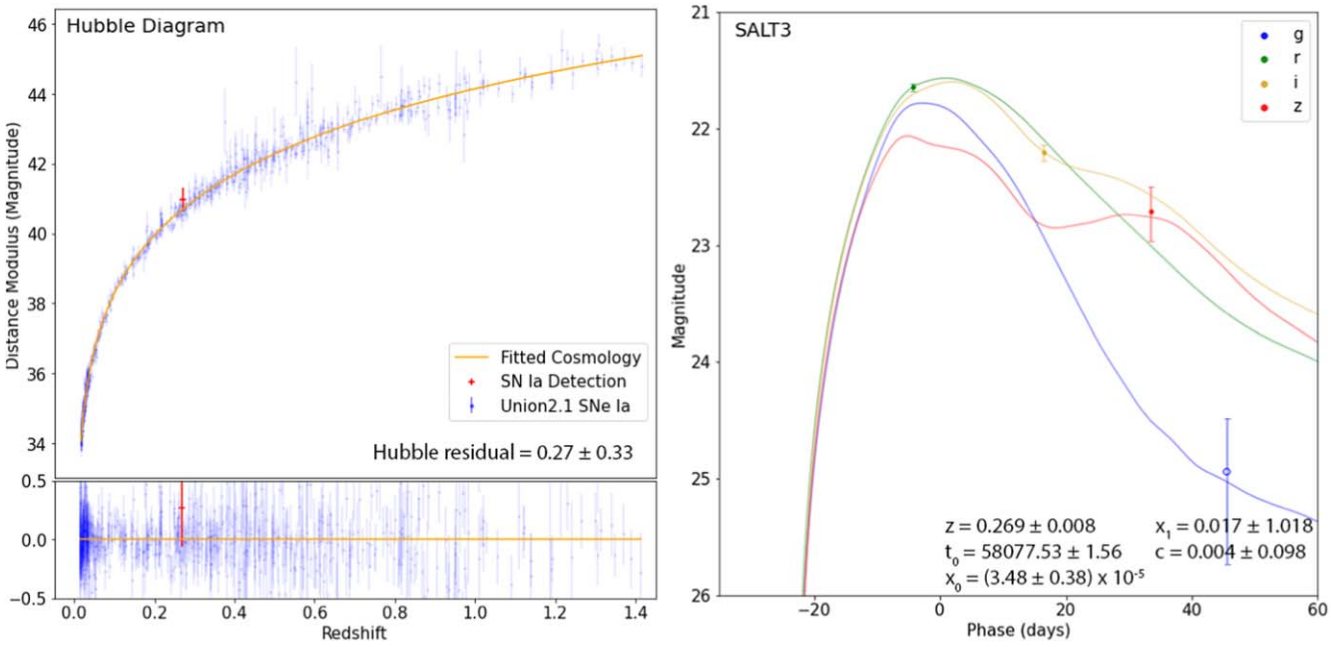

Figure 35. Best-fit SALT3 model for DESI-035.1374+00.4676 with a lens photo*z* redshift prior of 0.269 ± 0.007. For this and Figure 36, solid photometry points correspond to the detection passes shown in Figure 33.

observed two minutes apart. However, we do not observe a shift in detection location above the level of noise, and so we do not consider an asteroid as a likely scenario. See Figure 46 for single exposure detection images and their corresponding differencing images.

Postulation 1: uL-SN Ia—Figure 47 shows the best-fit light-curve model for the uL-SN Ia scenario. Due to the sparsity of the photometric data, the uncertainties of the SALT3 model parameters and Hubble residuals are large. While there are only two detection exposures, the pipeline identified this transient with four sub-detections. As with all of the other light curves presented, the light curves below are constrained by both detection and non-detection exposures.

Postulation 2: uL-CC SN—Figure 48 shows the best-fit light-curve model for the uL-CC SN scenario. This SN Ic-LB template (v19-2002ap-coor) is one of many templates that are consistent with the data.

Conclusion—The most likely scenario for the transient in DESI-015.8465-50.5450 is an unlensed supernova because the system is probably a spiral galaxy and not a strong lensing system. With the sparsity of photometric data, it is not possible to determine the type. It could also be the case that the host galaxy is object 4 (which could be lensed, possibly with object 3 as its counterimage), as opposed to object 1 (see Figure 45), but it is not feasible to determine this with the current data.

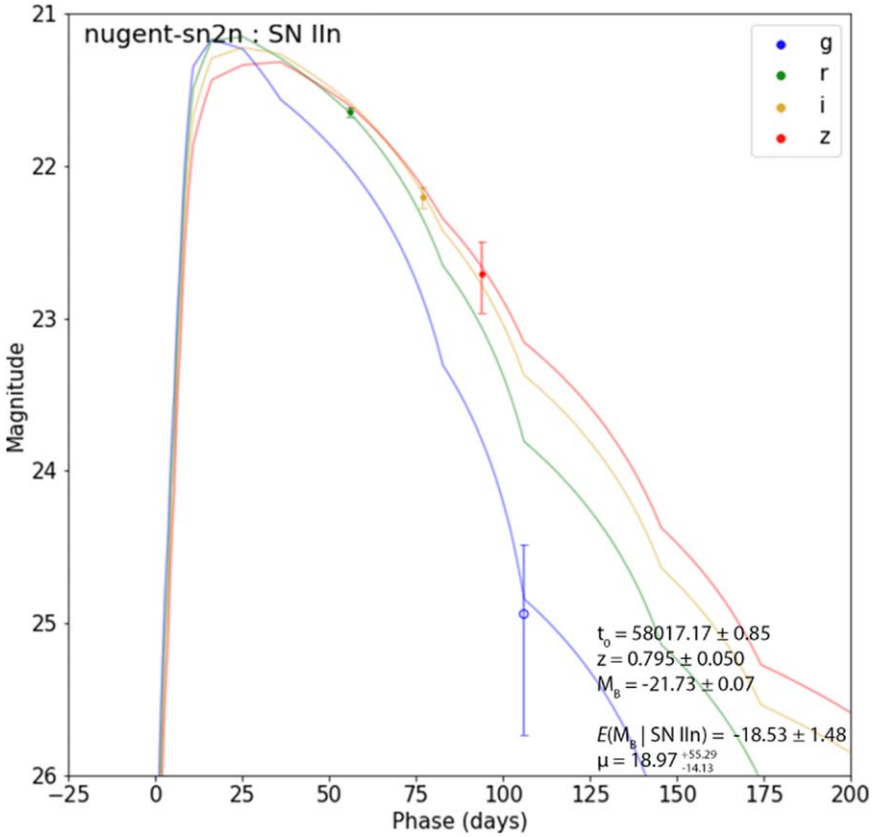

Figure 36. Best-fit core-collapse template model for DESI-035.1374+00.4676 with a source photo$z$ redshift prior of 0.776 ± 0.118.

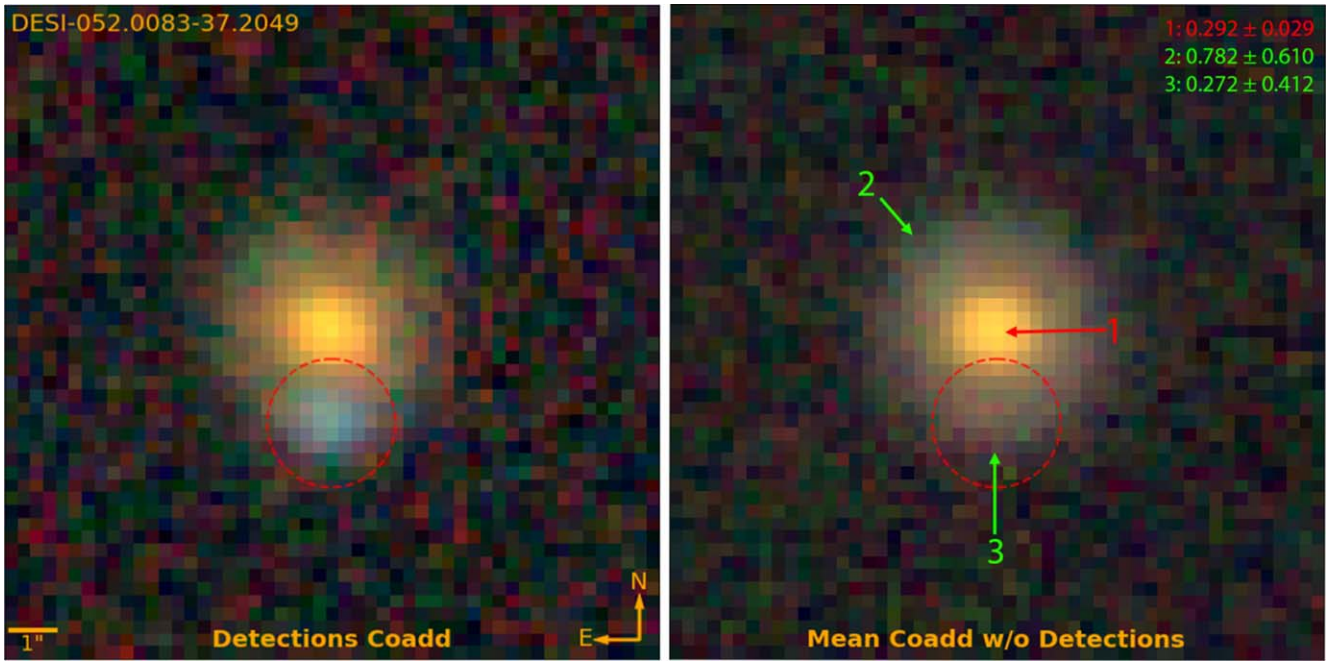

Figure 37. Coadded RGB images (using g, r, i, and z bands) of DESI-052.0083-37.2049 with and without the transient detection (red-dotted circle) exposures. The labeled objects are color coded as in the following postulated scenario: the lens galaxy is red and the source galaxy is green. Photometric redshifts are displayed on the top right-hand corner. The posited lens galaxy has a photo$z$ of 0.292 ± 0.029, the posited lensed images have photo$z$es of 0.782 ± 0.610 and 0.272 ± 0.412.

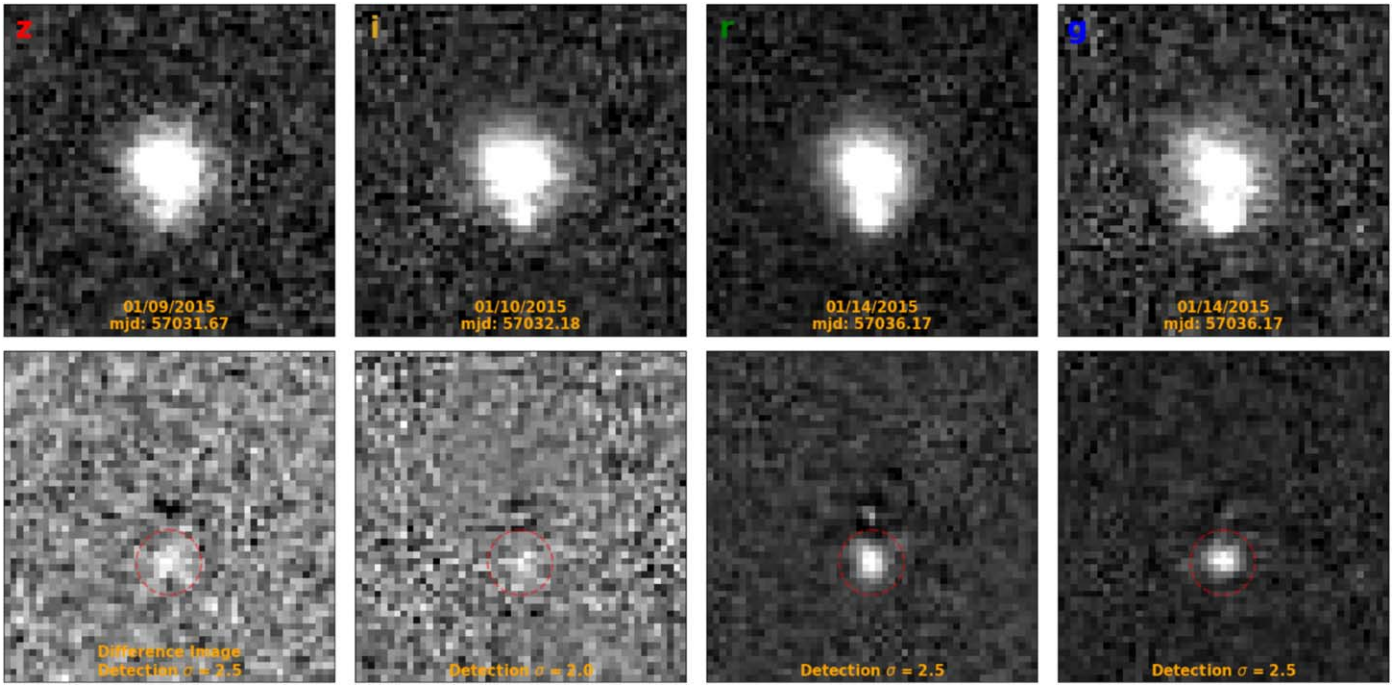

Figure 38. Detection exposures for the transient in DESI-052.0083-37.2049 in chronological order. See caption of Figure 10 for the full description.

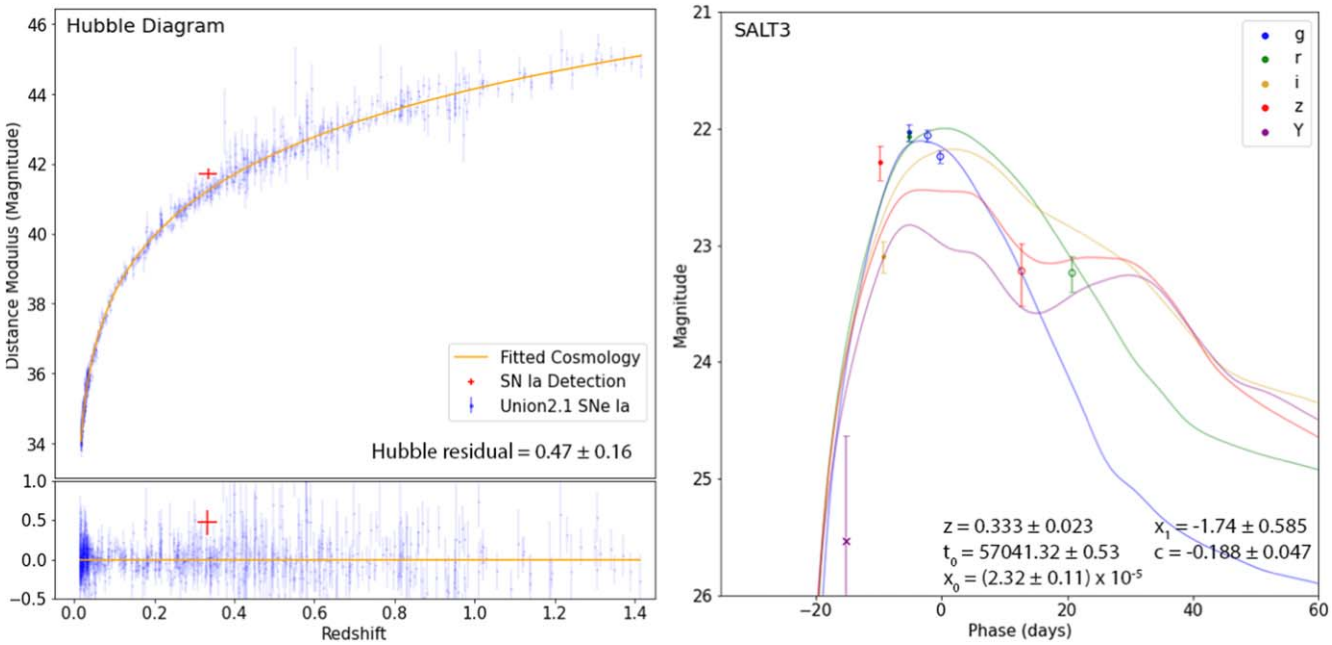

Figure 39. Best-fit SALT3 model for DESI-052.0083-37.2049 with a lens photo$z$ redshift prior of 0.292 ± 0.029. For this and Figure 40, solid photometry points correspond to the detection passes shown in Figure 38, hollow points correspond to other exposures with PSF photometry, and crosses correspond to measurements using aperture photometry.

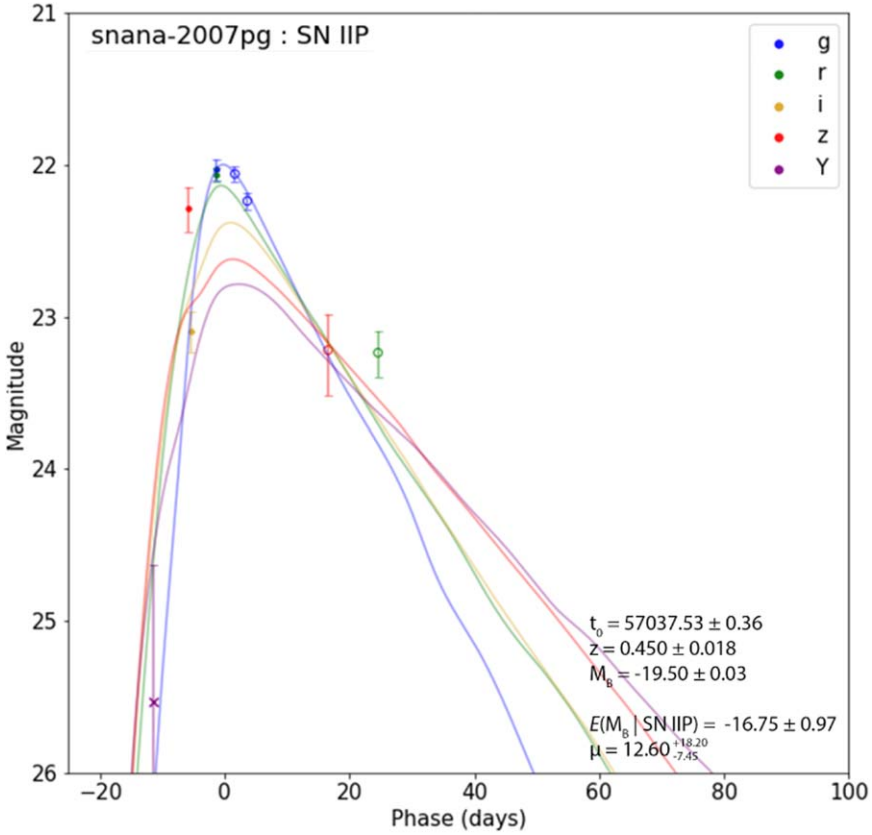

Figure 40. Best-fit core-collapse template model for DESI-052.0083-37.2049 with no redshift prior.

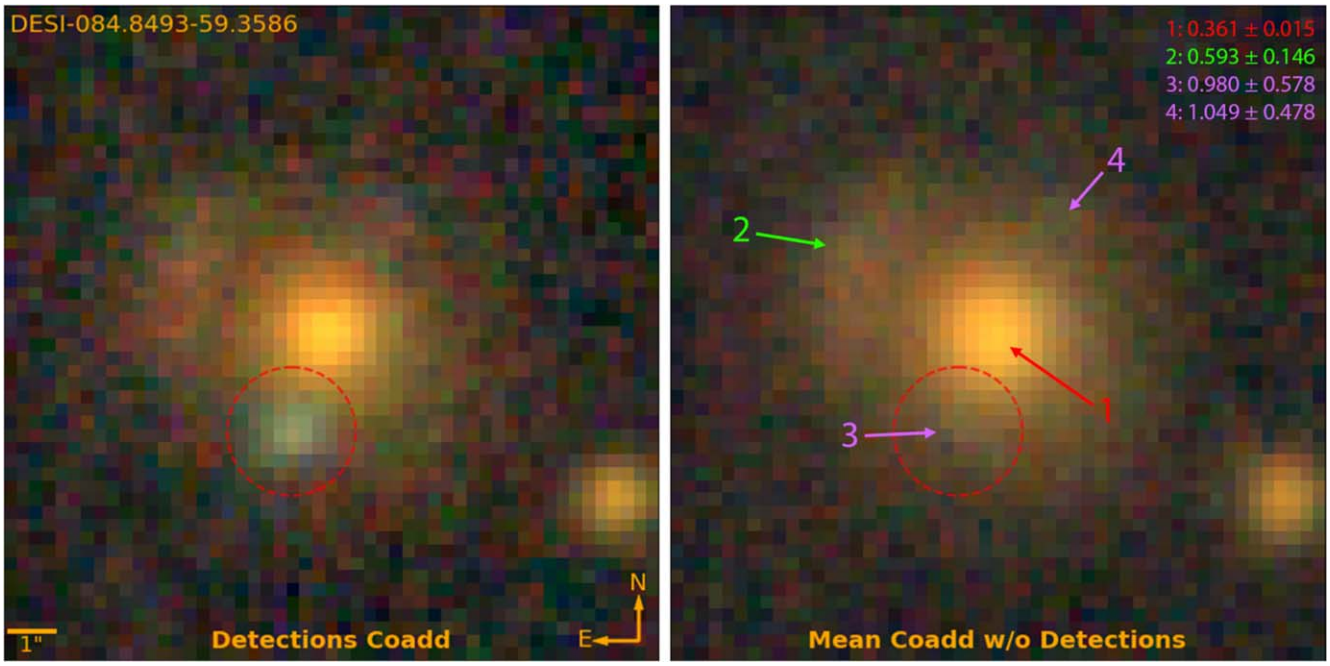

Figure 41. Coadded RGB images (using *g*, *r*, *i*, and *z* bands) of DESI-084.8493-59.3586 with and without the transient detection (red-dotted circle) exposures. The labeled objects are color coded as in the following postulated scenario: the lens galaxy is red, the source galaxy is green, and the second source is purple. Photometric redshifts are displayed on the top right-hand corner. The posited lens galaxy has a photo$z$ of 0.361 ± 0.015, the posited lensed image has a photo$z$ of 0.593 ± 0.146, and a second posited lensed source have photo$z$es of 0.980 ± 0.578 and 1.049 ± 0.478.

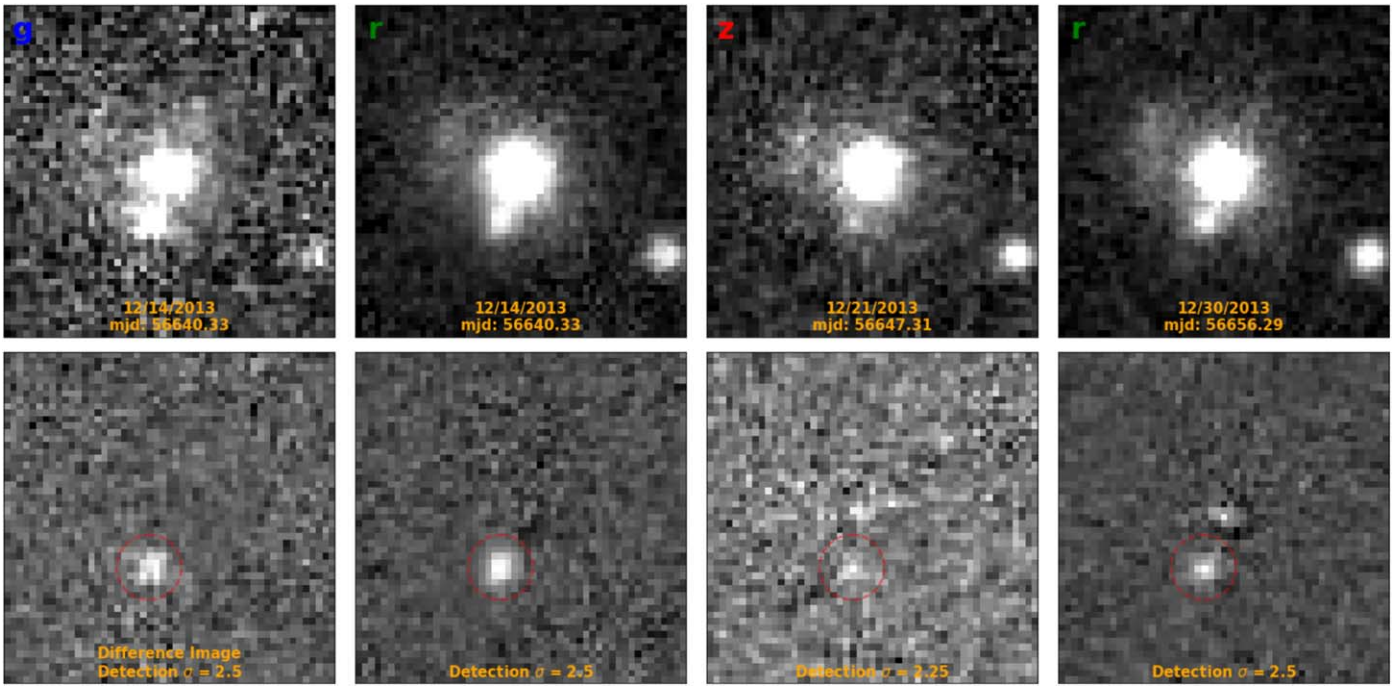

Figure 42. Detection exposures for the transient in DESI-084.8493-59.3586 in chronological order. See caption of Figure 10 for the full description.

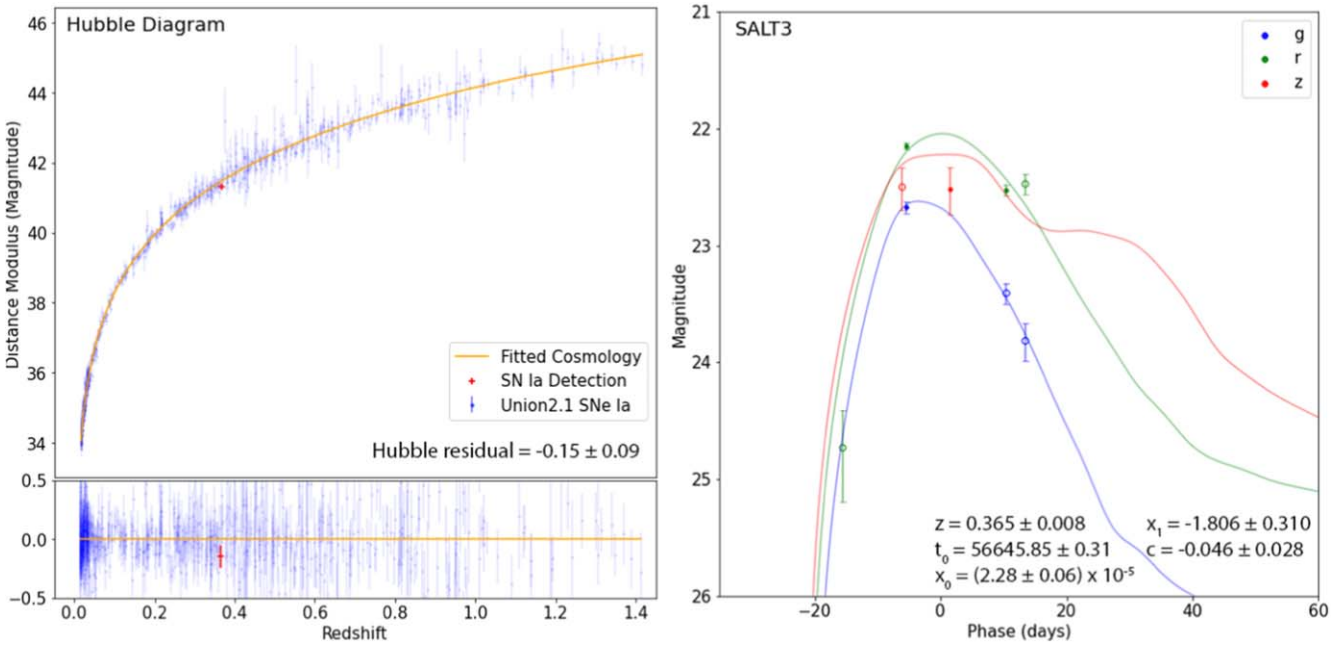

Figure 43. Best-fit SALT3 model for DESI-084.8493-59.3586 with a lens photo$z$ redshift prior of 0.361 ± 0.015. For this and Figure 44, solid photometry points correspond to the detection passes shown in Figure 42.

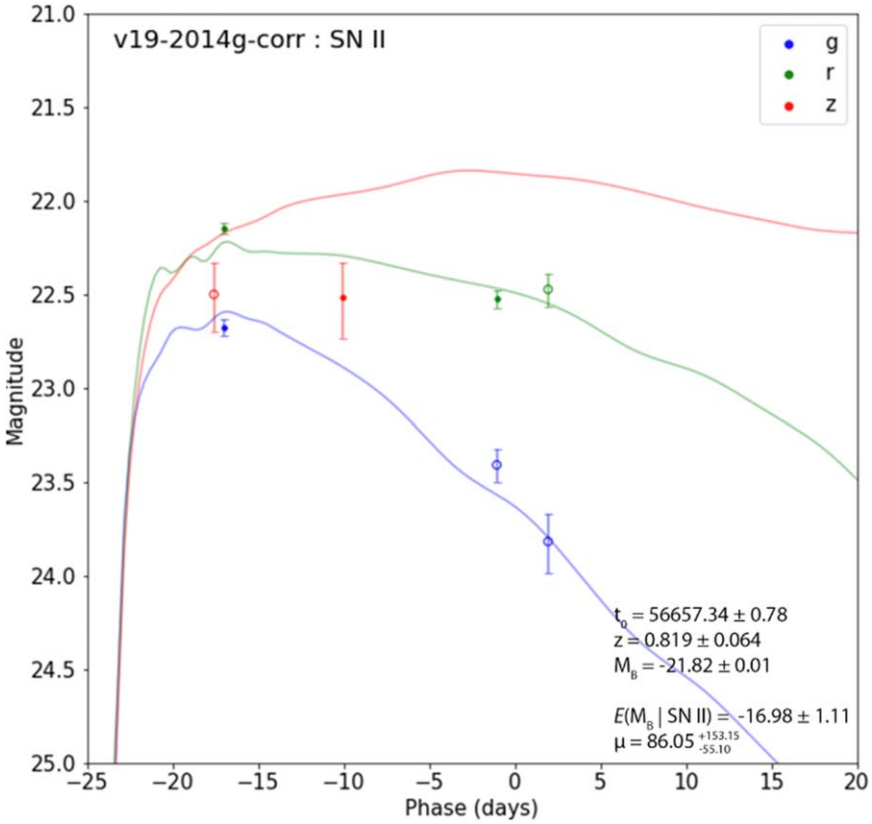

Figure 44. Best-fit core-collapse template model for DESI-084.8493-59.3586 with a source photoz redshift prior of 0.593 ± 0.146.

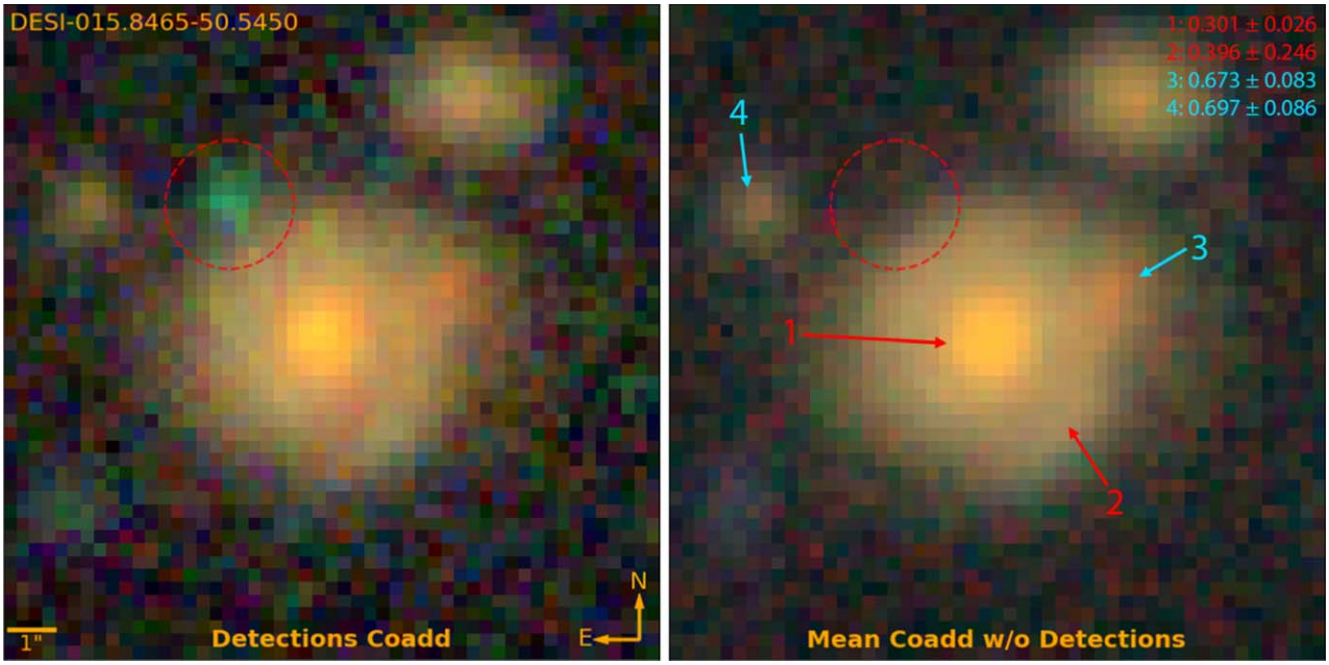

Figure 45. Coadded RGB images (using *g*, *r*, *i*, and *z* bands) of DESI-015.8465-50.5450 with and without the transient detection (red-dotted circle) exposures. The labeled objects are color coded as in the following postulated scenario: the main galaxy is red and the surrounding galaxies are cyan. Photometric redshifts are displayed on the top right-hand corner. Photometric redshifts are displayed on the top right-hand corner. The posited host galaxy has photozes of 0.301 ± 0.026 and 0.396 ± 0.246.

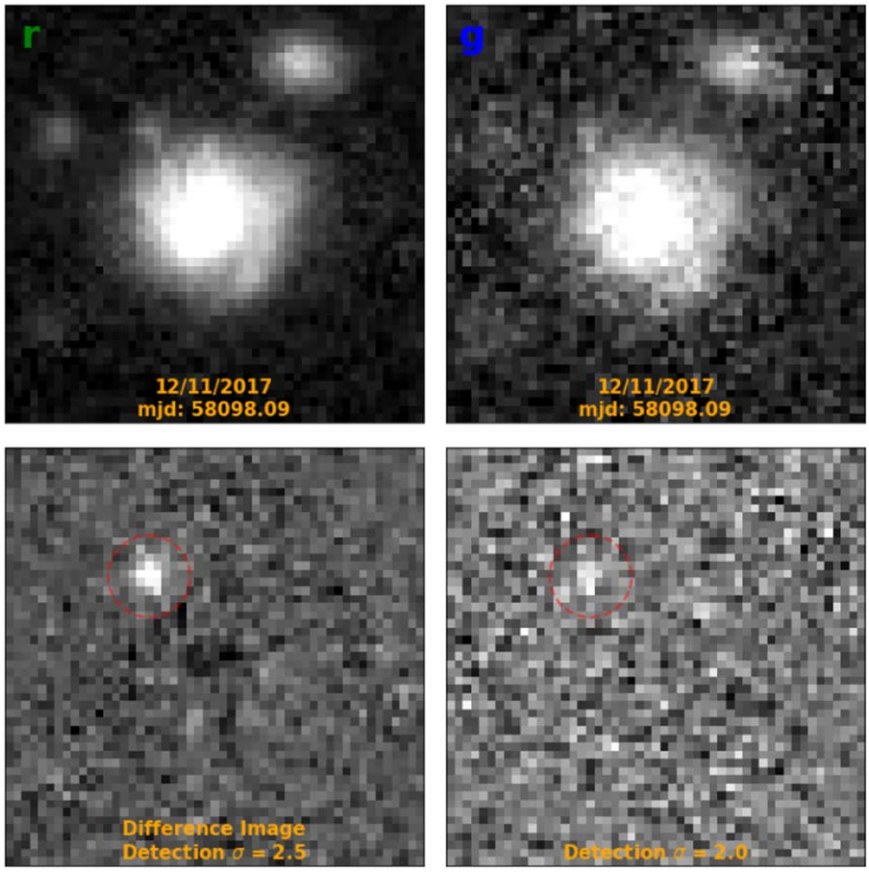

Figure 46. Detection exposures for the transient in DESI-015.8465-50.5450 in chronological order. See caption of Figure 10 for the full description.

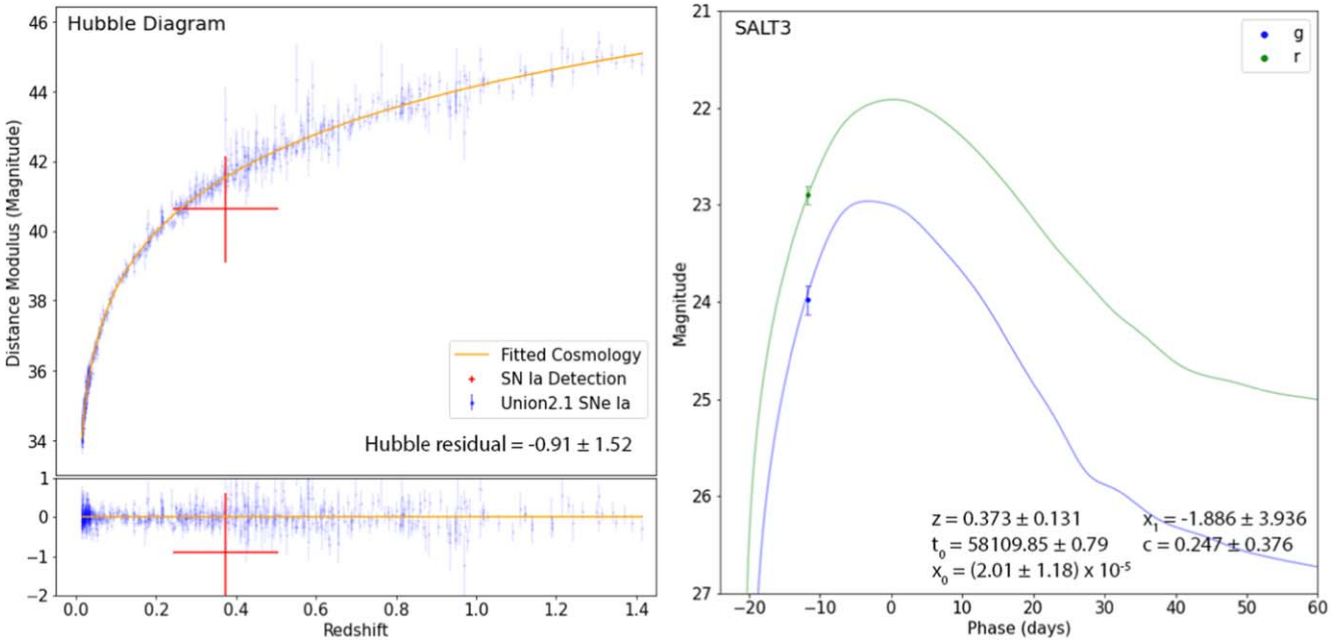

Figure 47. Best-fit SALT3 model for DESI-015.8465-50.5450 with a lens photo$z$ redshift prior of 0.301 $\pm$ 0.026. For this and Figure 48, photometry points correlate to the detections shown in Figure 46.

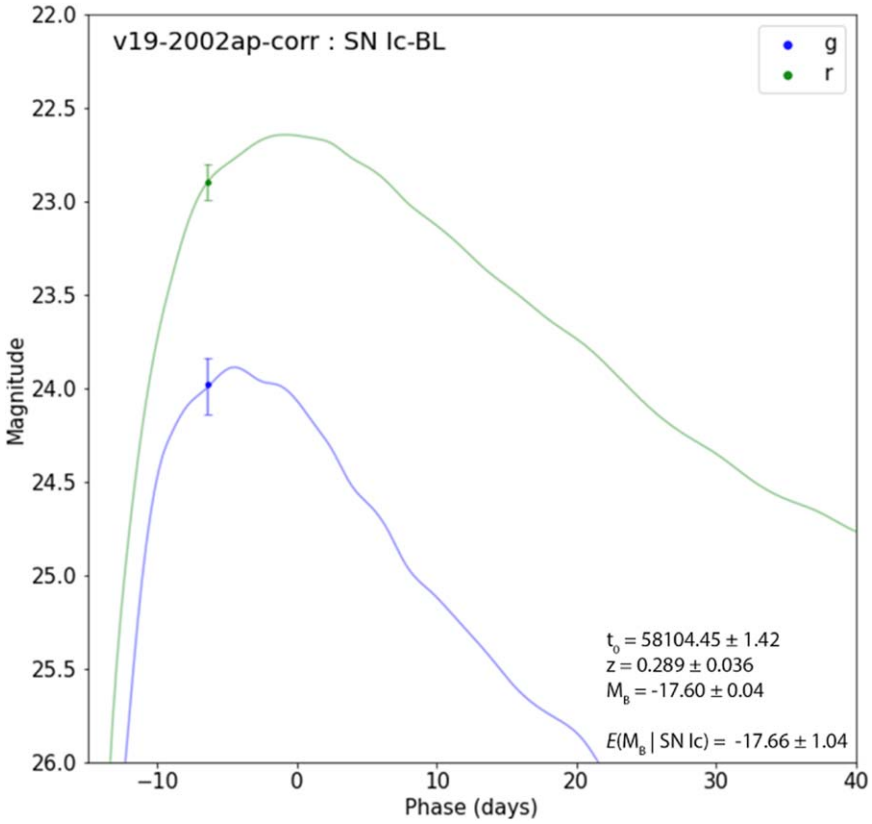

Figure 48. Best-fit core-collapse template model for DESI-015.8465-50.5450 with a lens photo$z$ redshift prior of 0.301 ± 0.026.

Appendix C
Asteroids

We have found two asteroid candidates (see Figures 49 and 50). The detections are observed on the same night (for each respective system), separated by approximately one to two minutes. The locations of the two detections in each case are spatially close enough for the pipeline to identify them as candidates (as a group of three to four sub-detections). PSF fitting for the transient detections shows that the movements between detections for both systems are significant. The approximate speeds of the transients are consistent with those of a main-belt asteroid (roughly $0\farcs5$ per minute near opposition; Cicco 2006).

C.1. DESI-008.6173+02.4228

For DESI-008.6173+02.4228, we find that the transient has moved $0\farcs475 \pm 0.101$ between the r and g band detections; a movement of $>4\sigma$ significance. Since the exposures were taken 1.98 minutes apart, the estimated speed of this asteroid is $0\farcs240 \pm 0.055$ per minute. This is slower than the typical main-belt asteroid (near opposition) speed of $0\farcs5$ per minute, but not unreasonably so. The coordinates and time observed do not correlate with any known asteroid in the IAU's Minor Planet Center[17] database.

C.2. DESI-150.4863+15.4209

In DESI-150.4863+15.4209, we find that the transient has moved $2\farcs155 \pm 0.372$ between the r and g band detections, with a significance of $>5\sigma$. The exposures were taken 1.23 minutes apart. Thus, the estimated speed of this asteroid is $0\farcs475 \pm 0.082$ per minute, which is consistent with a main-belt asteroid near opposition. The coordinates and time observed do not correlate with any known asteroid in the IAU's Minor Planet Center[18] database.

[17] https://www.minorplanetcenter.net/iau/mpc.html
[18] https://www.minorplanetcenter.net/iau/mpc.html

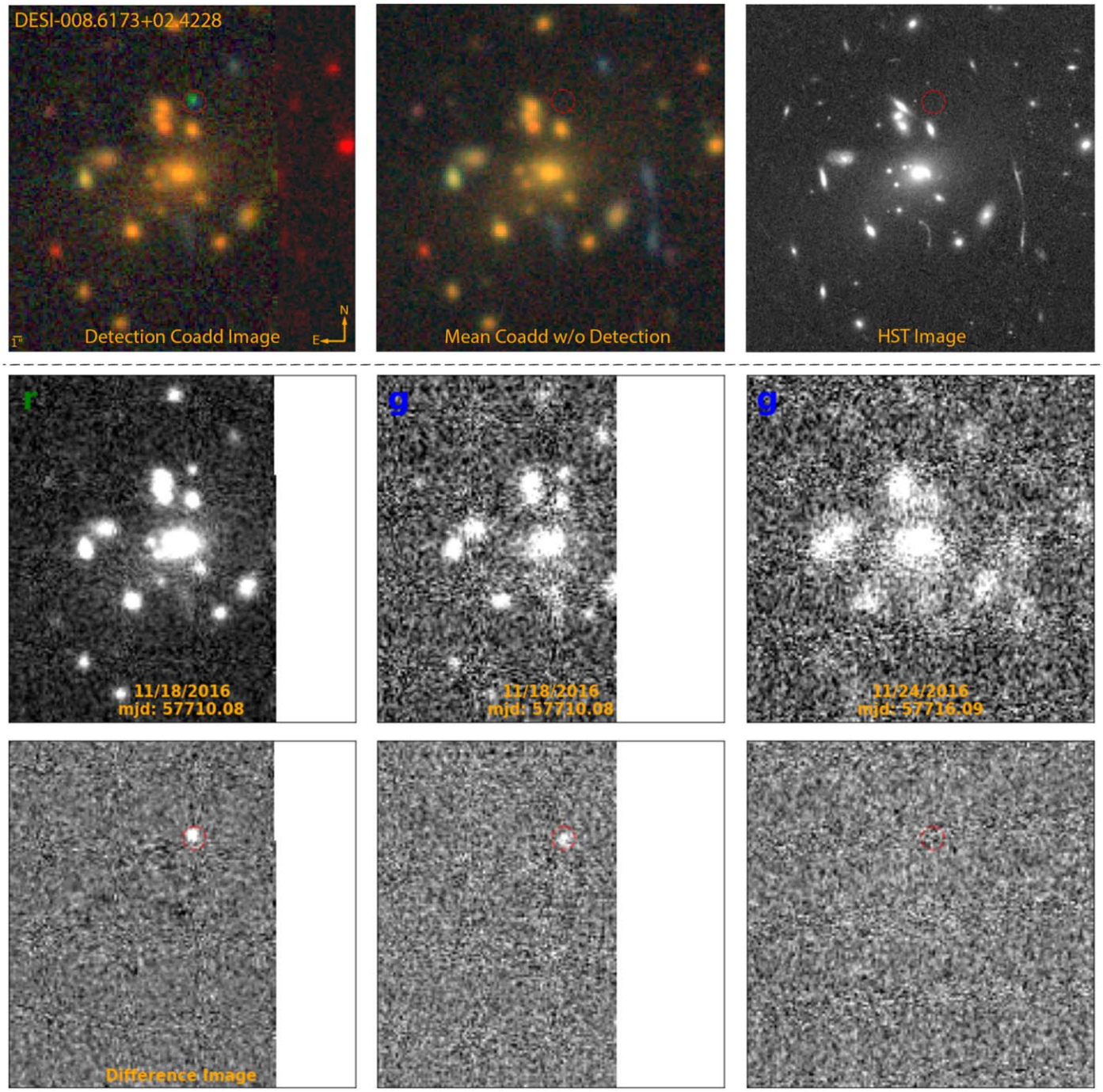

Figure 49. Above the dotted line are coadded images of DESI-008.6173+02.4228 with and without the transient detection (red-dotted circle) exposures. From left-hand to right-hand, the images show: (1) the coadded image generated from mean coadding from only the exposures with the transient detection, within each band; (2) the coadded image, generated from mean coadding all exposures excluding the detection exposures within each band; and (3) the HST image of the system (HST Proposal ID: 12884; H. Ebeling). The RGB image incorporates *g*, *r*, *i*, and *z* bands. Below the dotted line are detection exposures for the transient. Each column is a single detection at the labeled date and band. The top row is the single exposure image, whereas the bottom is the SFFT difference image. The detection location is marked with a red-dotted circle. The first and second columns show *r* and *g* band detections on 2016 January 18 minutes apart, whereas the third column shows a set on non-detections six days afterwards. Note the slight but significant shift in the transient location between the two detections.

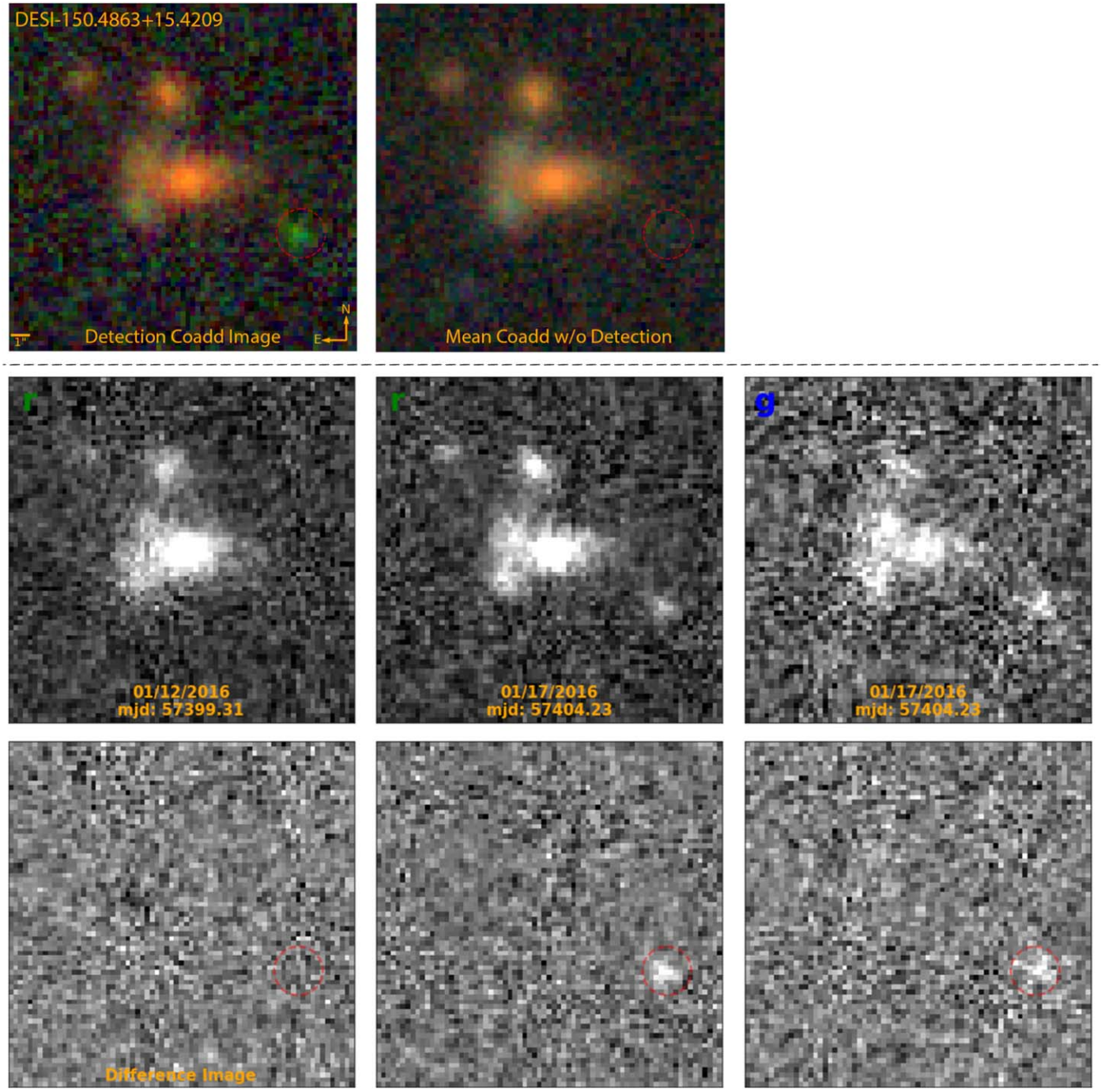

Figure 50. Above the dotted line are coadded images of DESI-150.4863+15.4209 with and without the transient detection (red-dotted circle) exposures (see Figure 49 caption). Below the dotted line are detection exposures for the transient. The second and third columns show detections on 2016 January 17, while the first column shows a non-detection on 2016 January 12 (5 days prior to detection). The detection location is marked with a red-dotted circle. As with the previous system, there is a significant shift in detection location between the exposures.

ORCID iDs

William Sheu https://orcid.org/0000-0003-1889-0227
Xiaosheng Huang https://orcid.org/0000-0001-8156-0330
Aleksandar Cikota https://orcid.org/0000-0001-7101-9831
Nao Suzuki https://orcid.org/0000-0001-7266-930X
David J. Schlegel https://orcid.org/0000-0002-5042-5088
Christopher Storfer https://orcid.org/0000-0002-0385-0014

References

Abbott, T. M. C., Adamów, M., Aguena, M., et al. 2021, ApJS, 255, 20
Aihara, H., AlSayyad, Y., Ando, M., et al. 2019, PASJ, 71, 114
Alard, C. 2000, A&AS, 144, 363
Astropy Collaboration, Price-Whelan, A. M., Sipőcz, B. M., et al. 2018, AJ, 156, 123
Astropy Collaboration, Robitaille, T. P., Tollerud, E. J., et al. 2013, A&A, 558, A33
Barbary, K. 2014, sncosmo v0.4.2, Zenodo, doi:10.5281/zenodo.11938
Barbary, K. 2018, SEP: Source Extraction and Photometry, Astrophysics Source Code Library, ascl:1811.004
Becker, A. 2015, HOTPANTS: High Order Transform of PSF ANd Template Subtraction, Astrophysics Source Code Library, ascl:1504.004
Bell, E. F., Zheng, X. Z., Papovich, C., et al. 2007, ApJ, 663, 834
Bertin, E., & Arnouts, S. 1996, A&AS, 117, 393
Birrer, S., Dhawan, S., & Shajib, A. J. 2022, ApJ, 924, 2
Bramich, D. M. 2008, MNRAS: Lett., 386, L77
Cañameras, R., Schuldt, S., Shu, Y., et al. 2021, A&A, 653, L6
Cañameras, R., Schuldt, S., Suyu, S. H., et al. 2020, A&A, 644, A163
Carrasco, M., Barrientos, L. F., Anguita, T., et al. 2017, ApJ, 834, 210
Chambers, K. C., Magnier, E. A., Metcalfe, N., et al. 2016, arXiv:1612.05560
Chen, W., Kelly, P. L., Oguri, M., et al. 2022, Natur, 611, 256
Cicco, D. 2006, Hunting Asteroids From Your Backyard, Sky and TelescopeSky & Telescope, https://skyandtelescope.org/observing/hunting-asteroids-from-your-backyard/
Craig, P., O'Connor, K., Chakrabarti, S., et al. 2021, arXiv:2111.01680
Dark Energy Survey Collaboration, Abbott, T., Abdalla, F. B., et al. 2016, MNRAS, 460, 1270
Dey, A., Rabinowitz, D., Karcher, A., et al. 2016, Proc. SPIE, 9908, 99082C
Dey, A., Schlegel, D. J., Lang, D., et al. 2019, AJ, 157, 168
Dhawan, S., Johansson, J., Goobar, A., et al. 2020, MNRAS, 491, 2639
Diehl, H. T., Buckley-Geer, E. J., Lindgren, K. A., et al. 2017, ApJS, 232, 15
Eldridge, J. J., Fraser, M., Smartt, S. J., Maund, J. R., & Crockett, R. M. 2013, MNRAS, 436, 774
Fitzpatrick, E. L. 1999, PASP, 111, 63
Flaugher, B., Diehl, H. T., Honscheid, K., et al. 2015, AJ, 150, 150
Freedman, W. L. 2021, ApJ, 919, 16
Gilliland, R. L., Nugent, P. E., & Phillips, M. M. 1999, ApJ, 521, 30
Goobar, A., Amanullah, R., Kulkarni, S. R., et al. 2017, Sci, 356, 291
Goobar, A., Johansson, J., Dhawan, S., et al. 2022, TNSAN, 180, 1
Grillo, C., Rosati, P., Suyu, S. H., et al. 2020, ApJ, 898, 87
Guy, J., Astier, P., Baumont, S., et al. 2007, A&A, 466, 11
Guy, J., Sullivan, M., Conley, A., et al. 2010, A&A, 523, A7
Harris, C. R., Millman, K. J., van der Walt, S. J., et al. 2020, Natur, 585, 357
Hounsell, R., Scolnic, D., Foley, R. J., et al. 2018, ApJ, 867, 23
Hu, L., Wang, L., Chen, X., & Yang, J. 2022, ApJ, 936, 157
Huang, X., Storfer, C., Gu, A., et al. 2021, ApJ, 909, 27
Huang, X., Storfer, C., Ravi, V., et al. 2020, ApJ, 894, 78
Hunter, J. D. 2007, CSE, 9, 90
Jacob, J. C., Katz, D. S., Berriman, G. B., et al. 2010, arXiv:1005.4454
Jacobs, C., Collett, T., Glazebrook, K., et al. 2019, ApJS, 243, 17
Jacobs, C., Glazebrook, K., Collett, T., More, A., & McCarthy, C. 2017, MNRAS, 471, 167
Ivezić, Ž, Kahn, S. M., Tyson, J. A., et al. 2019, ApJ, 873, 111
Kelly, P., Zitrin, A., Oguri, M., et al. 2022, TNSAN, 169, 1
Kelly, P. L., Diego, J. M., Rodney, S., et al. 2018, NatAs, 2, 334
Kelly, P. L., Rodney, S. A., Treu, T., et al. 2015, Sci, 347, 1123
Kelly, P. L., Rodney, S. A., Treu, T., et al. 2016, ApJL, 819, L8
Kenworthy, W. D., Jones, D. O., Dai, M., et al. 2021, ApJ, 923, 265
Lang, D., Hogg, D. W., & Mykytyn, D. 2016, The Tractor: Probabilistic astronomical source detection and measurement, Astrophysics Source Code Library, ascl:1604.008
Levan, A., Nugent, P., Fruchter, A., et al. 2005, ApJ, 624, 880
Madau, P., & Dickinson, M. 2014, ARA&A, 52, 415
Moustakas, L. 2012, in 10th Hellenic Astronomical Conf., ed. I. Papadakis & A. Anastasiadis, 14
Narayan, R., & Bartelmann, M. 1996, arXiv:astro-ph/9606001
Oguri, M., & Marshall, P. J. 2010, MNRAS, 405, 2579
Perlmutter, S., Aldering, G., Goldhaber, G., et al. 1999, ApJ, 517, 565
Pierel, J. D. R., Arendse, N., Ertl, S., et al. 2023, ApJ, 948, 115
Planck Collaboration, Aghanim, N., Akrami, Y., et al. 2020, A&A, 641, A6
Pourrahmani, M., Nayyeri, H., & Cooray, A. 2018, ApJ, 856, 68
Quimby, R. M., Oguri, M., More, A., et al. 2014, Sci, 344, 396
Richardson, D., III, R. L. J., Wright, J., & Maddox, L. 2014, AJ, 147, 118
Riess, A. G., Casertano, S., Yuan, W., et al. 2021, ApJL, 908, L6
Riess, A. G., Filippenko, A. V., Challis, P., et al. 1998, AJ, 116, 1009
Rodney, S. A., Brammer, G. B., Pierel, J. D. R., et al. 2021, NatAs, 5, 1118
Rodney, S. A., Strolger, L.-G., Kelly, P. L., et al. 2016, ApJ, 820, 50
Sako, M., Bassett, B., Becker, A. C., et al. 2018, PASP, 130, 064002
Schlafly, E. F., & Finkbeiner, D. P. 2011, ApJ, 737, 103
Scolnic, D., Brout, D., Carr, A., et al. 2022, ApJ, 938, 113
Shu, Y., Bolton, A. S., Mao, S., et al. 2018, ApJ, 864, 91
Shu, Y., Bolton, A. S., Mao, S., et al. 2021, ApJ, 919, 67
Shu, Y., Brownstein, J. R., Bolton, A. S., et al. 2017, ApJ, 851, 48
Shu, Y., Cañameras, R., Schuldt, S., et al. 2022, A&A, 662, A4
Smit, R., Bouwens, R. J., Franx, M., et al. 2012, ApJ, 756, 14
Smith, M., D'Andrea, C. B., Sullivan, M., et al. 2020, AJ, 160, 267
Sobral, D., Smail, I., Best, P. N., et al. 2012, MNRAS, 428, 1128
Sonnenfeld, A., & Leauthaud, A. 2018, MNRAS, 477, 5460
Spergel, D., Gehrels, N., Baltay, C., et al. 2015, arXiv:1503.03757
Stein, G., Blaum, J., Harrington, P., Medan, T., & Lukić, Z. 2022, ApJ, 932, 107
Storfer, C., Huang, X., Gu, A., et al. 2022, arXiv:2206.02764
Suyu, S. H., Huber, S., Cañameras, R., et al. 2020, A&A, 644, A162
Suzuki, N., Rubin, D., Lidman, C., et al. 2012, ApJ, 746, 85
Vincenzi, M., Sullivan, M., Firth, R. E., et al. 2019, MNRAS, 489, 5802
Welch, B., Coe, D., Diego, J. M., et al. 2022, Natur, 603, 815
Williams, G. G., Olszewski, E., Lesser, M. P., & Burge, J. H. 2004, Proc. SPIE, 5492, 787
Wong, K. C., Sonnenfeld, A., Chan, J. H. H., et al. 2018, ApJ, 867, 107
Wong, K. C., Suyu, S. H., Chen, G. C.-F., et al. 2019, MNRAS, 498, 1420
Zackay, B., Ofek, E. O., & Gal-Yam, A. 2016, ApJ, 830, 27
Zhou, R., Newman, J. A., Mao, Y.-Y., et al. 2020, MNRAS, 501, 3309